

Aerodynamics of a Scramjet Cavity Flameholder at On- and Off-Design Conditions

A dissertation presented to the faculty of the
School of Engineering and Applied Science of the
University of Virginia

In partial fulfillment of the requirements for the degree of

Doctor of Philosophy
Mechanical and Aerospace Engineering

by

Justin William Kirik

May 2017

APPROVAL SHEET

This dissertation is submitted in partial fulfillment of the
requirements for the degree of

Doctor of Philosophy
Mechanical and Aerospace Engineering

Justin W. Kirik

Author

This dissertation has been read and approved by the Examining Committee:

Christopher P. Goyne

Advisor

James C. McDaniel

Chair

George L. Cahen

Campbell D. Carter

Harsha K. Chelliah

Eric Loth

Matthew A. Reidenbach

Accepted for the School of Engineering and Applied Science:



Craig H. Benson, Dean, School of Engineering and Applied Science

May 2017

© 2017 Justin W. Kirik

All Rights Reserved

For my family

Abstract

Supersonic combustion ramjet (scramjet) engines offer the promise of making hypersonic aircraft an operational reality, lowering the costs of space access and enabling a responsive high-speed flight capability for national defense. Particle image velocimetry (PIV) is a technique ideal for the aerodynamic characterization of the scramjet flameholding process due to its ability to provide instantaneous and ensemble measurements at high spatial resolution across a planar measurement region. This work applied PIV to two configurations of a DMSJ cavity flameholder, characterizing its turbulent aerodynamics at conditions representative of operational design points as well as departures from them. An examination of replicated inlet-generated distortion found that the extent of recirculating flow in the cavity, which governs entrainment and residence time of fuel and air, was strongly dependent on the impingement location of an oblique shock wave. Impingement upstream of the cavity diminished the size of the recirculation region, whereas impingement directly on the cavity increased it. The aerodynamics of fuel injection upstream of the cavity were replicated with wall-normal sonic air injection, which thickened the shear layer separating cavity recirculation from main-duct flow and reduced spatial variation of fluctuating velocity magnitudes.

Past measurements have been challenged by the tendency of conventional metal oxide velocimetry tracers to inhibit their own imaging by adhering to flowpath windows. To resolve this limitation, the novel application of graphite flakes as PIV tracers in a high-speed flow was shown to provide acceptable flow tracking while maintaining compatibility with flowpath windows and persistence through the reaction zone. Subsequent measurements examined flameholder operation with pre-mixed hydrocarbon fueling at both steady-state conditions as well as during the lean-blowout transient. Air injection downstream of the combustor was used to maintain the pre-combustion shock system independent of the amount of heat release.

It was found that mean velocity in the spanwise center plane of the cavity flameholder was governed primarily by the length of the shock system, whereas turbulent fluctuations were most strongly influenced by whether or not combustion was present, indicating turbulent aerodynamics of dual-mode operation cannot be replicated by artificial blockage. Comparison of PIV results with corresponding measurements of the OH and CH^{*} radicals demonstrated how main-duct combustion is dependent on turbulent exchange with the cavity, and three-component PIV measurements at the boundary of the cavity and main duct indicated that the flow is largely spanwise-uniform at this interface. Turbulence intensity at the combustor entrance was found to be positively correlated with prior measurements of flame front angle, demonstrating how turbulent fluctuations drive flame spreading rate in the premixed regime. Integral length scales at this location were found to be constant with a change in fueling rate from one operational limit to the other, providing further evidence that turbulent aerodynamics are dependent on the presence of heat release and not its magnitude.

Examination of the lean blowout transient with kHz-rate PIV found that changes in cavity aerodynamics were confined to a period prior to blowout two orders of magnitude smaller than that of the collapse of the pre-combustion shock system, suggesting the cessation of flameholding was due to the cavity mixture falling below flammability limits, rather than an alteration of the turbulent exchange between the cavity and the remainder of the combustor. This result suggests current flight-proven velocimetry techniques could be used in a flight vehicle to predict imminent blowout and enable operation near the lean limit.

Acknowledgments

It has been said that airspeed and money are the only prerequisites for flight, and this research was no exception. Funding was received through a number of sources: the U.S. Air Force Summer Faculty Fellowship Program, funded by the U.S. Air Force Office of Scientific Research (AFOSR) and administered by the American Society for Engineering Education (ASEE); the United States Department of Defense via the National Defense Science and Engineering Graduate Research Fellowship, 32 CFR 168a, also administered by ASEE; AFOSR and the National Aeronautics and Space Administration (NASA) via the National Center for Hypersonic Combined Cycle Propulsion grant FA 9550-09-1-0611; the University of Virginia Commonwealth Fellowship in Engineering; the Virginia Space Grant Consortium Graduate Research Fellowship; and the Dean of the University of Virginia School of Engineering and Applied Science. Additionally, the graphite tracers used in this study were provided at no cost by Asbury Carbons. I am sincerely grateful to all of these sources, and most of all to the American and Virginia taxpayer, whose earnings ultimately funded this work and of which I hope to have been a good steward.

It is ironic that there is only one name on the cover of this dissertation, since so many people have contributed their time and talents to its production. I would first like to thank my advisor, Christopher Goyne, who enabled me to pursue my dream of a career in hypersonics and has been a tireless and patient guide to my research endeavors. From a summer at the U.S. Air Force Research Laboratory to bringing me to the University of Virginia in the first plane, he has provided me with unequalled opportunity, and I will owe any success of mine in this field to him. Additionally, I've appreciated how he not only tolerated but encouraged my flying lessons, and allowed me to freely rifle through his mailbox in search of the latest Aviation Week or Aerospace America to read during lunch. Some day we'll go flying together, even if substantially below Mach 5.

Although not an official advisor, James McDaniel has been an invaluable mentor throughout my graduate education. He should have been suspicious when I spent most of my interview with him asking about his flying career instead of research, but he gave me the benefit of the doubt and I am all the better for it. Additionally, he gave me my first logbook, no small gift to a would-be pilot. I may not follow in his footsteps as a C-130 pilot, but I would be thrilled to become half the researcher.

Harsha Chelliah was similarly an unofficial advisor, teaching not only the bulk of key courses I have taken here but also invaluable lessons about what it means to think like a researcher. I owe my knowledge of multiphase and turbulent flow to Eric Loth, who along with George Cahen and Matthew Reidenbach guided my research as a member of my advisory committee. The seventh member of my committee (tempted fate, I did) is Campbell Carter of the U.S. Air Force Research Laboratory (AFRL), who has been an indispensable guide to my work not only at AFRL but here at UVa as well. I have learned a great deal from him not only about how to address a research question, but how to effectively express the findings in writing. On a number of occasions he has additionally located, modified, and shipped critical parts that enabled this research to be completed.

It is hard to believe that I spent not even three months at AFRL, where I learned so much from so many at a world-leading institution. It was a privilege to perform research alongside Mark Hagenmaier, Kuang-Yu Hsu, Timothy Ombrello, and Scott Peltier. William Terry and David Schommer were superb in configuring and running the wind tunnel through both first and second shifts, and I particularly appreciate the personnel of the Component Air Research Facility for their support of our operations late into the night. Gary Streby provided engineering drawings for the experimental campaign, and numerous other uniformed and civilian Aerospace Systems Directorate personnel ensured our efforts were successful.

At UVa, Robert Rockwell has been indispensable as our in-house research scientist, handling all aspects of wind tunnel operation and experimental planning. For 62 years Edwin Spenceley has provided the highest standards in machining and fabrication, and still comes in to work every day before anyone but the birds (who eagerly await his distribution of birdseed). Ed has built a number

of parts for both the tunnel and my specific experiments, and I cannot express how valuable having such a skilled machinist a few steps down the hall has been. He is a friend not only to the people who work here but also to the animals who call the back lot of our lab home: a stray cat he tended through a winter became the one I adopted.

Scott Rorrer and Richard Roberts, Jr. were exceptional in configuring electrical service for research equipment, and Kevin Knight and Lewis Steva provided several critical tools and resources during these experiments. Brian Connolly generously loaned his group's laser for one set of experiments. Richard White performed electron microscopy of graphite tracers, which subsequently made a mess in Vladimir Mitkin's shock tube I can't quite understand how he could forgive. Wade Komisar's IT support has been invaluable. Brenda Perkins, Jacqueline Slaughter-Scott, Lindsay Grubbs, Laura Troutman, and Barbara Graves all made sure that paperwork and funding moved as it should. Andrew Koch and William Pease have provide a welcome respite from the workday with their tolerance of an unusually-old student in their ensembles. Even though I've never met him in person, Bernard Grossman of Virginia Tech (emeritus) has been a critical influence in my education, teaching online courses in high-speed aerodynamics with clarity and rigor. Much of the success of these experiments is owed to Steve Anderson of LaVision, Inc., who has always answered my sometimes-intelligent questions with sound guidance. Albert Tamashausky of Asbury Carbons gave generously of his time and expertise to ensure the success of his firm's products in a rather unusual application.

It has been a privilege to work at UVa with Andrew Cutler of George Washington University, and Patton Allison (Go Blue!) and Kraig Frederickson of Ohio State University. Fellow graduate student coauthors were Ryan Johnson of UVa and Luca Cantu and Emanuela Gallo of George Washington University (Luca and Emanuela brought high standards not only to their research but to laboratory cuisine as well). Although we haven't shared a paper, my graduate work has benefited from collaboration with a number of other students. Chad Smith was patient and thorough in teaching me the dark art that is PIV in my first summer here, and working with Brian Rice taught me a great deal about not only PIV but the research process as a whole. April Anlage provided invaluable assistance in experimental design and background research on scramjet blowout, and Dominic Barone wrote code to make the plots in this dissertation look professional (even if the data within them do not). Dom taught me not only a good deal about AFRL and L^AT_EX, but also that not all Ohioans are Buckeyes. Even through we did not directly perform experiments together, I have enjoyed the company of fellow graduate students Erin Reed, Joshua Codoni, Kristin Busa, Michael Smayda, David Barnes, Thomas Steva, Junji Noda, Eric Cecil, Benjamin Tatman, Damien Lieber, Clayton Geipel, Stephen Jamison, Gregory "De'Veon" Simms (Go Blue!), and Ujuma Shrestha (I can't believe I let you beat me to the defense, Dr. Shrestha).

My engineering education began at the University of Michigan, where I had the privilege of learning from a number of outstanding professors, but a few merit particular mention for their specific contributions. I was already certain I would pursue aerospace propulsion as a career by the time I first attended a Timothy Smith class, but his dedication to his students and enthusiasm for the subject made him an exceptional instructor even relative to the already-high standards of the department. John Shaw served not only as my academic advisor but also taught some of the most challenging and rewarding classes I have taken, and I hope this dissertation might make me an "enthusiast" by his standards. Though I only took one class from each, Krzysztof Fidkowski and James Driscoll similarly went far beyond the basic call of an instructor. The late Pierre Kabamba ensured that my first aerospace engineering course was as enjoyable as it was rigorous, as he inspired all in his class to become "astute" engineering students. Alec Gallimore and Matthias Ihme gave me my first opportunities in research, and I am indebted to them as well as their then-graduate students Raymond Liang and Yee Chee See, who sacrificed much of their time to guide my efforts. In my pre-college years, Russell Conner, Allwyn Cole, Janet Kapala, and Sarkis Halajian were particularly influential members of an exceptional group of teachers.

The senior members and cadets of the Civil Air Patrol Monticello Composite Squadron have

demonstrated time and time again what it means to be a “professional volunteer,” and our endeavors in aviation and rocketry were the highlights of my years in Virginia. I owe no small debt of gratitude to the countless individuals who have contributed to the L^AT_EX package, without which compilation of this dissertation and several of its constituent publications would have been quite unpleasant. I am one of thousands of engineering students who have appreciated John Anderson’s lucid writings in not only aerodynamics but its history as well. In our single meeting, the late Ed Lewis of NASA provided indispensable advice to an aspiring engineer about to begin his college education.

I cannot sufficiently describe the privilege it has been to study at the University of Virginia. To all members of this exceptional institution, I am sincerely thankful, and I will soon be able to say “I have worn the honors of Honor, I graduated from Virginia.”

The most credit of all is owed to my family, who have provided unwavering support throughout my education, though not all lived to see its formal completion. May this work be in honor and remembrance of them.

Contents

Abstract	i
Acknowledgments	ii
List of Figures	vii
List of Tables	ix
Nomenclature	x
1 Introduction	1
1.1 Scramjet Propulsion	1
1.2 Velocimetry	3
1.3 Scientific Objectives	5
2 Experimental Facilities and Techniques	7
2.1 Direct-Connect Scramjet Test Facilities	7
2.1.1 AFRL RC19	7
2.1.2 UVaSCF	8
2.2 Particle Image Velocimetry	9
2.2.1 PIV Technique Overview	9
2.2.2 PIV Systems	10
3 Flameholder Center Plane: Inlet Distortion	12
3.1 Introduction	12
3.2 Experimental Approach	13
3.2.1 Experimental Facility	13
3.2.2 Particle Image Velocimetry	15
3.3 Results	18
3.3.1 Jet $\bar{q} = 0$	20
3.3.2 Jet $\bar{q} = 0.7$	22
3.4 Conclusions	24
4 Graphite Tracers for Velocimetry	25
4.1 Introduction	25
4.2 Tracer Selection	26
4.2.1 PIV Configuration	26
4.2.2 Trials of Candidate Tracer Materials	26
4.3 Tracer Characterization	30
4.3.1 Sampling	30

- 4.3.2 Electron Microscopy 30
- 4.3.3 Aerodynamic Response 33
- 4.3.4 Thermophoretic Response 36
- 4.4 Conclusions 37

- 5 Flameholder Center Plane: Dual-Mode 38**
- 5.1 Introduction 38
- 5.2 Experimental Approach 39
 - 5.2.1 Experimental Facility 39
 - 5.2.2 Particle Image Velocimetry 40
- 5.3 Results 44
- 5.4 Conclusions 53

- 6 Flameholder-Main Duct Interface: Dual-Mode 55**
- 6.1 Introduction 55
- 6.2 Experimental Approach 56
- 6.3 Results 60
- 6.4 Conclusions 77

- 7 Flameholder Center Plane: Lean Blowout 79**
- 7.1 Introduction 79
- 7.2 Experimental Approach 80
- 7.3 Results 81
- 7.4 Conclusions 88

- 8 Conclusions 90**
- 8.1 Summary of Findings 90
- 8.2 Recommendations for Future Work 92

- References 93**

List of Figures

1.1	Schematic of a typical trapezoidal cavity flameholder	2
2.1	Schematic of RC19 flowpath	8
2.2	Schematic of UVaSCF	9
2.3	Schematic of PIV interrogation window displacement procedure	10
3.1	Shadowgraph imaging of RC19 combustor with a 7° shock-generating wedge	14
3.2	Schematic of inlet distortion experimental configuration	16
3.3	Effect of tracer injection on RC19 wall pressure	19
3.4	Mean velocity magnitude, inlet distortion	20
3.5	Root-mean-square velocity magnitude, inlet distortion	21
4.1	Raw PIV image of TiO ₂ tracers in UVaSCF, injection at x/h=-14	26
4.2	Raw PIV image of TiO ₂ tracers in UVaSCF, injection at x/h=-1.0	27
4.3	Raw PIV image of TiO ₂ tracers in UVaSCF, vibration source active	27
4.4	Raw PIV image of graphite tracers in UVaSCF, $T_0 = 1200$ K, $\phi = 0$	29
4.5	Raw PIV image of graphite tracers in UVaSCF, $T_0 = 1200$ K, $\phi = 0.40$	30
4.6	Raw PIV image of graphite tracers in UVaSCF, $T_0 = 300$ K, $\phi = 0$	30
4.7	SEM image of graphite tracer particles	31
4.8	Histogram of graphite flake length	32
4.9	Histogram of graphite flake thickness	32
4.10	Stokes number of graphite tracers, constant aspect ratio	35
4.11	Stokes number of graphite tracers, constant thickness	36
5.1	UVaSCF steady-state wall static pressure measurements	41
5.2	Experimental schematic, UVaSCF center plane, steady-state	42
5.3	Effect of tracer injection on UVaSCF wall static pressure distribution	43
5.4	Uncertainty of mean velocity, UVaSCF center plane, case 4	44
5.5	OH PLIF intensity, UVaSCF center plane, case 4	45
5.6	Instantaneous velocity magnitude and swirling strength, UVaSCF center plane, steady-state	46
5.7	Mean velocity magnitude, UVaSCF center plane, steady-state	48
5.8	Mean swirling strength, UVaSCF center plane, steady-state	49
5.9	Variance of axial velocity, UVaSCF center plane, steady-state	50
5.10	Variance of transverse velocity, UVaSCF center plane, steady-state	50
5.11	Covariance of axial and transverse velocities, UVaSCF center plane, steady-state	51
6.1	Experimental schematic, UVaSCF cavity top plane	56
6.2	Raw PIV images, UVaSCF cavity top plane, case 1	58
6.3	Raw PIV images, UVaSCF cavity top plane, case 4	58

6.4	Correlation uncertainty of mean velocity, UVaSCF cavity top plane	61
6.5	Correlation uncertainty of variance of velocity, UVaSCF top plane	62
6.6	Instantaneous velocity, UVaSCF top plane, case 1	63
6.7	Instantaneous velocity, UVaSCF top plane, case 4	64
6.8	Instantaneous velocity, UVaSCF top plane, case 5	65
6.9	Instantaneous velocity, UVaSCF top plane, case 6	66
6.10	Mean axial velocity, UVaSCF top plane	68
6.11	Variance of axial velocity, UVaSCF top plane	69
6.12	Variance of spanwise velocity, UVaSCF top plane	70
6.13	In-plane turbulence intensity, UVaSCF top plane	71
6.14	Mean swirling strength, UVaSCF top plane	72
6.15	Comparison of mean axial velocity in center and top planes	74
6.16	Comparison of variance of axial velocity in center and top planes	75
6.17	Comparison of mean swirling strength in center and top planes	76
7.1	Schematic of experimental configuration for LBO measurements	81
7.2	Pre- and post-LBO wall static pressure measurements	82
7.3	Equivalence ratio history of lean blowout	83
7.4	Combustion imaging during LBO transient	83
7.5	LBO mean velocity, 10 ms averaging length	84
7.6	Vector field-raw image pairs between 10 and 6 ms prior to LBO	85
7.7	Vector field-raw image pairs, 5 ms prior to LBO	86
7.8	Vector field-raw image pairs post-LBO	87
7.9	LBO root-mean-square velocity magnitude, 10 ms averaging length	89

List of Tables

- 2.1 Summary of PIV system specifications 11

- 3.1 Test conditions, RC19 inlet distortion measurements 15
- 3.2 Sources of uncertainty of inlet distortion measurements 18

- 5.1 Test conditions, UVaSCF steady-state measurements 40
- 5.2 Turbulence intensity at combustor entrance, UVaSCF center plane, steady-state . . . 51
- 5.3 UVaSCF integral length scales at point $x = -0.8$ mm, $y = 3.3$ mm, case 4 52
- 5.4 UVaSCF integral length scales at point $x = -0.8$ mm, $y = 3.3$ mm, case 5 52

Nomenclature

μ	Dynamic viscosity
ϕ	Equivalence ratio
ρ	Density
τ_D	Domain time scale
τ_p	Particle response time
l_D	Domain length scale
N	Sample size
St	Stokes number
u	Axial velocity
u_D	Characteristic velocity
V	Velocity magnitude
v	Transverse velocity
w	Spanwise velocity

Chapter 1

Introduction

1.1 Scramjet Propulsion

Supersonic combustion ramjets (scramjets) are seen as the most promising means of powering hypersonic aircraft and atmospheric stages of reusable space launch systems. The broader category of ramjets dispenses with the system of mechanical compression of air characteristic of gas turbines and instead uses the deceleration of high-velocity incoming air to achieve the same effect.¹ Although mechanically simple, this method of operation precludes the generation of any meaningful thrust until a flight vehicle has gained sufficient speed, usually at least a large fraction of Mach 1. Ramjet propulsion was first proposed in 1913 by Frenchman Rene Lorin, who at the same time discounted its practicality due to the required airspeeds, perhaps understandable at a time only a decade removed from the Wright Brothers' first powered flight. The ramjet in fact conceptually predates the gas turbine, since it was only eight years later that the turbojet was offered as a solution to this limitation.^{1,2} Patents for ramjet-propelled artillery shells and a concept very similar to modern ramjets were issued in 1926 and 1928, respectively, and the first ramjet ground tests were conducted by Rene Leduc in France in the early 1930s,² contemporaneous with Soviet flight tests of artillery-fired ramjets.³

Soviet researchers are also reported to have performed the first tests of a ramjet on a piloted aircraft, occurring between 1939 and 1940 with the aim of improving the performance of a Polikarpov propeller-driven biplane fighter.^{3,4} In 1945 ramjets were tested on the wingtips of a North American P-51 fighter, and a year later a Lockheed P-80 was similarly modified and achieved the first sustained flight solely on ramjet power.^{1,4} The distinction of the first aircraft to be powered exclusively by a ramjet belongs to the Leduc 010, launched from a carrier aircraft in France in 1949.^{1,2} In the following decade French efforts produced the Nord-Aviation Griffon II, which combined a turbojet with a concentric ramjet sharing a common inlet and exhaust to produce thrust from static conditions up to a top speed of Mach 2.1.^{1,5}

Cold War defense programs prompted considerable investment in ramjet technology, yielding both research vehicles and deployed weapons systems.¹ The Lockheed X-7 unmanned research aircraft served as a ramjet testbed between 1951 and 1960, reaching Mach numbers as high as 4.3.⁶ The United States deployed two ramjet-powered surface-to-air missiles: the eponymous product of the Boeing-Michigan Aeronautical Research Center (BOMARC) guarded the homeland against Soviet strategic bombers, while the Bendix Talos provided fleet defense for the Navy.¹

A fundamental limitation of pure ramjets results from their deceleration of incoming air below the speed of sound prior to combustion, leading to molecular dissociation that severely limits performance at flight Mach numbers greater than approximately four.⁷ The idea of avoiding such effects by maintaining supersonic flow throughout the engine was first proposed in 1946, and serious theoretical and experimental scramjet work was underway by the late 1950s.⁸ In the following

decade numerous ground-test programs and several attempts at atmospheric demonstrations were conducted,^{8–10} but it was not until 2002 that a scramjet was proven in flight, riding past Mach 7 on the nose of a sounding rocket over the Australian outback.¹¹ The first flight of an aircraft under scramjet power came two years later in the United States, with the X-43 unmanned research vehicle reaching Mach 9.7 in its final test.¹²

Current scramjet technology falls into two general categories: hydrocarbon-fueled designs suitable for flight Mach numbers between approximately three and seven, and hydrogen-fueled designs optimized for higher Mach numbers, potentially in excess of fifteen.^{12,13} Of the former, most concepts feature the ability to operate in a mixed subsonic-supersonic “dual-mode” regime, in addition to pure supersonic conditions.¹ This allows a dual-mode scramjet (DMSJ) to operate near the flight Mach 3 limit of conventional gas turbines, a regime where a pure scramjet would not generate sufficient thrust to accelerate a flight vehicle (since no ramjet of any kind can generate static thrust, many concepts for scramjet-powered vehicles feature gas turbines that accelerate a vehicle from a runway takeoff up to the point of scramjet takeover).

DMSJ designs achieve subsonic flow at the combustor entrance by using thermal choking to support a pre-combustion shock system, which is distinct from the shocks and expansion waves created by the engine inlet. The lower internal flow speeds found in a DMSJ allow for the longer chemical induction times of hydrocarbon fuels, which present far fewer logistical challenges to vehicle developers and operators than does the cryogenic hydrogen required to meet reaction rate and structural cooling needs at higher speeds.^{4,8} The heat-sink abilities of hydrocarbon fuels may however be enhanced by promotion of endothermic reactions that convert long-chain molecules into smaller products that have the added benefit of faster reaction rates than their precursors.¹⁴

The short chemical time scales of hydrogen allow for simple ramp-type fuel injectors,¹⁵ but those of hydrocarbons, whether in the form of a raw fuel such as JP-7 or its endothermically-altered products, are too long for the mean residence time of such a flowpath, even at dual-mode flow speeds. To rectify this, cavity flameholders have been identified as a means of providing a low-speed recirculating reservoir of radicals and other hot combustion products that pilot main-duct reactions.¹⁶ Designs have been identified that provide good acoustic stability and fuel-air mixing while minimizing total pressure losses.^{16–18} The spanwise center plane of a typical cavity flameholder geometry is depicted schematically in Fig. 1.1, featuring vertical upstream and sloped aft faces, and containing two recirculation regions.

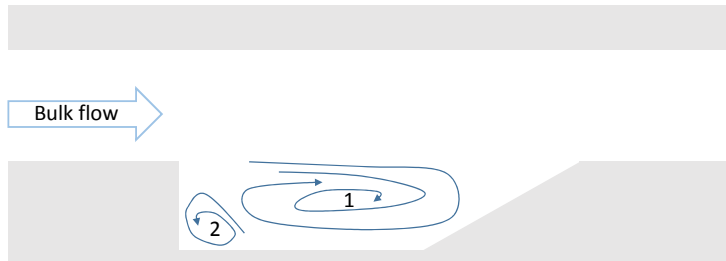


Figure 1.1: Schematic of a typical trapezoidal cavity flameholder showing primary (1) and secondary (2) recirculation regions.

Given the expense of flight testing at hypersonic speeds, the majority of scramjet experimentation is conducted in ground-based facilities. These include freejet wind tunnel configurations, where a partial or complete flight vehicle model is exposed to flight-like freestream conditions,^{19,20} but the majority of work has occurred in the direct-connect regime. This concept dispenses with the

well-characterized inlet and exhaust nozzles of a complete scramjet flowpath and instead supplies air directly to the combustor section, where the majority of outstanding research questions reside.⁴ Among the advantages over the freejet configuration are simplified instrumentation access and a substantially reduced total air flow requirement, both of which lower the still-considerable costs of ground testing.^{1,21,22}

Direct-connect facilities offer flow durations ranging from the order of milliseconds to seconds or even hours, and have become the preferred means of investigation of supersonic combustion phenomena, with freejet testing primarily reserved for full-flowpath analysis.^{1,23,24} One disadvantage of the direct-connect environment is that most implementations do not reproduce the shock waves and expansion fans that would be produced by a flight vehicle inlet and ingested by the engine, altering the fundamental aerodynamic state of the flow relative to a notional design point replicated in ground test.^{21,22} Such effects may be quantified by measurements of velocity, which may also be used to examine the turbulent exchange between the cavity and main duct that enables combustion to be sustained. Combustor inflow conditions and optimal fueling strategies will change over the wide ranges of Mach number and altitude expected of a flight vehicle, with the result that it may not be possible to define a single design point representative of the entire flight profile.¹ As a result, it is desirable to characterize flameholder aerodynamics over a series of aerodynamic and fueling conditions, including those near the limits of operability.

1.2 Velocimetry

Traditional probe-type velocimeters such as pitot probes^{25–29} and hot wire anemometers^{30,31} have been applied to scramjet ground test facilities, but the high-enthalpy and confined nature of these flows limit the utility of these methods due to the potential for damage to the probe and unacceptable disturbance to the velocity field of interest. Laser-based optical diagnostics have proven the overwhelming choice of researchers in recent decades, and these have included, in order of first application, laser Doppler velocimetry (LDV),^{32,33} planar Doppler velocimetry (PDV),^{34,35} and particle image velocimetry (PIV).^{15,36–45} Of these, PIV has nearly completely displaced its predecessors in publication frequency, a trend reflective of the whole of fluid dynamics research.⁴⁶ This may be attributed to the unique ability of PIV to provide both instantaneous and ensemble-averaged planar measurements at high spatial resolution.^{15,46} Additionally, PIV requires only a single laser sheet and one or two cameras to measure two or three components of velocity, respectively. Given the limited optical access of most scramjet flowpaths, this is an advantage over laser-induced fluorescence velocimetry, which requires either one camera or laser sheet per component of velocity measured, arranged in a mutually orthogonal configuration.^{15,47}

A key consideration for any velocimetry technique is the range of spatial and temporal scales that may be captured. Relevant length scales extend from Kolmogorov scales up to flowpath dimensions, and times scales similarly span the range from Kolmogorov scales to those representing transient operations such as a blowout or mode transition.^{4,46,48} The spatial and temporal resolution of a particular velocimetry system are largely decoupled, with some compromises to be made, for example, in the use of a high-speed intensified camera to capture low-intensity signals at high frame rate at the expense of reduced spatial resolution.⁴⁹ Regardless, the two questions will be addressed separately in this analysis.

Turbulence may be considered to consist of a transfer of energy from large spatial and temporal scales characteristic of a particular flowfield boundary down through the Kolmogorov scales, where the inviscid motion of larger scales is dissipated to thermal energy through viscous action.⁴⁸ A correlation function may be defined to relate velocity fluctuations across space and/or time,

$$r(\mathbf{x}, \mathbf{X}, t, \tau) \equiv \frac{\overline{u(\mathbf{x}, t) u(\mathbf{x} + \mathbf{X}, t + \tau)}}{\overline{u^2(\mathbf{x}, t)}} \quad (1.1)$$

where u is any component of velocity, \mathbf{x} is a point in space, \mathbf{X} is a displacement vector, t is a moment in time, and τ is a temporal displacement. Integral scales have magnitudes between the Kolmogorov and outer scales, and represent the spatial or temporal extent of velocity correlation, defined respectively as

$$l_\Lambda = \int_0^\infty r(\mathbf{x}, X\mathbf{e}, t, 0) dX \quad (1.2)$$

where \mathbf{e} is a unit vector in the direction of interest, and

$$\tau_\Lambda = \int_0^\infty r(\mathbf{x}, 0, t, \tau) d\tau \quad (1.3)$$

Integral length scales have been measured in turbulent low-speed laboratory flames to be on the order of 1-10 mm,⁵⁰ a result found to describe scramjet flows as well: Rice⁵¹ measured scales between 2 and 6 mm in a PIV investigation of a hydrogen-fueled flowpath, and Ramesh et al.⁵² predicted a scale of 5 mm in a numerical simulation of a hydrocarbon-fueled flowpath examined in the present work. Such scales are well within the range of present PIV applications, unlike the much smaller Kolmogorov scales, which like all turbulent scales are specific to a particular flowpath and operating condition but in most cases are expected to be smaller than 0.1 mm.⁵³ An estimate of the Kolmogorov scale λ_k may be found^{46,54} via the integral length scale, root-mean square velocity u_{rms} , and kinematic viscosity ν :

$$\lambda_k = \frac{\nu^{3/4} l_\Lambda^{1/4}}{u_{rms}^{3/4}} \quad (1.4)$$

Using this relation in conjunction with the results of Ramesh et al.,⁵² the Kolmogorov length scale is estimated for the flowpath of the present study as 0.01 mm, of the same order of magnitude as measurements of turbulent low-speed flames.⁵⁰ It must be kept in mind that in order to resolve any particular spatial scale, the Nyquist criterion requires that the measurement system achieve a resolution at least twice as fine.⁴⁹ It is important to note that most turbulent combustion phenomena of interest occur at the integral scale or larger,^{55,56} whereas measurements at the Kolmogorov scale are primarily of utility only to turbulence spectra studies.⁵⁴ Current PIV implementations achieve spatial resolutions better than half a millimeter^{42,56} and thus may adequately capture relevant spatial dynamics.

Apart from transient operations such as a steady change in fueling rate, which can be of arbitrary duration, the largest time scales of interest in scramjet research are those representing thermoacoustic instabilities and combustion mode transition. Fotia et al. measured a 5 Hz pressure oscillation resulting from a flame-shock interaction,⁵⁷ and oscillations in the range of 100-500 Hz have been measured by others.^{58,59} For the flowpath of the present study, Ramesh et al. predicted through numerical simulation a peak oscillatory amplitude at 360 Hz,⁵² and combustion radical measurements have indicated that the lean blowout process occurs on the order of a millisecond.⁶⁰

More challenging to capture are the integral and Kolmogorov time scales, which are on the order of tens to hundreds of kilohertz in turbulent flames^{53,61} To the author's knowledge measurements of these time scales have not been reported in scramjet flows, but estimates may be made using results of numerical simulations. The integral time scale may be approximated as the ratio of the integral length scale and the mean convective velocity,

$$\tau_\Lambda = \frac{l_\Lambda}{U} \quad (1.5)$$

and the Kolmogorov time scale as⁴⁶

$$\tau_k = \sqrt{\frac{\nu l_\Lambda}{u_{rms}^3}} \quad (1.6)$$

Using these approximations and the results of Ramesh et al.,⁵² the integral and Kolmogorov time scales are estimated as 70 and 500 kHz, respectively. Resolving such scales clearly requires capabilities beyond even the 3 kHz acquisition rate maximum in reported scramjet velocimetry studies.⁴⁵

Given that PIV scramjet studies have adequately resolved relevant spatial scales but have not yet reported time-resolved measurements of any phenomena, it is desirable to achieve an increase in sampling rate of several orders of magnitude. PIV systems that achieve sampling rates of several kilohertz without sacrificing spatial resolution are available and have been applied to laboratory burners with maximum velocities of tens of meters per second,^{53,55,56,62-77} but only one application to scramjet flows has been published,⁴⁵ which did not attempt to resolve any high-speed phenomena and instead made use of the high acquisition rate to overcome limitations on test duration imposed by velocimetry tracers. A preliminary study⁷⁸ by the present author and colleagues gave only mean results at non-reacting conditions and similarly did not take advantage of the 1 kHz sampling rate to temporally resolve any flow features, instead focusing only on characterizing a new type of velocimetry tracer that removed such limitations, with the ultimate goal of using this high-speed diagnostic to expand the range of resolvable temporal scales in scramjet flows.

Key challenges to the application of high-speed laser velocimetry to scramjet flows include thermal limitations on lasers that necessitate a compromise between repetition rate and energy per pulse, reduced camera resolution at high repetition rate, experimental downtime needed for data transfer from onboard camera memory to computer storage, and computational challenges in processing and extracting relevant results from the large amounts of raw data high-speed systems can generate.⁶¹ An additional limitation is a lack of statistical independence of instantaneous velocity measurements acquired at a rate much greater than the flow frequencies under investigation. Such oversampling can require a greater sample size than would be needed with a lower-rate technique to achieve the same statistical convergence, but this problem is easily avoided with careful selection of sampling rate.

In summary, high-speed PIV systems offer several key advantages relative to conventional diagnostics. These include the ability to temporally and spatially resolve combustion dynamics, analyze transient events such as blowout and combustion instabilities, and acquire statistically significant data sets in duration-limited facilities.^{61,79,80} The present research will focus on measurements above the flowfield oscillation rate but below the integral (and thus Kolmogorov) time scales, allowing for statistically independent measurements of transient phenomena while preserving the ability to acquire mean-flow statistics.

1.3 Scientific Objectives

Scramjet PIV studies have primarily focused on hydrogen-fueled configurations,^{15,36-38,41} with more recent work addressing hydrocarbon fueling.^{39,45} Tuttle et al.³⁹ addressed only the supersonic mode of operation, and velocimetry of a cavity flameholder at dual-mode conditions has not been reported. Additionally, Tuttle et al. encountered substantial accumulation of metal oxide tracer particles on flowpath windows bordering the cavity flameholder, an effect that was found to occur to a much greater extent in the present work.⁷⁸ Such window fouling has been observed in other experiments as well,^{71,81-83} limiting PIV capabilities in applications placing high-enthalpy flow adjacent to windows.

Ignition and blowout limits have been extensively analyzed in scramjets configured with cavity flameholders,⁸⁴⁻⁹⁰ but the dynamics of the process itself have received less attention,^{18,91} and no velocimetry has been reported at this or any other transient condition. Other off-design conditions remain similarly unexplored, with studies of the influence of inlet distortion on combustor aerodynamics in the present work recent exceptions.^{40,42}

To address these shortcomings in the current state of scramjet research, the following scientific objectives were established:

1. Quantify the effect of simulated inlet distortion on cavity flameholder aerodynamics.
2. Extend particle image velocimetry to regions of the scramjet flowpath not accessible with conventional seeding methods by application of novel tracer materials.
3. Characterize cavity flameholder aerodynamics at steady-state dual-mode conditions.
4. Characterize cavity flameholder aerodynamics during the lean blowout transient.

Work relevant to the first objective represents the first published velocimetry of a scramjet ground-test rig with replicated inlet distortion, and the second objective was satisfied with the first reported application of graphite tracers to a high-enthalpy flow. Measurements corresponding to the third and fourth objectives were similarly the first of their kind, and additionally were the first reported in the fully-premixed combustion regime.

This dissertation continues with a chapter describing the direct-connect test facilities used and the experimental techniques applied to them. Chapters addressing these scientific objectives follow, and the dissertation concludes with a summary of key findings and recommendations for future investigations.

Chapter 2

Experimental Facilities and Techniques

2.1 Direct-Connect Scramjet Test Facilities

Two direct-connect scramjet test facilities were used in this study: RC19 was used for examination of the effects of inlet distortion on cavity aerodynamics as presented in Chapter 3, and UVaSCF was used for the remainder of the experiments.

2.1.1 AFRL RC19

U.S. Air Force Research Laboratory Research Cell 19 is a direct-connect continuous-flow non-nitiated scramjet test facility capable of supporting a variety of rectangular flowpath configurations.²⁴ Heating of test gases is provided by a methane-fired heat exchanger, and although the uncooled heat-sink flowpath is capable of indefinite operation under non-reacting conditions, combustion test duration is governed by thermal limits. As used in this study, RC19 consisted of a two-dimensional Mach 3 nozzle followed by a constant-area isolator and a combustor section with a divergent floor. A full-span cavity flameholder was located in this divergent section, and the floors of these two components had the same 2.5° divergence relative to the upper wall. The forward and aft faces of the cavity formed angles of 90° and 157.5°, respectively, with the floor.

Figure 2.1 presents a side view of this flowpath relative to the axes chosen, where the streamwise direction x is parallel to the isolator centerline, y is perpendicular to the isolator floor, and the spanwise direction z completes the right-handed coordinate system. The coordinate origin was placed at the top of the cavity forward face along the spanwise centerline, and the bulk flow direction was from left to right. The isolator had a height of 50.8 mm and a span of 152 mm, and the length and depth of the cavity were 66.0 and 16.5 mm, respectively.

To simulate the aerodynamics of fuel injection, air was introduced through a sonic jet injector with an exit diameter of 3.2 mm in the flowpath floor upstream of the cavity, denoted with an arrow in Fig. 2.1. The injector was oriented normal to the floor and located on the tunnel centerline at $x = -13.5$ mm. The operation of the jet injector is characterized by the ratio of its momentum flux to that of the main-duct flow:

$$\bar{q} = \frac{(\rho V^2)_{jet}}{(\rho V^2)_{\infty}} \quad (2.1)$$

Here, ρ and V represent density and velocity magnitude, respectively. In this study, the value of the momentum flux ratio was either 0 (jet off) or 0.7.

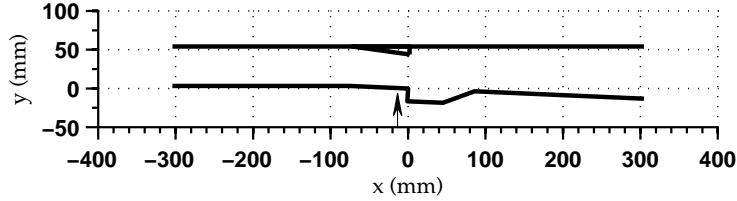


Figure 2.1: Side view of RC19 flowpath with distortion generator wedge at most-downstream location.

In order to re-create the effects of nonuniform flow produced by a flight vehicle inlet, a full-span 8° wedge 74 mm in length was available for installation on the upper surface of the flowpath. Instead of replicating the entire distorted flowfield expected within an engine in flight or freejet testing, this device produced a single shock in the vicinity of the flameholder, representing the propagation of a shock originating at the lip of the engine inlet.²⁷ 76 mm of travel in the streamwise direction was available, and the distorted-flow cases placed the leading edge of the wedge at $x = -72$ mm, $x = -104$ mm, and $x = -142$ mm. These locations correspond to the resulting oblique shock wave impinging on the cavity, the jet injector, and a location upstream of the jet injector, respectively.

2.1.2 UVaSCF

The University of Virginia Supersonic Combustion Facility (UVaSCF) is a continuous-flow nonvibrated direct-connect scramjet test facility incorporating a modular rectangular flowpath. Oil-free, dehumidified air is supplied by a compressor to a 14-stage, 300 kW electric resistance heater, ensuring air entering the test section is free of contaminants and has composition representative of atmospheric flight.²³ The nozzle and test section are water-cooled, ensuring test duration at reacting conditions is limited only by the capacity of the fuel storage system. The flowpath configuration used in this study is depicted in Fig. 2.2, where the coordinate origin and orientation are the same as defined for RC19.

A two-dimensional Mach 2 facility nozzle led to an isolator section, which contained the pre-combustion shock system and had a constant height (y -direction) of 25 mm and width (z -direction) of 38 mm. It was followed by a combustor with a 2.9° divergence of the wall on which a trapezoidal cavity flameholder was located. The cavity floor was parallel to the divergent wall, and formed angles of 90° and 157.5° with the forward and aft cavity faces, respectively. A constant-area section followed, facilitating the formation of a thermal throat, and the most-downstream section resumed the 2.9° divergence of the cavity-side wall and led to an atmospheric exhaust. In the subsequent discussion flowpath dimensions will be normalized by the cavity depth of 9.0 mm, denoted h .

Gaseous ethylene fuel was injected through two sets of six wall-normal sonic orifices, one set each on the cavity-side and opposite walls of the isolator, at $x/h = -55$, yielding premixed flow at the combustor entrance.^{87,92} Optical access was provided by sidewall windows occupying nearly the entire extent of the combustor, as well as a 6 mm-wide window extending over most of the streamwise length of the combustor wall opposite the cavity.

The shock system upstream of the combustor section could be maintained independent of the degree of heat release by operation of an air throttle, consisting of a pair of sidewall air injectors located at $x/h=37.5$. Injection of high-pressure air created aerodynamic blockage equivalent to

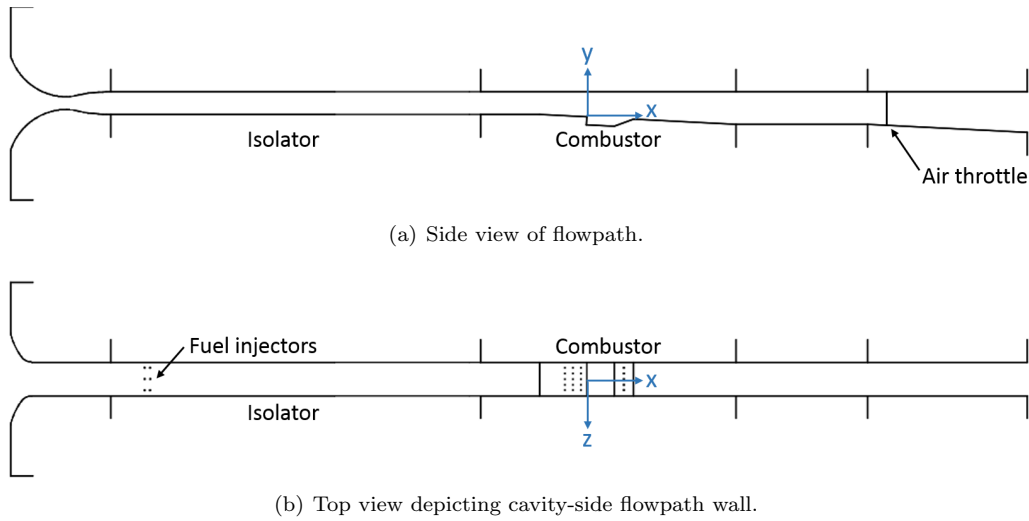


Figure 2.2: Side (a) and top (b) views of flowpath configuration, drawn to scale, with facility nozzle at left and atmospheric exhaust at right.

that resulting from heat release, and allowed the pressure rise upstream of the flame front to be decoupled from the combustion process. This particular configuration allowed for replication of the full range of pre-combustion shock system lengths resulting from heat release alone.

2.2 Particle Image Velocimetry

2.2.1 PIV Technique Overview

PIV is particularly well-suited to scramjet investigations due to its advantages in spatial and temporal resolution over other velocimetry methods, as discussed in Sec. 1.2. Numerous commercial PIV systems are available, and applications of PIV to scramjet flowpaths have been well-documented in the literature.^{15,36–45} Detailed descriptions of the technique have been provided by others,^{46,93–95} and only a summary will be provided here. The PIV method relies on using a pulsed laser sheet to illuminate tracer particles suspended in a flow, and imaging each laser pulse with a dual-frame camera. By comparing the displacement of particles between illuminations at time separations shorter than the flow time scales of interest, flow velocity may be calculated. The method is of course dependent on the particles faithfully tracking the flow and following a linear trajectory between laser pulses. Such characteristics will in most cases never be exactly achieved, but the resultant error is small enough in a well-designed experiment to permit representative results.

Calculation of vector fields is performed via semi-automated numerical routines, with a number of software packages available to investigators. Most implementations divide the imaged measurement plane into rectangular interrogation windows, then spatially shift the corresponding windows of the first and second frames (commonly denoted A and B, respectively) of an image pair until the optimal correlation between images is found. This process may be repeated for subdivisions of the initial interrogation windows, using the calculated displacement vectors to guide the search for those in the smaller windows. Such processing routines allow PIV to examine velocity fields with dynamic ranges exceeding two orders of magnitude.⁴⁶ This process is depicted schematically in Fig. 2.3, where the interrogation window boundaries are depicted as a box and particles as circles.

Stereoscopic PIV (SPIV) allows the measurement of the out-of-plane component of velocity by imaging the measurement plane from two distinct perspectives. A three-dimensional spatial

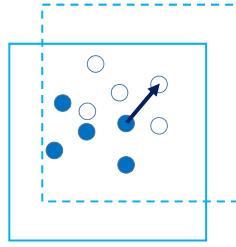


Figure 2.3: Schematic of PIV interrogation window displacement procedure. Displacement vector (arrow) depicts relative particle motion between frames A (solid box and circles) and B (dashed box and open circles).

calibration function generated prior to vector computation is used to match corresponding two-component vectors from each camera, making use of the difference in apparent displacements to determine complete three-component vectors.^{93,94}

2.2.2 PIV Systems

Three PIV systems are available for use in the present work, the specifications of which are summarized in Table 2.1. System 1 was used for work completed at the U.S. Air Force Research Laboratory, and systems 2 and 3 were used at the University of Virginia, as will be described in subsequent sections. Systems 2 and 3 can acquire three-component measurements, whereas system 1 is limited to the two components parallel to the measurement plane. Successful PIV measurements are dependent on precise synchronization of the laser light source with image acquisition. A Stanford Research Systems DG535 delay generator was used for this purpose with PIV system 1, whereas system 2 used a LaVision programmable timing unit, and system 3 used a LaVision high-speed controller.

All systems use variants of a fluidized bed seeder to levitate and disperse the tracer particles. Such seeders house particles in a vertical cylinder, to which air is introduced at the bottom through a porous plug, levitating the particles and propelling the smallest of them to exit an orifice in the top of the chamber.⁹³ The seeder used with PIV system 1 was manufactured by Innovative Scientific Solutions, Inc., and that used with PIV systems 2 and 3 was produced in-house at the University of Virginia Aerospace Research Laboratory. The output of each seeder was ducted to an injection port in the scramjet test section.

A system of lenses was used to convert the axisymmetric output of the laser into a sheet suitable for planar illumination of PIV tracers. The laser beam of PIV system 1 was first passed through a pair of spherical lenses to increase the beam diameter, then through a polarizing beam splitter cube to adjust intensity, and finally through a negative focal length cylindrical lens followed by a positive focal length spherical lens to form the beam into a sheet. PIV system 2 used two pairs of cylindrical lenses to independently control laser sheet width and thickness, with each pair consisting of one lens of negative focal length to expand the beam and another of positive focal length to provide collimation. A set of integrated optics produced by LaVision was used with PIV system 3, and incorporated a pair of spherical lenses followed by a single cylindrical lens.

	System 1	System 2	System 3
Camera model	PCO 1600	LaVision Imager Pro X 2M	Photron SA 1.1
Camera type	CCD ²	CCD	CMOS ³
Camera maximum frame rate ¹ (Hz)	15	14	2700
Camera resolution (pixels)	1600 × 1200	1600 × 1200	1024 × 1024
Camera pixel size (μm)	7.4 × 7.4	7.4 × 7.4	20 × 20
Laser model	New Wave Solo-III	Spectra Physics PIV-400	Photonics DM50-527DH
Laser type	Nd:YAG	Nd:YAG	Nd:YLF
Laser wavelength (nm)	532	532	527
Laser maximum repetition rate (Hz)	15	10	5000
Laser maximum power (mJ/pulse)	50	400	55
Measurable velocity components	2	3	3
Control and processing software	LaVision DaVis 8	LaVision DaVis 7	LaVision DaVis 8

¹ Double-frame, full resolution

² Charge-coupled device

³ Complementary metal-oxide semiconductor

Table 2.1: Summary of PIV system specifications.

Chapter 3

Flameholder Center Plane: Inlet Distortion

3.1 Introduction

The problem of maintaining stable combustion in a supersonic combustion ramjet (scramjet) has led investigators to consider a variety of flameholder designs.^{16,96} Cavity flameholders are widely used in subsonic combustion systems but have received particular attention in scramjet research when used with hydrocarbon fuels.¹⁸ Prior investigations have indicated that such flameholders offer advantages in drag and ignition behavior, but flow instabilities may prevent sustained combustion under some conditions.¹⁶

Cavity flameholders are broadly classified into two categories based on the behavior of the shear layer formed at the upstream face. Cavities for which the shear layer does not reattach to the floor are termed “open,” and those for which the shear layer does are considered “closed.”¹⁶ Shear layer reattachment to the cavity floor generally does not occur for length-to-depth ratios L/D of less than 10, providing an approximate geometric distinction between the two cavity types.^{17,97} Recent work has focused on cavity geometries with an aft face sloped to form a ramp,⁵⁹ and in this case cavity length is taken as the axial distance between the step (forward face) and the midpoint of the ramp.¹⁷

With the X-51A and HIFiRE (Hypersonic International Flight Research Experimentation Program) Flight 2 scramjet vehicles as recent exceptions,^{13,98} research with scramjet cavity flameholders has been largely confined to ground test facilities,¹⁶ which may be divided into two general categories: freejet and direct-connect. Freejet facilities expose complete or partial flight vehicle geometries to flight-like freestream conditions, whereas direct-connect facilities supply air only to the scramjet flowpath itself. Although freejet testing more accurately simulates flight conditions, direct-connect testing greatly reduces cost and simplifies technical requirements for both the test article and facility, allowing for a much greater variety of instrumentation techniques.²¹ Additionally, the direct-connect environment enables testing of flowpaths too large to be accommodated in freejet test facilities.²²

These factors make the direct-connect environment the only practical option for many fundamental studies of scramjet operation, meaning care must be taken to ensure that the flow entering the engine is representative of that which would be produced by a flight vehicle. This is generally not the case, however, since flow delivered by a conventional direct-connect facility has not been processed by the system of oblique shock waves produced by a flight vehicle forebody and inlet, and is free of the consequent series of compression and expansion waves that propagating through the engine. The locations of these waves will change throughout the vehicle flight envelope and may

alter fuel-air mixing and flameholding properties.²⁷

It is thus desirable to simulate this distortion experimentally, and to date several studies have investigated this possibility through the use of an additional facility section installed between the nozzle and scramjet flowpath.^{21,22,27,99} This section, referred to as a distortion generator, replicates the flow nonuniformities produced by a flight vehicle through use of either an asymmetrically-varying cross-section or the inclusion of ramps and/or air injectors. Good agreement between numerical simulations of flight inlets and experimental testing of prototype distortion generators was demonstrated, validating the design approaches used.²² Key differences between distorted and undistorted direct-connect flowpaths were found in pressure and mass flux distributions, implying that optimal fueling strategies may differ significantly between typical ground test configurations and flight vehicles.^{22,27}

Previous experimental investigations of distortion generators have reported only pressure and temperature,^{22,27} and due to the lack of velocity measurements, the flow physics of simulated inlet distortion has been largely unexplored. Furthermore, although velocimetry had been reported for a number of scramjet flows at the time the present work was performed,^{15,36,38,100} only the study of Tuttle et al.³⁹ was known to have examined flow inside a cavity flameholder, and no study had reported cavity velocimetry in the investigation of inlet distortion. (Since the publication⁴² of the present work Peltier et al.⁴⁵ have extended the technique.) Particle image velocimetry (PIV) was selected for the present study due to its ability to provide spatially-resolved data across a planar measurement region, positioning it as an improvement over pointwise techniques such as laser Doppler velocimetry (LDV)¹⁰¹ or lower-resolution planar techniques such as hydroxyl-tagging velocimetry.¹⁰⁰

Given the importance of cavity flameholders to the near-term development of scramjet engines, it is critical that the impact of flight-like distortion on cavity flowfields be understood through the acquisition and analysis of velocimetry. The purpose of this study, which addresses the first scientific objective of this dissertation, is to quantify the effects of several distortion scenarios on flameholder aerodynamics, both with and without simulated fuel injection upstream of the cavity. This work serves as part of a larger investigation into the replication of inlet-generated distortion in direct-connect scramjet component testing, encompassing a variety of techniques to measure chemical and physical flow properties.

This chapter continues with a discussion of the experimental facility, including the development of a means of simulating inlet distortion. Next, the test conditions and diagnostics are detailed, including a quantification of experimental error. Mean and fluctuating velocity data are presented for a combination of distortion and simulated fuel injection conditions, which represent the first reported results of their kind.⁴² The chapter concludes with a discussion of the impact of flow distortion on flameholder aerodynamics.

3.2 Experimental Approach

3.2.1 Experimental Facility

Experiments were conducted in Research Cell 19 of the Air Force Research Laboratory,²⁴ described more fully in Sec. 2.1.1, in a configuration previously characterized using planar laser-induced fluorescence of the OH and NO species.^{102,103} Apart from the inclusion of a distortion generator and the use of a Mach 3 nozzle in place of a Mach 2 equivalent, this flowpath was the same as that studied by Tuttle et al., who found that the shear layer did not reattach to the cavity floor,³⁹ confirming the expected behavior based on the cavity length-to-depth ratio of 4.0. It is, however, important to note that this heuristic does not account for the distorted-flow conditions of this study.

As discussed in Sec. 2.1.1, a full-span wedge was installed at three streamwise stations on the upper wall of the combustor, producing an oblique shock wave that impinged on either the cavity, the jet injector, or a location upstream of the jet injector. The behavior of this shock wave

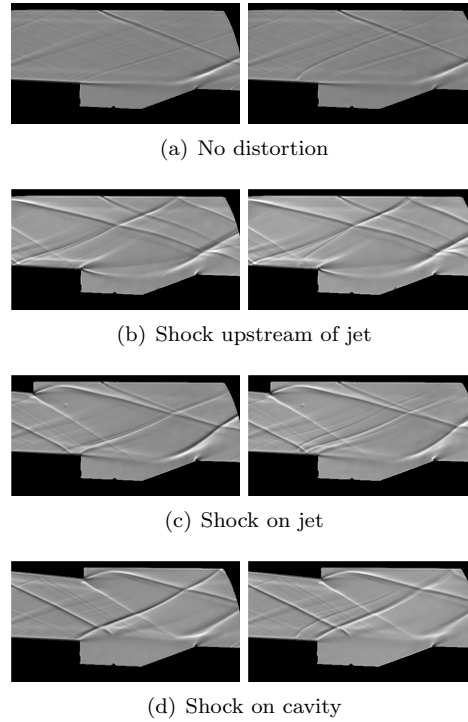


Figure 3.1: Shadowgraph imaging¹⁰² with a 7° wedge for $\bar{q} = 0$ (left) and $\bar{q} = 0.7$ (right) cases.

was confirmed via prior shadowgraph analysis,¹⁰² as seen in Fig. 3.1. Several aspects of these measurements should be noted: first, the wave emanating from the middle of the flowpath upper wall was caused by the edge of a window, which was not reconfigured between test cases. Second, the black spot on the cavity floor represents the masking of a spark plug igniter. Finally, these measurements examined a 7° wedge: to compensate, the axial locations of the wedge in the present study were adjusted such that the shock impingement locations were the same as those resulting from the 7° wedge.

Of particular interest is the behavior of the shear layer spanning the boundary between the cavity and main-duct flowfields, which governs the volume of recirculating flow within the cavity. Shear layer response to flow distortion may be explained by changes to the main-duct pressure field caused by the oblique shock and expansion fan produced by the distortion generator, and the requirement that pressure be constant across the shear layer for equilibrium to be maintained. The baseline undistorted case is free of impinging shocks and expansion fans, and thus the pressure imposed on the cavity is constant along its length, requiring no shear layer deflection to ensure equilibrium. As a result, the shear layer proceeds in nearly a straight line between the upper ends of the forward and aft cavity faces.

When the distortion generator is positioned such that the oblique shock impinges upstream of the jet, the boundary layer upstream of the cavity step is at an elevated pressure relative to nozzle exit conditions, since it has been processed by both the incident and reflected shocks. The cavity is exposed to the negative streamwise pressure gradient resulting from the expansion fan centered about the trailing edge of the distortion generator, and this relatively lower pressure is communicated upstream through the subsonic cavity flow. In order to maintain compatibility between this and the higher pressure of the incoming boundary layer, an expansion fan centered on the upper corner of the step is formed, deflecting the shear layer into the cavity as a result.

Case	Jet \bar{q}	Shock impingement	T ₀ (K)	P ₀ (MPa)
1a	0	None	305	1.21
2a	0	Upstream of jet	306	1.20
3a	0	On jet	304	1.21
4a	0	On cavity	306	1.20
1b	0.7	None	304	1.21
2b	0.7	Upstream of jet	306	1.21
3b	0.7	On jet	304	1.21
4b	0.7	On cavity	306	1.20

Table 3.1: Test conditions for the eight cases examined.

In the shock-on-jet case, the cavity is subject to higher pressures than in the case just discussed, since the cavity is exposed to less of the expansion fan. The incoming boundary layer is at a similar pressure as in the previous case, but the pressure difference between it and the cavity is now smaller. Less flow turning through an expansion fan centered on the cavity step is required to reconcile this smaller pressure difference, and shear layer deflection into the cavity is lessened as a result.

The shock-on-cavity case shows completely different behavior, owing to the lack of an expansion fan impinging on the cavity. The incident shock raises the pressure of the cavity above that of the incoming boundary layer, deflecting flow away from the cavity between the cavity step and shock impingement location. This deflection necessitates an oblique shock that increases the pressure of the incoming flow to match that of the cavity.

Experiments in the present study were conducted at the conditions given in Table 3.1. The test cases were chosen to examine the effects of all combinations of two jet injection conditions and four distortion conditions, the latter consisting of a baseline case without the distortion-generating wedge as well as three cases with the wedge installed at different streamwise locations.

3.2.2 Particle Image Velocimetry

Two-component particle image velocimetry measurements were made with PIV system 1. The measurement plane was aligned with the main duct central axis and located along the spanwise centerline of the flowpath, covering most of the cavity as well as a smaller area of the main-duct flow. Dual-frame images were acquired with a PCO 1600 interline-transfer charge-coupled device (CCD) camera controlled by PCO CamWare software, and fitted with a Nikon Nikkor 60 mm focal length lens set to an f-stop of f/8. A Semrock 532 nm interference filter was installed on the camera lens to reduce the amount of ambient light contributing to image noise. To better fit the field of view (while still preserving spatial resolution) only a subset of the full CCD area was used, with images acquired at a resolution of 1600×780 pixels instead of the full resolution of 1600×1200 pixels. This resolution allowed a maximum of 1069 image pairs to be stored in onboard camera memory for each data acquisition sequence.

Illumination of the tracer particles was provided by a dual-head Nd:YAG laser (New Wave Solo PIV Solo-III), the output of which passed sequentially through a pair of spherical lenses to increase the beam diameter, a polarizing beam splitter cube, and a negative focal length cylindrical lens followed by a positive focal length spherical lens to form the beam into a sheet, with a thickness of approximately 1 mm. Additionally, several dielectric mirrors were used to redirect the laser beam to comply with the physical constraints of the test facility. Windows in the top and side walls of the flowpath provided optical access for the laser sheet and camera, respectively. The polarizing beam splitter directed part of the incident beam into a beam dump and was adjusted such that the average energy that reached the measurement plane was 30 mJ/pulse. The laser was triggered by a Stanford Research Systems DG535 delay generator, which itself was triggered by the

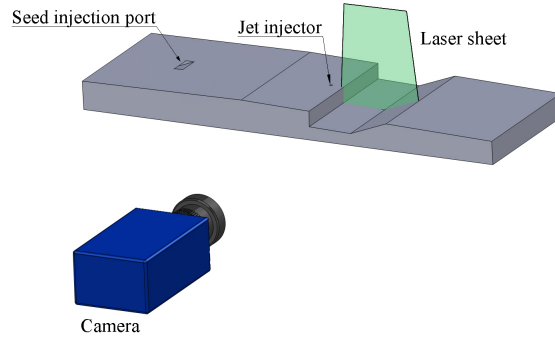


Figure 3.2: Schematic of the experimental configuration. For clarity, the laser delivery system is omitted, and only the lower wall of the flowpath is shown.

camera controller. This configuration maximized framing rate by limiting it only by the camera readout rate. Images were acquired at a rate of 15 Hz, and the delay generator provided a laser pulse separation of $\Delta t = 4 \mu s$. Pulse timing was monitored continuously using a fast photodiode (ThorLabs DET 210) and a digital oscilloscope (LeCroy WaveRunner 44Xi).

Seeding of the cavity flow and bounding shear layer was accomplished with the introduction of TiO_2 particles suspended in dry air through a slot injector in the isolator floor. The particles were spherical, with a 100 nm diameter, and were supplied by American Elements. Additionally, flow through the jet injector was seeded with particles of the same type. Seeded airflow was provided to the slot and jet injectors by independent fluidized-bed seeders manufactured by Innovative Scientific Solutions, Inc.

The slot injector was oriented at 20° relative to the flowpath surface, measuring $\Delta x = 9.3$ mm by $\Delta z = 25$ mm, and was located on the tunnel centerline at $x = -178$ mm. This method of seeding was selected to minimize disturbances to the surrounding flowfield, and provided a low-momentum flow to mix with the boundary layer and become subsequently entrained in the cavity. Additionally, it provided higher tracer density along the spanwise centerline of the cavity than at outboard locations. Thus, tracer density near the windows was much reduced as was the tendency for tracer accumulation on the windows, thereby maximizing run duration. The normal momentum flux ratio of the seeded air with respect to the main-duct flow was estimated to be on the order of 10^{-5} , and it will be shown in the next section that this resulted in an insignificant disturbance to the flowfield. A schematic of this experimental setup is included in Fig. 3.2.

The ability of a suspended particle to faithfully track flow features is described by the Stokes number, defined as the ratio of the particle aerodynamic response time to a domain time scale:¹⁰⁴

$$St = \frac{\tau_p}{\tau_D} \quad (3.1)$$

The domain time scale in turn is taken as the ratio of characteristic domain length to flow velocity:¹⁰⁴

$$\tau_D = \frac{l_D}{u_D} \quad (3.2)$$

In order to ensure a conservative estimate of Stokes number, the smallest length and largest velocity characteristic of the flow should be chosen. Accordingly, the cavity depth of 16.5 mm was taken as the characteristic length scale, and the main-duct velocity from isentropic flow calculations of 630 m/s was taken as the characteristic velocity. These two values represent the mean velocity gradient experienced by a particle as it transits the space between the high-velocity main duct and

the near-zero-velocity cavity interior. Although the local velocity gradient will vary throughout the measurement plane, the chosen time scale represents a conservative (small) value representative of the measurement plane as a whole.

For particles with density much greater than that of the suspending fluid, the particle response time according to the Stokes drag is given by:¹⁰⁴

$$\tau_p = \frac{\rho_p d_p^2}{18\mu} \quad (3.3)$$

where ρ_p and d_p are particle density and diameter, respectively, and μ is the dynamic viscosity of the fluid, which was calculated using Sutherland's formula⁷ based on main-duct fluid properties calculated under isentropic flow assumptions. Using these relations, the Stokes number of the experiment was calculated as 0.012. Samimy and Lele determined that Stokes numbers less than 0.25 provide suitable tracking of compressible flow for velocimetry applications,¹⁰⁵ thus lending confidence to the ability of the particles to adequately represent the flow in this study.

It is important to note that the calculated Stokes number of 0.012 neglects particle agglomeration, which was not quantified in this study, and would serve to increase the Stokes number. Agglomeration was however found to be qualitatively minimal, since camera pixel saturation indicative of reflection from an agglomerated cluster substantially larger than an individual particle was not seen in the raw images. Some agglomeration would not render invalid the present technique: under the conditions of this study, particle clusters up to 450 nm in diameter could form without exceeding the Stokes number criterion of Samimy and Lele.¹⁰⁵

Instantaneous velocity vector fields were calculated with DaVis FlowMaster 8 software using a cross-correlation algorithm. A multi-pass procedure reduced interrogation window size from 128×128 pixels to 16×16 pixels with 50% overlap. With the 16.7 pixel/mm resolution provided by the experimental setup, this yielded 0.48 mm spacing between adjacent vectors. Window shifting was applied at each pass in order to maximize the number of particle pairs within each interrogation window and thus improve the accuracy of the final result. In order to eliminate spurious vectors between successive passes, a median filter and 3×3 smoothing were used. The final vector fields were not smoothed, but a more sophisticated median filter was applied. Ensemble averages (presented in the following section) were calculated using only vectors that fell within 3 standard deviations of the mean value at each location in the measurement plane.

Experimental uncertainty of velocity was taken as the root-sum-square of the systematic and random errors associated with the measurement technique as well as the uncertainty in the mean due to finite sample size. Errors in the measurement technique included those of laser pulse timing and measurement of particle displacement, with particle flow-tracking error neglected due to the aforementioned Stokes number analysis. Laser pulse timing error was calculated as the root-sum-square of jitter in the laser itself (± 1 ns) as well as the delay generator used to trigger it (± 0.4 ns), both quoted from manufacturer specifications. In addition, an error in pulse separation equal to the pulse duration of 10 ns was included.

Particle displacement measurement error was composed of error in the calibration used to create a physical scale for the raw images as well as error of the PIV algorithm in calculating particle displacement. Calibration error is determined by the PIV software as the standard deviation of the imaged mark-to-mark spacing of the calibration target, which for this experiment was 0.019 mm. This error would be expected to vary in proportion to the nominal mark-to-mark spacing of a particular calibration target, since it is a function of the physical uniformity of the target itself as well as distortion introduced by the optical path between it and the camera image sensor. As a result, this source of error was normalized by the nominal mark-to-mark spacing, yielding a percentage which was then applied to the measured particle displacement. Doing so for the 3.2 mm mark-to-mark spacing of the calibration target used presently yielded a 0.61% error in displacement.

It has been shown that cross-correlation algorithms have a displacement calculation error of ± 0.1 pixels,¹⁰⁶ which must be compared to a representative displacement. Although experimental

Source	Type	Value	Unit
Laser jitter	Random	± 1	ns
Delay generator jitter	Random	± 0.4	ns
Laser pulse separation	Random	± 10	ns
Cross-correlation	Random	$\pm 6.0 \times 10^{-3}$	mm
Calibration	Systematic	$\pm 0.61\%$	N/A

Table 3.2: Sources of uncertainty considered in the calculation of overall experimental uncertainty.

uncertainty is often quoted relative to full-scale values, the high dynamic range of the present flow-field makes this approach somewhat misleading, and instead the average of the mean displacements over the entire measurement plane for all cases examined, 12.3 pixels (corresponding to 184 m/s), was taken as the representative displacement.

To quantify the uncertainty in mean velocity due to finite sample size, a 95% confidence interval was calculated based on the mean sample size N of 980 and root-mean-square (RMS) velocity magnitude $\sqrt{V'^2}$ of 78.2 m/s calculated over all cases examined:

$$\Delta_{|\bar{V}|} = \frac{1.96\sqrt{V'^2}}{\sqrt{N}} \quad (3.4)$$

The half-width $\Delta_{|\bar{V}|}$ of this confidence interval is approximately one-sixteenth the representative RMS velocity magnitude; planar measurements of RMS velocity for each test case will be presented in the next section. It is important to note that the mean sample size is slightly less than the total number of vector fields due to rejection of some vectors by the postprocessing algorithm. The uncertainties due to systematic error ϵ_{sys} and the confidence interval Δ were combined to determine the total uncertainty in mean velocity $\epsilon_{|\bar{V}|}$ according to Eq. (3.5):

$$\epsilon_{|\bar{V}|} = \sqrt{\epsilon_{sys}^2 + \Delta_{|\bar{V}|}^2} \quad (3.5)$$

The total experimental uncertainty of mean velocity was thus calculated as $\pm 2.7\%$, corresponding to ± 5.0 m/s when considering the representative value of 184 m/s. The uncertainty in an instantaneous measurement as calculated by the root-sum-square of all random error sources was found to be $\pm 0.85\%$, and was not included in the uncertainty of mean velocity since such random errors were captured along with true fluctuations as measured root-mean-square velocity. Statistical uncertainty of RMS velocity is strictly a function of sample size, and is given by:¹⁰⁷

$$\Delta_{\sqrt{V'^2}} = 1.96\sqrt{\frac{V'^2}{2N}} \quad (3.6)$$

The uncertainty of RMS velocity was found to be 4.4%, and as seen from Eq. (3.6) is a function only of sample size when expressed in this manner. Individual sources of uncertainty are summarized in Table 3.2.

3.3 Results

To examine potential disturbances to the flowfield resulting from the injection of seeded air through the slot injector, pressure data on the flowpath lower surface with and without tracer injection are presented in Fig. 3.3. Tunnel conditions differed somewhat from those at which PIV measurements were made, with total temperature and pressure of 592 K and 1.38 MPa, respectively. Since the

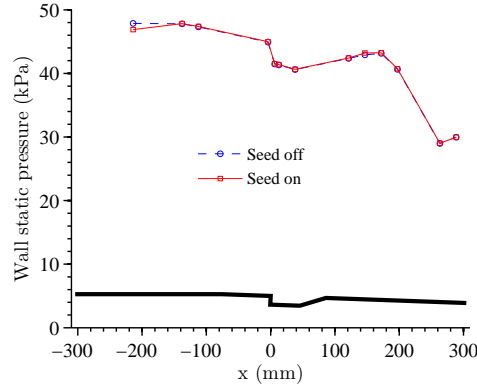


Figure 3.3: Static pressure on flowpath lower surface (geometry scaled to horizontal axis).

Mach number of the main-duct flow and the flow rate of seeded air were the same as those in the cases listed in Table 3.1, the results of this analysis are taken to be representative of the actual test conditions. Differences are seen to be minimal, with the maximum deviation of -2.0% (-0.94 kPa) occurring upstream of the slot injector. Pressure data in the immediate vicinity of the cavity indicate even smaller changes, suggesting that the particular region of interest of the flowfield was not appreciably affected by seeding, a conclusion confirmed by numerical analysis.¹⁰⁸

A total of 1069 vector fields were acquired for each of the cases listed in Table 3.1, corresponding to the maximum capacity of onboard camera memory for a single acquisition sequence. From these fields, mean velocity is quantified via its magnitude and path lines (Fig. 3.4), and unsteadiness is represented by RMS velocity (Fig. 3.5). Path lines were calculated through numerical integration of the velocity field, and are similar to but not identical to streamlines, which must satisfy the mathematical requirements of a stream function.

All data are presented over the same field of view, extending to 2 mm above the top of the cavity step and 7 mm upstream of the aft end of the cavity. This field of view was obtained as follows: first, for each individual test case all areas outside the uniformly-seeded cavity and shear layer were masked in the vector calculation process. Next, the presented measurement areas were made equal by plotting only those data within the above geometric limits. Additionally, data in a trapezoidal area adjacent to the cavity floor near $x = 25$ mm were excluded due to a reflection from an off-centerline spark plug igniter. This field of view represents the largest region that avoided all laser reflections and areas of poor tracer density in all eight test cases.

As an example of the data collected, the results of case 1a as presented in Figs. 3.4 and 3.5 will be examined. Considering mean velocity magnitude, it can be seen that large gradients exist within the flow, primarily in the y direction, which is to be expected in a cavity adjacent to a supersonic stream.^{39,100,109,110} It is also clear that the upper edge of the shear layer is outside of the field of view, since a region of nearly-uniform velocity is not seen, and instead a velocity gradient in the $+y$ direction extends to the upper edge of the measurement plane. These large velocity gradients result in a high dynamic range, with velocities measured from near 0 m/s to a maximum of 561 m/s. Considering RMS velocity, it is seen that the greatest unsteadiness occurs at the shear layer separation and reattachment points, located above the cavity step and the aft region of the ramp, respectively.

A comparison of shadowgraph results and path lines from PIV data (Figs. 3.1 and 3.4, respectively) is most relevant in consideration of shear layer behavior. Relative to the undistorted case, the intrusion of the shear layer into the cavity with the shock either on or upstream of the jet is clear, as is the shear layer deflection into the main duct with the shock on the cavity. No

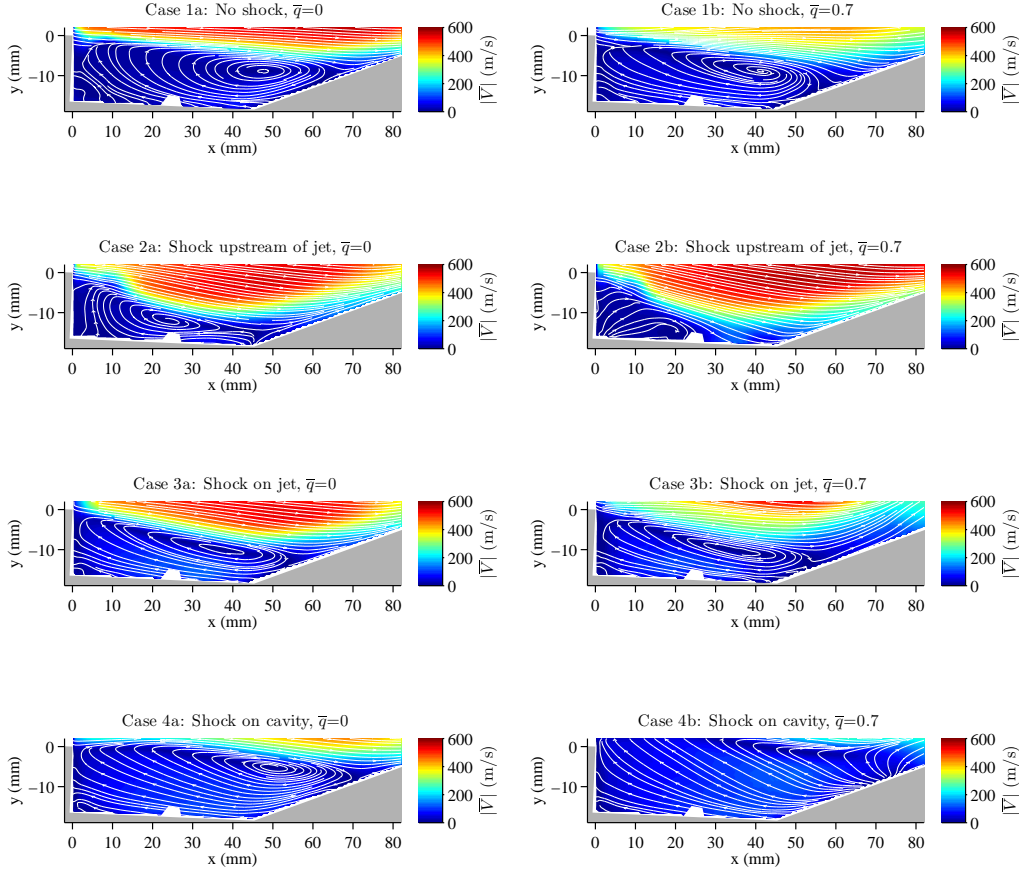


Figure 3.4: Mean velocity magnitude.

compressible flow features other than the shear layer can be quantified by the PIV data due to their limited field of view relative to shadowgraph results, but the latter show that the addition of upstream air injection yields insignificant changes to the location and nature of compression and expansion waves.

3.3.1 Jet $\bar{q} = 0$

To examine the influence on the cavity of shock impingement upstream of the jet, the results of case 2a are compared with those of case 1a. As seen in Fig. 3.4, the shear layer is deflected into the cavity downstream of $x = 12$ mm. The maximum velocity is nearly unchanged, 548 m/s instead of 561 m/s, but the velocity across the measurement plane as a whole is much higher, a result of shear layer intrusion into the cavity. A roughly-elliptical region of path lines within the cavity may be seen for both cases in Fig. 3.4, and careful inspection reveals that the path lines follow an outwardly-expanding spiraling path, suggesting the convergence of spanwise flow at the measurement plane. This pattern of recirculation has a distinct center, which moves 23 mm forward ($-x$ direction) and 3 mm downward between cases 1a and 2a, representative of the general displacement of the recirculation region as it is compressed by the intruding shear layer. This results in flow over the cavity ramp immediately exiting the cavity in case 2a, whereas part of such flow

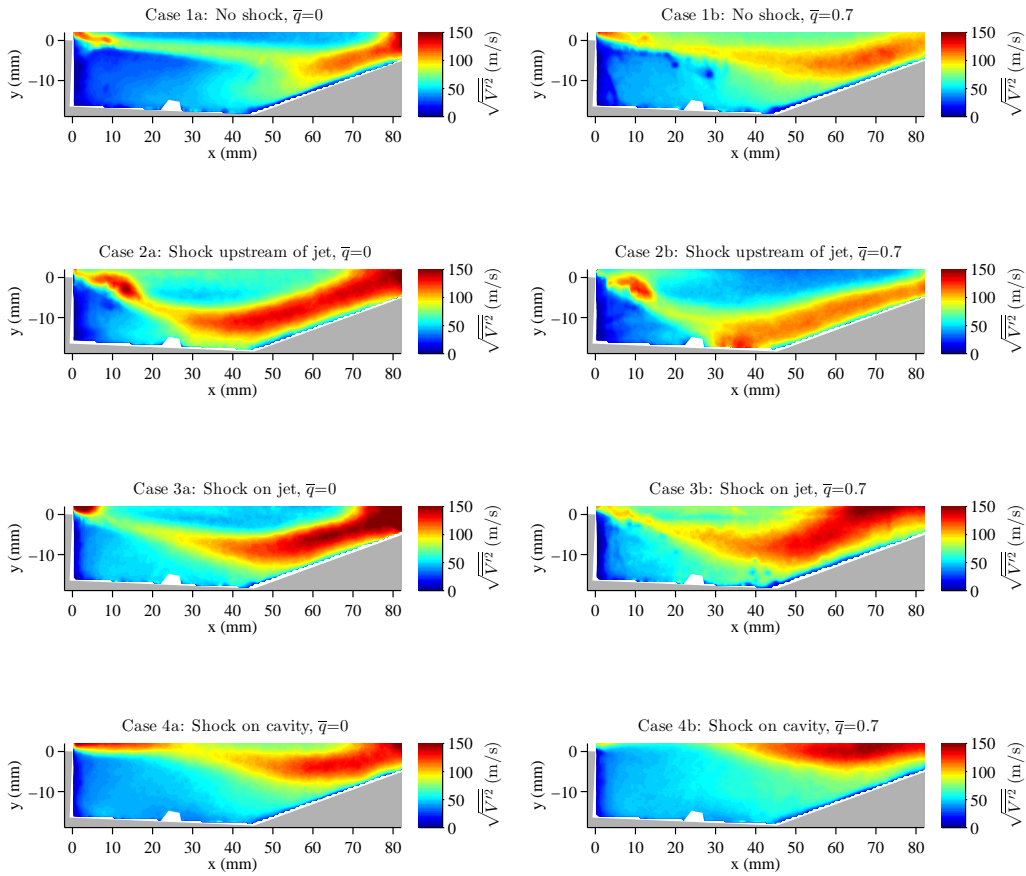


Figure 3.5: Root-mean-square velocity magnitude.

enters the recirculation region before exiting the cavity in case 1a.

Since most cavity flameholders with sloped aft walls (ramps) are designed such that shear layer reattachment occurs along this ramp, it is expected that not all flow over it will become entrained in the cavity. Instead, a stagnation point is formed along the ramp, dividing recirculating flow from that escaping the cavity, which for case 1a is located at $x = 62$ mm. The stagnation point moves to the lower edge of the ramp in case 2a, which may have implications for cavity fueling if flow patterns in the measurement plane represent those in the rest of the cavity. Fuel may be injected through ports in the ramp,³⁹ and in case 2a the data in Fig. 3.4 suggest most if not all of such fuel would be immediately convected into the main duct without entering the recirculation region, if the cavity flowfield is spanwise-uniform. In a prior investigation with this same flowpath and distortion configuration, combustion could not be initiated with fueling from the ramp face.¹⁰² Computational fluid dynamics (CFD) analysis of the same configuration suggested that a short residence time and low static pressures near the spark plug ignition sources may have been primarily responsible for the inability to achieve flameholding.¹⁰³

Flow with shock impingement on the jet injector (case 3a) also shows shear layer deflection similar to that in case 2a but to a lesser extent. The shear layer is also less curved than in case 2a, as seen in the corresponding plots of velocity magnitude. There is a 30 m/s reduction in maximum velocity for case 3a with respect to case 1a, but velocities in the measurement plane are overall much higher in case 3a. The center of recirculation is displaced 10 mm forward between cases 1a and 3a, a result of compression by shear layer deflection. This deflection also has the effect of making the crude ellipses of the path lines become much more elongated, in addition to moving the stagnation point forward to $x = 53$ mm.

The shock-on-cavity jet $\bar{q} = 0$ condition is represented by case 4a. Relative to case 1a, the shear layer shifts upward, thickens, and takes on an s-shaped form. The shear layer rises between the step and $x = 20$ mm, and descends toward the ramp downstream of this location. Although the thickness of the shear layer in this distortion configuration cannot be determined, since it appears to extend past the edges of the measurement plane, it is clearly much greater than in the undistorted baseline (case 1a). In contrast to the undistorted case, where the shear layer remains largely within the cavity, this distortion configuration moves the shear layer well into the main duct. As a result of this upward displacement of the shear layer, velocities are much lower across the measurement plane, with a 130 m/s reduction of maximum velocity relative to case 1a. Changes to the recirculation region relative to the undistorted case are minor, with its center displaced 3 and 4 mm in the $+x$ and $+y$ directions, respectively. The recirculation region expands both upward and aft ($+x$ direction) as a result of shear layer displacement, and the stagnation point moves aft to $x = 69$ mm.

Examination of RMS velocity in Fig. 3.5 shows that addition of the distortion generator produces much greater unsteadiness within the cavity, particularly along the ramp. This may be correlated with the shear layer impinging upon the ramp at steeper angles relative to the undistorted case, as seen in the path line plots of Fig. 3.4. Additionally, RMS velocities are higher both at the location of shear layer separation and through the remainder of the shear layer itself, indicating that the entire process of the shear layer separating at the cavity step, traversing the length of the cavity, and reattaching at the ramp is made more unsteady by the addition of flow distortion.

3.3.2 Jet $\bar{q} = 0.7$

Cases 1a and 1b represent the effects on an undistorted flowfield of jet $\bar{q} = 0$ and $\bar{q} = 0.7$ conditions, respectively. Jet injection thickens the shear layer, indicated by the smaller magnitude of the velocity gradient seen qualitatively in Fig. 3.4. As a result of shear layer thickening, the maximum velocity within the measurement plane is greatly reduced, 429 m/s as opposed to 561 m/s. The recirculation region is compressed by the thickening shear layer, with its center moving 7 mm in the $-x$ direction. Additionally, the ramp stagnation point moves toward the cavity floor to $x = 54$

mm.

A comparison of undistorted flow and flow with the shock upstream of the jet at $\bar{q} = 0.7$ conditions (cases 1b vs. 2b) reveals results similar to those at $\bar{q} = 0$ conditions (cases 1a vs. 2a). The resulting velocity magnitudes are similar, as can be seen in Fig. 3.4: the shear layer of case 2b is deflected into the cavity, increasing maximum velocity magnitude by 140 m/s relative to case 1b. The path lines in Fig. 3.4 show broad similarities between cases 2a and 2b, with the exception of a lack of an ordered recirculation region at the center plane in case 2b. There is little recirculating motion anywhere in this plane except for a small region of convergent flow near $x = 20$ mm, $y = -14$ mm. The stagnation point moves to the bottom of the cavity ramp, which would prevent fuel injected through the ramp from being entrained in the cavity, assuming behavior at the measurement plane is representative of the remainder of the cavity. Although the amount of fuel from the jet injector that may be entrained in the cavity was not quantified in this study, any such fuel will enter a much smaller recirculation region.

The changes brought to the undistorted $\bar{q} = 0.7$ (case 1b) flowfield by shock impingement on the jet injector (case 3b) are again similar to the corresponding changes at $\bar{q} = 0$ (case 1a vs. case 3a). The shear layer is deflected into the cavity, but to a lesser extent than with the shock impinging upstream of the jet, and the maximum velocity within the measurement plane increases by 100 m/s from case 1b to 3b. The path lines above the aft end of the cavity ramp are seen to diverge from its face, a phenomenon unique to this combination of distortion generator location and jet operation. Since examination of raw particle images qualitatively confirmed this behavior, this result is not considered to be a processing artifact but may be due to convergence of spanwise flow at the measurement plane. The recirculation region is compressed from the $+y$ direction by the deflected shear layer, and the center of recirculation moves 7 mm in the $-x$ direction with insignificant vertical displacement. The stagnation point is displaced forward along the ramp to $x = 51$ mm by the deflected shear layer, 3 mm forward of its location in the undistorted case.

Case 4b yielded the greatest changes relative to an undistorted baseline: with shock impingement on the cavity, the shear layer is nearly entirely removed from the cavity, with only its extreme lower edge seen at the top of the field of view and downstream of approximately $x = 50$ mm. The maximum velocity in the measurement plane is reduced by 200 m/s, with relatively weak velocity gradients throughout. Substantial changes are also seen in the path lines, with reverse ($-x$ direction) flow filling nearly the entire measurement plane. Though the limited field of view prevents its full characterization in the present study, numerical analysis indicated that this region does not support the kind of organized recirculation seen in the preceding cases.¹⁰²

It should again be noted that as with all cases examined, data were only acquired on the center plane, and may not be representative of the entire cavity volume. The potential for spanwise nonuniformity is particularly enhanced by operation of the jet injector, since it introduces a spanwise nonuniformity to the incoming flow. Spanwise flow in case 4b may be inferred from behavior near the stagnation point, located at $x = 73$ mm. Path lines that extend over much of the measurement plane originate at this location (see Fig. 3.4), again implying convergence at the measurement plane of spanwise flow that is subsequently directed away from the ramp. Spanwise flow patterns were found in earlier work in the same facility, where measurements of the OH radical using planar laser-induced fluorescence indicated a spanwise-asymmetric combustion product distribution despite a spanwise-symmetric fuel injection configuration.¹¹¹ Spanwise flow patterns were also suggested by numerical analysis of this flowpath under distorted-flow conditions.¹⁰³ Attempts in previous work to sustain combustion at the shock-on-cavity condition were successful both with and without fueling through the jet injector in addition to the cavity ramp,¹⁰² so it is clear that this mode of cavity operation does not preclude stable combustion. CFD analysis indicated that this configuration results in relatively high pressures in the cavity, thus enhancing flameholding potential.¹⁰³

Addition of the jet to the undistorted flowfield results in a general increase of RMS velocity while reducing peak magnitudes, as seen in Fig. 3.5. Changes brought by the shock impinging on and upstream of the jet at $\bar{q} = 0.7$ are similar to those at $\bar{q} = 0$, with greater unsteadiness along

the cavity ramp, and smaller increases at the location of separation and through the remainder of the shear layer. Unique behavior in RMS velocity is displayed by case 4b, corresponding to the unique mean-flow results seen in Fig. 3.4. The location of shear layer separation is displaced well outside of the field of view, and as a result no local maximum in RMS velocity occurs adjacent to the cavity step. The region of flow seen to reverse its mean x-velocity in a vertical distance of only a few millimeters near $50 \text{ mm} < x < 80 \text{ mm}$ and $y = 0 \text{ mm}$ (Fig. 3.4) corresponds to high RMS velocity (Fig. 3.5), while the remainder of the cavity shows much smaller spatial variation in flow direction coupled with lower unsteadiness.

3.4 Conclusions

The effects of simulated inlet distortion on a scramjet cavity flameholder were investigated with particle image velocimetry (PIV), providing the first measurements of their kind. The measurement area covered a spanwise center plane capturing most of the cavity as well as part of the bounding shear layer. A full-span distortion-generating wedge was used to produce an oblique shock wave that impinged upon locations within and upstream of the cavity. Addition of the distortion generator brought significant changes to both the magnitude and direction of the velocity field in the measurement plane via deflection of the shear layer. The area of recirculation within the measurement plane increased when the distortion generator was positioned such that the resulting shock impinged upon the cavity, and decreased with shock positions farther upstream, all relative to the undistorted baseline. In cases where a pattern of ordered recirculation was established, its center was displaced in the same direction but with smaller magnitude in relation to changes in the axial location of the shock.

Simulation of fuel injection with a wall-normal air jet upstream of the cavity produced less-severe changes to the flowfield, with similar magnitudes but different directions of velocity observed. In all configurations of the distortion generator, the jet thickened the shear layer, and changes to flow patterns upon addition of the jet were most pronounced with shock impingement upstream of the jet injector and on the cavity. In no conditions examined did the shear layer reattach to the cavity floor, demonstrating that the cavity maintained an aerodynamically open geometry. Instead, shear layer reattachment occurred on the cavity ramp in all but one configuration, and presumably occurred downstream of the cavity in the exception. Shear layer reattachment behavior has implications for direct fueling of the cavity through the ramp, since the relative locations of the stagnation point and fuel injection determine the amount of such fuel that is recirculated within the cavity.

Unsteadiness was quantified with root-mean-square (RMS) velocity, and results showed that addition of the distortion generator increased unsteadiness over the measurement plane as a whole, and the shear layer in particular, all relative to the undistorted baseline cases. Increases in RMS velocity magnitude within the shear layer would be expected to enhance turbulent transport into the cavity of fuel injected upstream and of cavity combustion products into the main duct. Areas above the cavity ramp exhibited particularly large increases in unsteadiness due to distortion, and the addition of upstream jet injection resulted in lower peak RMS velocities but generally greater unsteadiness across the measurement plane.

Chapter 4

Graphite Tracers for Velocimetry

4.1 Introduction

Supersonic combustion ramjet (scramjet) design is driven by computational fluid dynamics (CFD) models, which must be validated against experimental databases.^{13,21,43} Due to its high-enthalpy flow and confined environment,⁹⁶ the scramjet flowpath is better suited to minimally-intrusive optical diagnostics than probe-based techniques such as pitot-static measurements or hot-wire anemometry, since the physical presence of a probe will often distort the flow to the point of rendering invalid the measurement of interest.¹¹² Optical diagnostics applied to scramjet flows have included planar laser-induced fluorescence (PLIF),¹⁸ coherent anti-Stokes Raman spectroscopy (CARS),¹¹³ tunable diode laser absorption spectroscopy (TDLAS),^{114,115} tunable diode laser absorption tomography (TDLAT),¹¹⁶ laser Doppler velocimetry (LDV),³⁵ hydroxyl-tagging velocimetry (HTV),¹⁰⁰ and particle image velocimetry (PIV).^{36,38–40,42,43,45,117}

Of the velocimetry techniques, both PIV and LDV are dependent on proper seeding of the flowfield with tracer particles.⁴⁷ These particles must be sufficiently large to scatter enough light to enable photographic detection, yet small enough to faithfully track the flow.¹¹⁸ An additional challenge arises when particles run adjacent to the window of a confined flow, since particles may deposit on the window and obscure imaging or illumination.^{39,42,44,45,71,81,119} The severity of this effect is dependent on the individual experiment, but is a particular challenge in the recirculating flow of a recessed cavity flameholder.^{39,42} Prior PIV studies of cavity flameholders have used titanium dioxide as a tracer material due to its reduced tendency to form agglomerated clusters and abrade windows relative to other materials having comparable reflectivity and melting temperature, such as oxides of aluminum, silicon, and zirconium.^{39,42,117} Despite this, gradual window fouling still occurred, and it is desirable to select a tracer material that does not adhere to facility windows.

The objective of this study is to identify a tracer particle that permits PIV measurements in a high-enthalpy environment without degradation of flowpath windows. This chapter begins with a summary of attempts at PIV measurements using conventional metal oxide tracer particles in the cavity flameholder of a scramjet combustor. Next, the selection process of a new tracer material is described, along with its experimental characterization. Theoretical models are introduced to quantify the behavior of the particles in the experimental facility and compared with standard measures of acceptable flow tracking.

This work presents the first application of a tracer material that demonstrates complete compatibility with combustor windows by allowing seeding of indefinite duration in both low- and high-enthalpy regimes, satisfying the second scientific objective of this dissertation. Additionally, this is the first reported application of graphite tracers in either a high-speed flow or within a reaction zone.

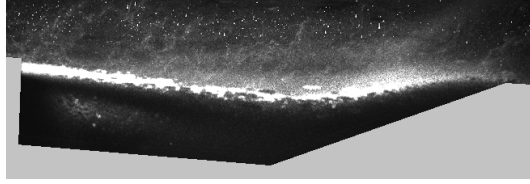


Figure 4.1: Raw PIV image of TiO_2 tracer particles after injection through port at $x/h=-14$. Areas outside measurement region are masked in gray for clarity.

4.2 Tracer Selection

4.2.1 PIV Configuration

PIV systems 2 and 3 were applied to the UVaSCF, in the same experimental configuration, to provide two-component measurements in the spanwise center plane of the cavity flameholder (see Sec. 2.2.2 for a complete description of each PIV system). The laser output was transformed into a sheet by a series of lenses and delivered to the test section through the narrow window in the wall opposite the cavity, terminating at the cavity floor. A single camera viewed the measurement plane orthogonally through a combustor side window, capturing the full spanwise center plane of the cavity as well as a section of the adjacent main duct, as depicted in Fig. 5.2. Prior to PIV measurements, a camera spatial calibration was performed by removing the flowpath window opposite the camera and inserting a calibration target into the test section such that it was coincident with the laser sheet. The flowpath window between the calibration target and the camera was left in place, thus maintaining the same optical path as during PIV acquisition.

Tracer particles were levitated by dry air in a fluidized bed seeder and injected on the centerline of the cavity-side combustor wall through a 3 mm-diameter port at an axial location of $x/h = -14$. This port had a circular cross-section but was angled at 25° relative to the flowpath surface, forming an elliptical exit profile. This configuration introduced a low-momentum jet of seeded air into the boundary layer at a small angle relative to the main-duct flow, minimizing perturbations to the flow while maximizing entrainment in the cavity. The design was also intended to minimize convective transport of tracer particles away from the measurement plane and toward the combustor sidewall windows, and was similar to that used in prior PIV studies in RC19, where window fouling was not substantial enough to preclude meaningful PIV results.^{39,40,42} Given that tracer injection in the present experiment occurred downstream of fuel injection, a solenoid valve was installed at the seeder inlet and opened only during tracer injection, to preclude the possibility of a combustible mixture traveling upstream to the pneumatic regulator at the operator's station.

4.2.2 Trials of Candidate Tracer Materials

Measurements were first attempted using 100 nm titanium dioxide tracer particles, of the same type as used in measurements presented in Chapter 3. The tendency for window fouling observed⁴² in RC19 was seen to be much more severe in the UVaSCF, with a large section of the window bounding the cavity becoming completely obscured within several seconds of the introduction of seeding at a density suitable for PIV measurements. A sample image from these attempted measurements, which used PIV system 2, is seen in Fig. 4.1. The outline of the cavity may be seen, but most of the window area bordering the cavity is rendered opaque by tracer particle deposition. Tracer density is generally good in the shear layer, with lower densities evident below it. Higher densities could be achieved, but this particular experiment was conducted with lower-than-ideal levels in order to minimize window fouling. However, due to the obscuring effects of tracer deposition no useful data

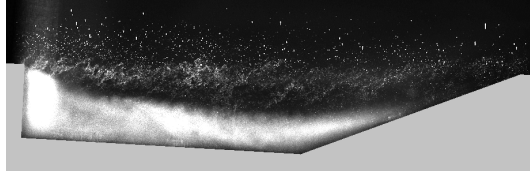


Figure 4.2: Raw PIV image of TiO_2 tracer particles after injection through port at $x/h=-1.0$. Areas outside measurement region are masked in gray for clarity.

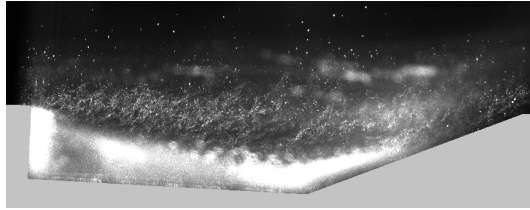


Figure 4.3: Raw PIV image of TiO_2 tracer particles after injection through port at $x/h=-1.0$, with vibration source active.

were ultimately obtained in the cavity interior.

Despite the fact that tracer particles were injected along the flowpath centerline, a large fraction of them migrated out to the side windows. This occurred in the UVaSCF at a much higher rate than in RC19, a result attributed to the lower width-to-depth ratio of the cavity of the former. It is anticipated that spanwise flow patterns will strengthen relative to those in the spanwise center plane as the cavity becomes narrower relative to its depth, resulting in greater distribution of particles away from the centerline and onto the side windows.

An attempt was made to minimize spanwise transport of tracer particles within the cavity by moving the injection location to a centerline wall-normal port of 1.0 mm diameter located at $x/h=-1.0$. This was intended to minimize the spanwise distribution of the tracer particles by reducing their distance traveled through the turbulent boundary layer upstream of the cavity. Results of this attempt are seen in Fig. 4.2. Although window fouling is noticeably reduced relative to seeding through the port at $x/h=-14$, a large section of the cavity was still obscured by tracer deposition. This indicates that spanwise flow patterns were strong enough to distribute tracer particles outward to the windows even when entering the cavity in a narrow region along the flowpath centerline.

This result motivated an attempt to minimize tracer adhesion to the windows by applying high-frequency vibration to the flowpath structure. To accomplish this, a pneumatic turbine vibration generator was attached to the frame of the window through which the camera viewed the measurement plane. This unit was rated by the manufacturer to produce vibration at 330 Hz with 50 N amplitude, and was selected on the basis of its high frequency and low amplitude relative to other available units. As seen in Fig. 4.3, window fouling was not appreciably affected by the addition of vibration. The mechanism of particle adhesion was not thoroughly investigated, but electrostatic charging of tracer particles relative to the windows was not considered a likely cause, since particles adhered to the electrically grounded copper cavity floor at levels qualitatively similar to those on the windows.

These results indicated that TiO_2 was not a suitable tracer material for this particular flowpath. An additional experiment was conducted using 250 nm SiO_2 particles injected through the port at $x/h=-14$, but results were similar to those using TiO_2 . This was not unexpected, as a prior PIV study in the UVaSCF using SiO_2 in a different experimental configuration found that seeded

flow running adjacent to facility windows resulting in unacceptable fouling.⁴¹ It should be noted that the raw images seen in Figs. 4.1, 4.2, and 4.3 were taken at different lens reproduction ratios and laser power levels, thus preventing a rigorous quantification of the obscuring effect of tracer adhesion. Such quantification is not necessary, however, since in all cases large sections of the cavity are thoroughly obscured.

Conventional PIV tracer particles able to withstand the high (2400 K maximum) temperature of the UVaSCF were shown to be transported to the side windows and could not be dislodged with the application of high-frequency vibration. A more aggressive means of particle removal was considered, such as air injection directed at the sections of the windows bordering the cavity. Even if successful, such a procedure would necessarily be so forceful as to alter the flowfield of interest beyond the point of utility, and the observed rate of window fouling was too great to permit occasional cleaning procedures between periods of data acquisition.

Since it was concluded that a portion of any tracer material introduced to the cavity would come in contact with the side windows, a search was made for a material that would either combust, sublime, or evaporate after resting on the windows for more than the few milliseconds needed for an airborne particle to contribute to a measurement. This strategy was applied by Love,¹²⁰ who exploited the tendency of solid CO_2 to sublime as a way to prevent tracer contamination of the windows of an unheated closed-circuit wind tunnel. CO_2 particles were formed by the sudden expansion of the liquid phase and persisted long enough to pass through the oblique shock of interest, but sublimated before they could reach facility windows.

Although CO_2 seeding is ideal for unheated facilities, the objective of the present study requires a material that will persist at least several milliseconds within the reacting cavity, but undergo its final physical or chemical transformation relatively soon after. This estimate of required persistence time was based on a calculation of cavity center plane residence time using the RC19 data of Kirik et al.⁴² It is important to note that particles need only survive one revolution through the recirculating flow pattern of the cavity in order to create uniform tracer density, which corresponds to a time-of-flight that is not necessarily equal to the cavity residence time.

In the search for a suitable tracer material, liquid droplets were discounted since they would almost certainly combust or evaporate too quickly. Solid particles were then examined, with the goal of selecting a material with an ignition temperature somewhat greater than the static temperature (670 K) but less than the total temperature (1200 K) of the non-reacting flow. Such a material would ideally experience negligible mass loss when traveling in the supersonic flow, but would combust after adhesion to facility windows due to the higher temperatures of the adjacent stagnated flow. An additional complication is presented by the desire to acquire PIV measurements at both non-reacting and reacting conditions. A particle that only combusts after settling on a flowpath surface under non-reacting conditions may well be consumed after only a very short period airborne in a reaction zone. The decision was made to select a tracer material based on the non-reacting temperature field, which is easily quantified analytically, and determine experimentally whether the particle behaves as desired in the reacting flowfield, since analysis of candidate materials with coupled CFD-chemical kinetics codes would be impractical.

A review of solid materials that could be practicably obtained in quantities suitable for PIV measurements revealed graphite as a candidate tracer. Its autoignition temperature of 1000 K is within the temperature range specified above,* and is readily obtained in a range of particle sizes from commercial vendors. The literature contains at least two PIV studies where graphite was selected as a tracer material instead of one of the more common metal oxides. Neubert et al.¹²¹ and Buschbeck et al.¹²² applied graphite tracers within the cylinder of a piston engine. In these studies, graphite was chosen to address the problem of scouring of transparent cylinder walls by particles collected by piston rings, which was substantially reduced by graphite's natural lubricity. This is a largely different problem than the central concern of the present study, since windows of the

*Material Safety Data Sheet, graphite powder, Fisher Scientific, Fair Lawn, NJ

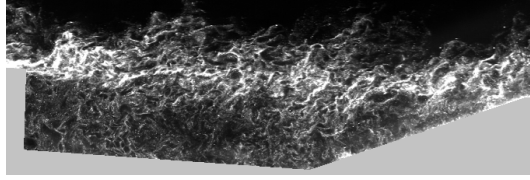


Figure 4.4: Raw PIV image of graphite tracer particles in UVaSCF under heated non-reacting conditions.

UVaSCF are not forcibly abraded by tracer particles. In fact, although metal oxide particles may render the windows opaque, they may be subsequently hand-cleaned to excellent optical quality.

One key difference of the in-cylinder studies relative to the present work is that the duration of a combustion stroke in a reciprocating engine is much longer than the mean flow-through time of a scramjet combustor. Because of this, the finding of Buschbeck et al.¹²² that graphite tracer particles were consumed by the combustion zone within piston-stroke time scales does not guarantee that reacting-flow measurements in the UVaSCF will be precluded.

Trials of several types of graphite powders were conducted, and ultimately synthetic flakes produced by Asbury Carbons were selected. PIV system 3 was used for this and all subsequent measurements, and sample raw images are given in Figs. 4.4, 4.5, and 4.6 for heated non-reacting, reacting, and cold-flow conditions, respectively. It is seen that flowpath windows are completely free of graphite tracer deposition, a result found to hold true for an indefinite duration of tracer injection, thus removing the restriction on optical access imposed by conventional metal oxide tracers.

The mechanism governing the tendency for a particular tracer material to adhere to flowpath windows was not identified, although a review of the available literature indicated susceptibility to electrostatic charging may be responsible. It has been found that many particle types will develop a negative charge upon becoming aerosolized,^{123,124} and in particular when subsequently passed through tubing,¹²⁵ as was done in these PIV experiments. Such particles may then experience electrostatic attraction to neutral surfaces by localized charging.¹²³

Since electrostatic charge is linearly proportional to the volumetric radius of a particle, whereas aerodynamic force varies in proportion to its square, it is seen that electrostatic attractive force will decay more gradually with particle size than will the aerodynamic force that may dislodge particles, which itself decays with particle size due to the presence of a boundary layer.^{123,124} As a result, the tendency for particles to adhere to surfaces will become greater as particle size decreases. The present study has not however yielded an explanation for why metal oxide tracers experience a strong affinity for flowpath windows whereas graphite tracers do not.

Figure 4.5 in comparison with Figs. 4.4 and 4.6 shows that the density of graphite tracers in the cavity is not appreciably affected by the robust reactions in this region. Figure 4.5 was taken at an equivalence ratio ϕ (the actual fuel-air ratio relative to that required to achieve stoichiometric fueling) of 0.40, and may be compared to PLIF imaging of the OH radical under identical conditions in Fig. 5.5(a). Particles are clearly seen in Fig. 4.5 both within and outside of the combustion zone, providing experimental confirmation that the graphite tracer particles persist long enough in the flame to permit PIV measurements.

Initial imaging of graphite tracers in the UVaSCF revealed a substantial disparity in reflected intensity between the two frames of an image, despite equal measured laser intensity of the respective pulses. It was determined that scattering was dependent on the polarization of incident light, since the two pulses of the laser in PIV system 3 have orthogonal polarization states. To resolve this, a half-wave plate was installed at the output of the laser and oriented such that the polarization of each laser pulse was rotated by 45° to achieve common alignment.

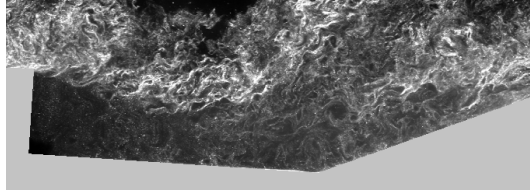


Figure 4.5: Raw PIV image of graphite tracer particles in UVaSCF under reacting conditions.

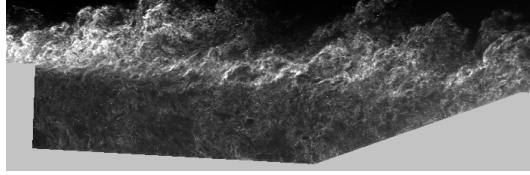


Figure 4.6: Raw PIV image of graphite tracer particles in UVaSCF under unheated conditions.

4.3 Tracer Characterization

4.3.1 Sampling

In order to analyze the aerodynamic and chemical response of the graphite tracer particles in the scramjet flowpath, it is necessary to quantify their size and shape. Although samples of the raw material could be analyzed, prior studies have shown that tracer particle agglomeration may occur during the fluidization process prior to injection.^{126,127} Ideally, particles would be sampled directly from the flowfield, but this is not practical given the high temperatures and velocities within the measurement plane. Instead, particles were sampled directly from the seeder output in a benchtop test. In order to replicate the conditions under which the seeder operated during PIV experiments, a nozzle was constructed with cross-sectional area identical to that of the port at $x/h=-14$, and the pressure differential across the seeder was matched, with dry air again used as the fluidizing gas.

Particle sampling should be done isokinetically, which requires that velocity at the sampling probe inlet be equal to that of the undisturbed flow, in order to ensure that the particle size distribution is not altered by streamline curvature near the probe inlet.¹²⁷ An isokinetic sampling rig was constructed following the methods of Owens et al.¹²⁶ This incorporated a hollow probe whose output led to a filter paper, with airflow maintained by a vacuum pump downstream. A rotameter was installed between the filter paper and the vacuum pump to enable flow velocity within the probe to be determined. The sampling probe tip was placed 8 mm downstream of the seeder nozzle exit, and the velocity at this location was measured with a hot-wire anemometer. The maximum velocity at any seeder operating condition was 40 m/s, ensuring that no compressible flow effects needed to be taken into account. The seeder output velocity was then matched at the sampling probe inlet by setting the probe volumetric flow rate to the appropriate value given its cross-sectional area. Tracer particle samples were then collected and stored on a mixed cellulose ester filter paper with $0.45 \mu\text{m}$ pore size, which was selected based on the $1.4 \mu\text{m}$ mean flake size found in earlier electron microscopy of the raw material.

4.3.2 Electron Microscopy

In order to quantify the size and shape of the graphite tracer particles as produced by the fluidized bed seeder, the particles captured in the isokinetic sampling test were analyzed by electron mi-

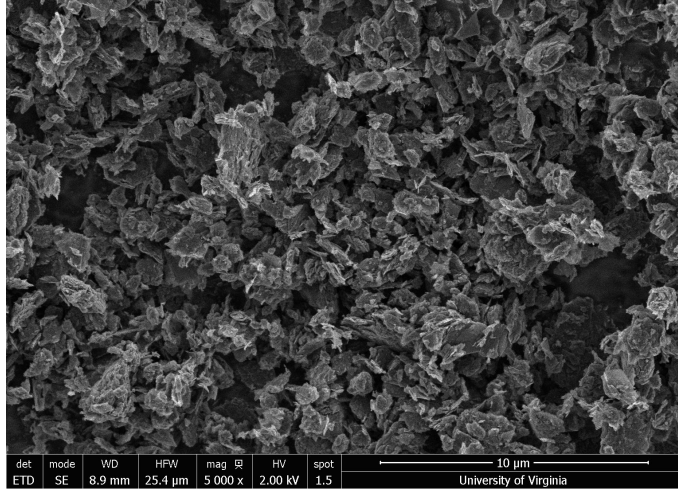


Figure 4.7: SEM image of graphite tracer particles at 5,000x magnification.

croscopy. An FEI Quanta FEG 650 scanning electron microscope (SEM) was used to image the collected particles at magnifications between 5,000x and 50,000x. An attempt was made to image the particles directly on the filter paper. This measurement could not be obtained, however, since the lack of a ground path between the particles and the electrically conductive base on which the filter paper was mounted resulted in the particles becoming charged and moved by the electron beam. Additionally, charging of both the particles and filter paper degraded image quality, and some SEM settings resulted in rapid deterioration of the filter paper. This required the particles to be transferred from the filter paper to an adhesive carbon tab. Although not ideal due to the disturbance this introduced to the particles, this proved the only practical means of achieving a measurement. A sample image is seen in Fig. 4.7.

Particles in the SEM images were subsequently measured using the ImageJ software package. A mean flake length of $1.1 \mu\text{m}$ was found, with values ranging between $0.20 \mu\text{m}$ and $3.5 \mu\text{m}$. A histogram of measured flake length is presented in Fig. 4.8. Particle length is seen to be concentrated near the mean value, with few particles having more than a factor of two difference with the mean. The mean thickness of individual flakes was found to be 16 nm from a range of $9\text{-}24 \text{ nm}$. Half-widths of 95% confidence intervals for flake length and thickness are respectively $0.12 \mu\text{m}$ and 2.4 nm . A histogram of thickness measurements is seen in Fig. 4.9, which shows a nearly-uniform distribution among the range of values. Additionally, an agglomerated cluster with thickness of approximately 100 nm was seen, but it was not clear whether this represented a grouping created during seeder operation, or was instead a product of the pressure applied during transfer from the filter paper to the carbon tab. This dimension will be considered in subsequent analysis for purposes of completeness, but is not included in the calculation of the mean due to its rarity and unclear origin.

These measurements are close to those found in a similar analysis of raw particles, where mean flake length of $1.4 \mu\text{m}$ and thickness of 13 nm were measured. It is unclear whether the differences may be attributed to random error, the operation of the fluidized bed seeder, or the transfer of particles from the filter paper to the adhesive carbon tab. It will be shown in the next section that the differences in mean dimensions of the raw particles and those sampled directly from the seeder result in negligible changes to aerodynamic properties. Due to the uncertainty of the effects on the particles their transfer from the filter paper to the adhesive carbon tab may have had, only the analysis of the raw particles will be considered in subsequent analysis.

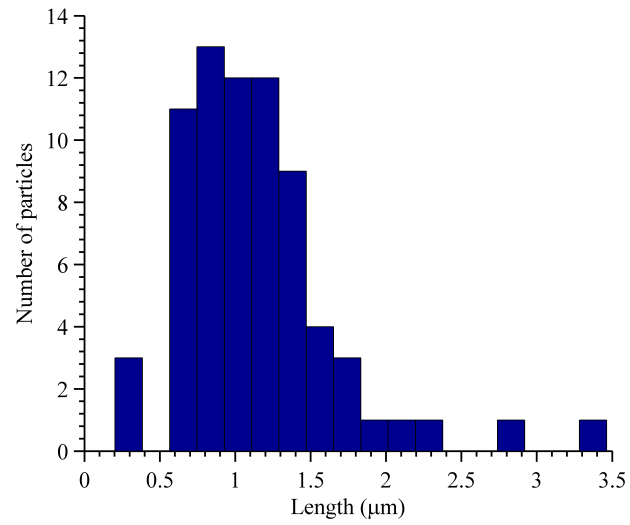


Figure 4.8: Histogram of measured flake length, taken from total sample size of 72.

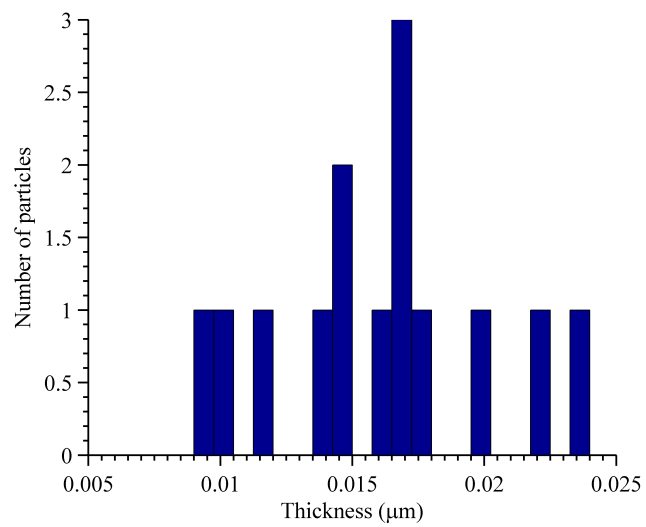


Figure 4.9: Histogram of measured flake thickness, taken from total sample size of 14.

4.3.3 Aerodynamic Response

Critical to the validity of PIV measurements is the requirement that tracer particles have negligible velocity relative to the flow in which they are distributed. Following the development of Loth,¹²⁸ this slip velocity is denoted \mathbf{w} and is the difference between the particle centroid velocity \mathbf{u}_p and the flow velocity extrapolated to the particle centroid \mathbf{u}_f

$$\mathbf{w} = \mathbf{u}_p - \mathbf{u}_f \quad (4.1)$$

This readily leads to the establishment of a particle Reynolds number (Re_p)

$$Re_p = \frac{\rho_f |\mathbf{w}| d_{vol}}{\mu} \quad (4.2)$$

where ρ_f and μ are respectively the density and dynamic viscosity of the fluid, and d_{vol} is the volumetric diameter of the particle,

$$d_{vol} = (6V_p/\pi)^{1/3} \quad (4.3)$$

where V_p is particle volume.

The assumption of negligible slip velocity is satisfied under the conditions of creeping flow, where particle Reynolds number approaches zero ($Re_p \rightarrow 0$). In this regime a closed-form solution for the drag of a sphere is available:

$$\mathbf{F}_D = -3\pi d_{vol} \mu \mathbf{w} \quad (4.4)$$

This is the Stokes drag solution, and provides a benchmark for evaluating the aerodynamics of non-spherical particles via the definition of a Stokes correction factor:

$$f = \frac{|\mathbf{F}_D|}{3\pi d_{vol} \mu |\mathbf{w}|} \quad (4.5)$$

A particle response time τ_p may be defined as the time taken to reduce an instantaneous imposition of a non-zero slip velocity to $1/e$ of its initial value.¹⁰⁴ Mathematically, for the case of a particle with density much greater than that of the surrounding fluid, it is expressed as

$$\tau_p = \frac{m_p |\mathbf{w}|}{|\mathbf{F}_D|} \quad (4.6)$$

where m_p is the particle mass.¹⁰⁴ Combining Eqs. 4.4 and 4.6 yields

$$\tau_p = \frac{m_p}{3\pi d_{vol} \mu f} \quad (4.7)$$

The graphite flakes used as tracer particles in the present study are approximated as oblate spheroids, characterized by the length of the axis of symmetry d_{\parallel} and its perpendicular dimension d_{\perp} . This allows the definition of an aspect ratio¹²⁸

$$E = \frac{d_{\parallel}}{d_{\perp}} \quad (4.8)$$

which for an oblate spheroid is less than unity. Volumetric diameter is given by

$$d_{vol} = d_{\perp} E^{1/3} = d_{\parallel} E^{-2/3} \quad (4.9)$$

The corresponding Stokes correction factor is a function of aspect ratio:¹²⁸

$$f_E = \frac{E^{-1/3} \sqrt{1 - E^2}}{\arccos E} \quad (4.10)$$

This model averages over all possible particle orientations relative to the oncoming flow, and is conservative in that oblate spheroids have been shown to preferentially assume the higher-drag broadside orientation.¹²⁸

As described in Sec. 3.2.2, the ability of tracer particles to faithfully track the flow may be quantified by the Stokes number, the ratio of particle response time to a characteristic domain time scale:¹⁰⁴

$$St = \frac{\tau_p}{\tau_D} \quad (3.1)$$

Samimy and Lele¹⁰⁵ recommend Stokes numbers less than 0.25 be established for valid velocimetry. Lower Stokes numbers yield more accurate flow tracking, thus a conservative estimate of the Stokes number will use the smallest representative domain time scale. Since tracer particle performance in the cavity flameholder is the primary consideration of this study, the domain time scale will be defined relative to the process of a particle traveling from the high-velocity main duct to the low-velocity region near the cavity floor. A representative time scale may then be calculated as the ratio of cavity depth l_D to main-duct velocity u_D :

$$\tau_D = \frac{l_D}{u_D} \quad (3.2)$$

The cavity depth is of course fixed over all experimental conditions, but main-duct velocity is not. Comparison of Eqs. 3.1 and 3.2 shows that Stokes number will increase with main-duct velocity. Therefore, a conservative estimate of Stokes number will use the maximum main-duct velocity that could be expected, which is calculated by considering the facility nozzle exit Mach number and total temperature under isentropic flow assumptions. The presence of shocks caused by wall-normal fuel injection and the heat release of combustion will only serve to decrease velocity adjacent to the cavity, resulting in an actual Stokes number smaller than this estimate.

An additional consideration is the possible reduction in flake dimensions due to oxidation. The dense seeding seen in Fig 4.5 indicates oxidation does not consume an appreciable fraction of particles during their residence within the cavity. Nonetheless, the degree to which they may shrink due to reactions is unknown, and the impact of this recession on aerodynamic performance must be considered. Proportional reductions in both length and thickness were modeled, such that a constant aspect ratio was maintained. Two flakes were considered, each with an initial length equal to the mean value of 1.4 μm . One flake was modeled as having an initial thickness equal to the mean value of 13 nm, and the other with an initial thickness of 100 nm corresponding to the observed agglomerated cluster. The results of this calculation are presented in Fig. 4.10.

It is seen that the ranges of Stokes numbers for both particles are well below the maximum value of 0.25 specified by Samimy and Lele.¹⁰⁵ It is also seen that Stokes number decreases with flake size (keeping in mind this model scales reduction in thickness linearly with reduction in length). As a result, a particle's flow tracking ability is only enhanced by its oxidation. The limit of particle performance is thus a function only of its light-scattering ability, which of course will fall below the threshold of detection at some minimum flake size. Figs. 4.4-4.6 demonstrate that the reflectivity and size of graphite tracers is sufficient to permit flow tracking across the majority of the measurement plane, with the remaining area unseeded only due to the limitations of turbulent diffusion in convecting tracers away from the cavity-side wall through which they were injected.

The chosen particle dimensions used in these calculations may be shown to be representative of the sample by considering the range of dimensions found. The thickness and length of a particular particle could not both be determined, since these measurements were dependent on the orientation of the particle relative to the SEM viewing angle, and no provisions were available for reorientation. However, consideration of combinations of initial dimensions other than those used in the preceding calculations reveals similar results to those seen in Fig. 4.10. With the exception of the agglomerated cluster, flake thicknesses were found to fall within a relatively narrow range, as demonstrated by the confidence interval given in Sec. 4.3.2. The preceding calculations were repeated for constant

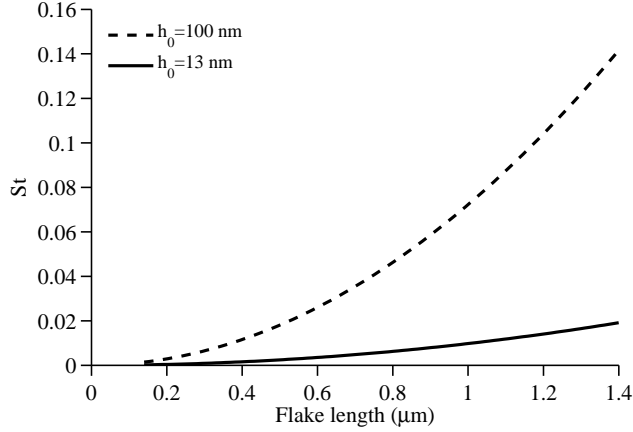


Figure 4.10: Stokes number as a function of flake length for two representative values of initial flake thickness h_0 .

flake thicknesses of 13 nm and 100 nm for a range of flake lengths, in order to investigate whether any combinations of length and thickness would yield unacceptable aerodynamic response.

As seen in Fig. 4.11, flakes with the mean thickness of 13 nm and any length up to the maximum measured value of $3.5 \mu\text{m}$ will satisfy the Stokes number criterion. Flakes with thickness of 100 nm will also satisfy this criterion provided their length does not exceed $2.8 \mu\text{m}$. It should be emphasized that a thickness of 100 nm was considered so as to include the agglomerated cluster observed in the SEM measurements. Since only one such cluster was observed, and its mechanism of formation is unclear, it is unlikely that such clusters form a substantial fraction of the tracer particles produced by the fluidized bed seeder. Even if this were the case, only a subset of such clusters would exceed the maximum Stokes number. The model applied is also conservative in that it assumes a cluster would consist of solid carbon, neglecting the voids between adjacent graphite sheets, thus reducing the cluster mass and improving its aerodynamic response. These results indicate that the overwhelming majority, if not the entirety, of the tracer particles will yield acceptable aerodynamic response in the UVaSCF.

An alternative to defining a single Stokes number for an entire flowfield is to consider particle response at each point in the flow. With knowledge of particle velocity and its gradient as well as a model of aerodynamic response, the in-plane components of slip velocity may be computed at all points in the measurement plane.¹²⁹ Using the particle equation of motion,

$$\frac{d\mathbf{u}_p}{dt} = \frac{\mathbf{F}_D}{m_p} \quad (4.11)$$

the slip velocity may be expressed in vector component form as

$$(u_p - u_f)_i = - \left(\frac{\rho_p d_{vol}^2}{18\mu f} \right) u_{p,i} \frac{du_{p,i}}{dx_i} \quad (4.12)$$

where ρ_p is the density of the tracer material, and summation across the repeated index i on the right-hand side is not implied.

In addition to the foregoing consideration of the response of a particle to a steady velocity gradient, the ability to track turbulent fluctuations must also be considered. Melling¹¹⁸ provides an expression for the maximum angular frequency of fluid motion ω_c that may be tracked at a given

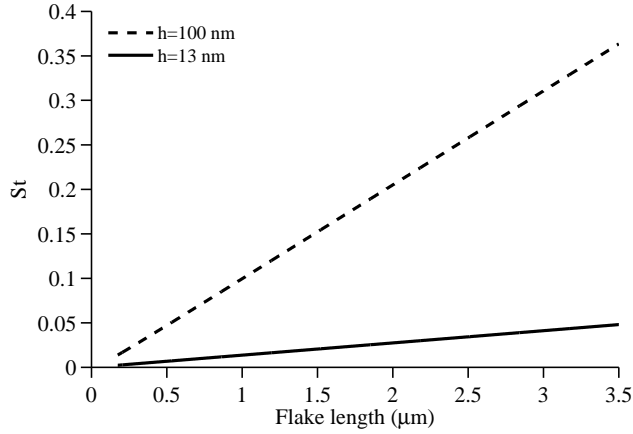


Figure 4.11: Stokes number as a function of flake length for two representative constant values of flake thickness h_0 .

ratio of particle and fluid mass-specific kinetic energies:

$$\omega_c = \frac{1}{\tau_p} \left(\frac{1}{\overline{u_p^2}/\overline{u_f^2}} - 1 \right) \quad (4.13)$$

In order to provide a conservative estimate of tracer performance, dynamic viscosity of air (as relevant to particle response time given in Eq. (4.7)) was calculated at the static temperature of the supersonic non-reacting flow; higher temperatures will serve only to increase viscosity and improve flow tracking. At Melling's recommended cutoff of $\overline{u_p^2}/\overline{u_f^2} = 0.95$, this calculation yields a maximum measurable angular frequency of 4.7×10^5 rad/s.

4.3.4 Thermophoretic Response

Thermophoresis serves to move tracers in the direction opposite that of a temperature gradient. Given that the measurement planes of experiments in the UVaSCF contain strong temperature gradients,⁵² it is reasonable to evaluate the effect thermophoresis may have on measured velocity. Thermophoretic velocity may be considered to be the product of a thermophoretic mobility and a temperature gradient:

$$u_{p,T} = M_{p,T} \nabla T \quad (4.14)$$

Keh and Ou¹³⁰ provide an expression for the components of thermophoretic mobility parallel and perpendicular, respectively, to the axis of symmetry of a spheroid:

$$M_{p,T,\parallel} = -\frac{C_s \mu}{\rho_f T} \left(1 + \frac{\alpha k_p}{\beta k_f} \right)^{-1} \quad (4.15)$$

$$M_{p,T,\perp} = -\frac{C_s \mu}{\rho_f T} \left(1 + \frac{\beta k_p}{(\alpha + 1) k_f} \right)^{-1} \quad (4.16)$$

where ρ_f is fluid density and C_s is a coefficient of order unity representing thermal slip at the particle surface. For this study, a conservatively high value of $C_s = 1.5$ was used. Shape constants α , β , and λ_0 are given by

$$\alpha = (\lambda_0^2 - 1) (\lambda_0 \coth^{-1} \lambda_0 - 1) \quad (4.17)$$

$$\beta = \lambda_0 [\lambda_0 - (\lambda_0^2 - 1) \coth^{-1} \lambda_0] \quad (4.18)$$

$$\lambda_0 = \sqrt{\frac{1}{1 - (1/E)^2}} \quad (4.19)$$

Since thermophoretic effects will not exert a torque on spheroidal particles,¹³⁰ the tracers may be considered to be randomly oriented and thus the group average given by Keh and Ou¹³⁰ may be used to calculate the magnitude of thermophoretic velocity:

$$u_{p,T} = -\frac{1}{3} (M_{p,T,\parallel} + 2M_{p,T,\perp}) \nabla T \quad (4.20)$$

Calculations of particle slip and thermophoretic velocity will be performed for experiments presented in Chapter 5, where it will be shown that the resulting contribution to experimental uncertainty is negligible relative to sources accounting for calibration error and finite sample size.

4.4 Conclusions

A process was implemented to identify a PIV tracer material that does not adhere to the windows of the combustor section of a direct-connect scramjet flowpath, removing a limitation imposed by conventional metal oxide particles. Micron-size graphite flakes were selected as a candidate material and subsequently tested at unheated, heated, and reacting-flow conditions in the UVaSCF. Raw PIV images showed no discernible tracer deposition on combustor windows even after long durations of flow seeding, and particles provided adequate light scattering to permit detection by the PIV system. Particles were shown to survive passage through the reaction zone of a cavity combustor, demonstrating that the chemical lifetime of graphite tracers is longer than the local flow time scales. The dimensions of the graphite flakes were measured via electron microscopy and used to model aerodynamic response in a high-speed cavity, demonstrating flow tracking acceptable to within standard limits.

Chapter 5

Flameholder Center Plane: Dual-Mode

5.1 Introduction

Trapezoidal cavity flameholders have received substantial attention as a means to stabilize combustion in scramjet flowpaths, which are challenged by main-duct convective time scales that significantly exceed those of chemical induction of hydrocarbon fuels.^{16,17,131} Such cavities provide a high-residence time region where reactants may mix with combustion products and produce a source of heat and radical species to pilot reactions in the remainder of the combustor.¹⁸ Cavity flameholders are particularly well-suited to dual-mode scramjet (DMSJ) designs, which may operate with core flow that is either primarily supersonic or subsonic, greatly expanding the range of flight Mach numbers accessible to a scramjet-powered vehicle.^{85,96} The pre-combustion shock system that is characteristic of DMSJ operation results in considerable aerodynamic unsteadiness due to shock wave/boundary layer interactions upstream of the combustion zone, and if fuel injection is located within this shock system a feedback loop based on the interaction of unsteady fuel-air mixing and heat release may result.^{59,85,132} Instabilities resulting from interactions between mixing and combustion may occur under primarily supersonic (scram-mode) conditions as well, and are an inherent aspect of scramjet operation under non-premixed conditions.⁴

Time scales of fuel-air mixing may exceed those of chemical reactions, particularly when hydrocarbon fuels are used, and as such heat release is in many cases limited by the degree to which reactants are mixed prior to reaching the flame front. In turn, heat release may govern local mixing via vorticity produced by the interaction of combustion-induced density gradients with strong pressure gradients resulting from high (even if subsonic) combustor Mach numbers, and changes to transport properties due to variations in temperature and chemical composition.^{4,77} Turbulence-chemistry interactions are thus masked by the intermediate step of fuel-air mixing, complicating efforts to isolate the direct relationship between heat release and combustor aerodynamics.⁸⁷ Since the operation of a cavity flameholder is dependent on the unsteady exchange of fluid across its interface with the remainder of the combustor, measurements of the local turbulent velocity field are essential to the characterization of flameholder performance, yet such measurements are inherently specific to a particular fuel injection configuration unless fuel-air mixing is completed well upstream of the flame front.

It is therefore desirable to study DMSJ operation independent of the fuel-air mixing process, and to address this need a premixed DMSJ flowpath has been developed and evaluated with a number of diagnostic methods.^{60,87,92,133–135} The University of Virginia Supersonic Combustion Facility (UVaSCF) was adapted to include fuel injectors upstream of the pre-combustion shock

system, such that passage through this shock system would ensure complete mixing of ethylene fuel and air prior to arrival at the reaction zone. Planar laser-induced fluorescence (PLIF) of the NO molecule confirmed uniformity of mixing by examining a fuel simulant injected under non-reacting yet aerodynamically-similar conditions to the baseline reacting case.⁹² Combustion behavior was examined through OH and CH₂O PLIF,^{60,133} CH* and broadband chemiluminescence,^{60,87} coherent anti-Stokes Raman spectroscopy (CARS),^{134,135} as well as numerical simulations.⁵²

These studies found that in a time-averaged sense, a nearly-linear flame front is established, anchoring a short distance downstream of the top of the cavity forward face, and extending to the opposite wall of the combustor at an angle of 10-12° relative to the duct central axis. It was determined that this angle is governed by freestream turbulence levels dictated by pre-combustion shock system aerodynamics, and not by fueling rate, inflow total temperature, or combustion-induced dilatation.¹³³ Instantaneous measurements revealed considerable variation in the spatial extent of the flame front,^{60,87,133} results that were consistent with but could not confirm numerical predictions of an instability caused by an interaction between combustor heat release and the upstream shock system.⁵²

To accompany these studies of combustion behavior, it is necessary to quantify the velocity field within the combustor, and the cavity flameholder in particular. Prior measurements of velocity in cavity-based high-speed combustors have both elucidated fundamental fluid physics as well as provided validation of numerical models critical to the development of airframe-integrated propulsion systems.^{37,43,136} The first reported planar velocity measurements within a high-speed cavity flameholder were made using hydroxyl-tagging velocimetry (HTV) in a non-reacting flowfield,^{100,137} and the subsequent application of particle image velocimetry (PIV) allowed a two-orders-of-magnitude increase in spatial resolution and the ability to examine reacting flows.^{39,42,45}

The present study seeks to quantify the mean and turbulent features of the flameholder velocity field, analysis of which has not been previously reported in the premixed or dual-mode combustion regimes. Of particular interest is the behavior of the turbulent shear layer separating the cavity from the combustor main duct, since flameholding requires unburned fuel and air remain in the cavity long enough to react yet be ejected back into the main duct at a rate sufficient to maintain its combustion. By examining this turbulent interaction as a function of independent changes in heat release and pre-combustion shock system length, the controlling parameters of flameholder aerodynamics may be identified.

This chapter addresses the third scientific objective of this dissertation, characterization of the cavity flameholder at steady-state dual-mode conditions. A description of the experimental facility and diagnostics is presented first, followed by an analysis of ensemble-averaged velocity statistics and their dependence on variations in heat release and pre-combustion shock system length. Finally, the combustor flameholding mechanism is evaluated through comparison of PIV and OH PLIF measurements.

5.2 Experimental Approach

5.2.1 Experimental Facility

The UVaSCF was used for the present research, in a configuration described in Sec. 2.1.2. Of particular importance to this study is the operation of the air throttle, which allows the pre-combustion pressure rise to be re-created through aerodynamic blockage instead of heat release. The behavior of this shock system will be characterized by the location in normalized coordinates of its leading edge, identified by a step change in streamwise pressure gradient. The nominally-inviscid supersonic core flow upstream of this shock system is presented with a decreasing cross-sectional area due to the growth of wall boundary layers, leading to a slight streamwise increase in static pressure, the magnitude of which is far smaller than that due to the shock system.

Case	ϕ	Shock system leading edge (x/h)	Air throttle status
1	0	27	off
2	0	-38	on
3	0	-45	on
4	0.40	-45	off
5	0.34	-38	off
6	0.34	-45	on

Table 5.1: Test conditions.

The test conditions listed in Table 5.1 were selected to examine the separate effects of pre-combustion pressure rise and heat release by independently varying air throttle pressure and equivalence ratio ϕ . Two equivalence ratios were considered, $\phi = 0.40$ and $\phi = 0.34$, which (when air throttle injection was not active) led to pre-combustion shock system leading edge locations of $x/h = -45$ and $x/h = -38$, respectively. These were previously found to represent (with a small amount of margin) the operability limits of the flowpath, with the lower equivalence ratio corresponding to the lean blowout limit and the higher representing the point beyond which the pre-combustion shock system would reach the fuel injectors, leading to greatly enhanced combustion and damage to the flowpath from the consequent increase in static pressure.⁸⁷ It should be noted that the upper limit of equivalence ratio in a flight vehicle would be determined by the point at which the pre-combustion shock system reached the inlet, leading to its unstating, assuming the flowpath was able to endure the aforementioned effects of the shock system reaching the fuel injectors.

Case 1 corresponds to the nominal fuel-off status of the flowpath, with a shock system established well downstream of the combustor serving to reconcile sub-atmospheric supersonic flow with the atmospheric facility exhaust. The air throttle is used in cases 2 and 3 to establish the shock system created by fuel-on cases 5 and 4, respectively. Case 6 uses the air throttle to maintain the longer shock system of case 4 but at a lower equivalence ratio. For all cases, tunnel stagnation conditions were maintained at constant $P_0 = 300$ kPa and $T_0 = 1200$ K, the latter approximating a Mach 5 flight enthalpy.

Static pressure was measured along the centerline of the cavity-side flowpath wall at 74 discrete locations distributed between the exit of the facility nozzle and the flowpath exhaust, and results for each test case are presented in Fig. 5.1 as normalized by absolute static pressure at the facility nozzle exit (38 kPa). It is seen that pressures upstream of the leading edge of the cavity flameholder ($x/h = 0$) were nearly identical among cases 3, 4, and 6, and similarly between cases 2 and 5, indicating that the pre-combustion shock system may be replicated independent of the amount of heat release. The pressure rise downstream of $x/h = 28$ in case 1 is due to backpressuring by the atmospheric facility exhaust and is distinct from the shock system upstream of the cavity in the remaining cases, for which the same pressure rise does not begin until approximately $x/h = 44$.

5.2.2 Particle Image Velocimetry

PIV system 3 was used for the present work, and is described in more detail in Sec. 2.2.2. Graphite tracer particles were aerosolized in a fluidized bed seeder with dry air at a volumetric flow rate between 13-15 standard cubic feet per hour (SCFH) and injected along the centerline of the cavity-side flowpath wall at $x/h = -14$ (see Sec. 4.2.1). Illumination of tracer particles was accomplished with a Photonics Industries DM50-527DH dual-head Nd:YLF laser operating at 527 nm, the output of which passed through a set of integrated optics to produce a 0.3 mm-thick sheet that was directed through the combustor window opposite the cavity flameholder.

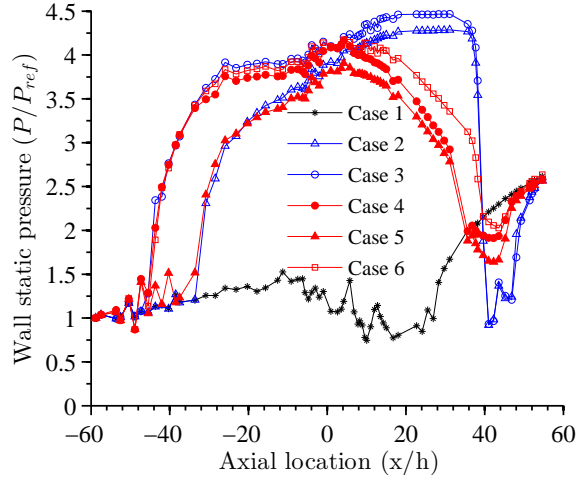


Figure 5.1: Cavity-side axial centerline static pressure distributions.

Images were acquired by a Photron SA 1.1 camera fitted with a 105 mm focal length Nikon lens, operated at an aperture of $f/8$. It was found that broadband chemiluminescence was much stronger than laser light scattered from the tracers, and as a result a line filter was fitted to the lens to block all wavelengths differing by more than a few nanometers from that of the laser. The camera viewed the measurement plane orthogonally, and a baffle consisting of a sheet of metal painted flat black was installed on the side of the combustor opposite the camera, in order to reduce the amount of stray light competing with particle scattering.

Synchronization of the laser and camera was provided by a LaVision high-speed controller, and vector fields were calculated with the LaVision DaVis 8.3 software package. All ensemble data sets consisted of 2000 singly-exposed dual-frame images acquired at a rate of 1 kHz, with a $1 \mu\text{s}$ separation between laser pulses. A schematic of the experimental configuration is included in Fig. 5.2.

Due to the nature of turbulent transport of tracers from the upstream boundary layer into the cavity flameholder, some regions of the measurement plane occasionally lacked tracer density sufficient to permit the calculation of a valid vector. Since the PIV algorithm may nonetheless generate a vector from background noise, it was necessary to exclude such regions from the vector calculation process. An image processing routine was applied to raw PIV images to eliminate areas of poor tracer density, and consisted of a standard deviation filter applied over a 4×4 pixel kernel, followed by a 6×6 pixel sliding average. Pixel locations for which the result of this calculation did not exceed a particular intensity count threshold were eliminated from subsequent vector calculation. The threshold value, which was the same for all cases considered, was selected based on manual inspection of the preprocessing routine's effect on a number of raw images, and would be expected to vary according to laser power and delivery method, signal-to-noise ratio, lens aperture setting, and image sensor response.

Additionally, pixels whose intensity saturated the dynamic range of the camera (12 bit), such as would result from laser scattering from a particularly dense region of tracers, were masked. This preprocessing routine was a binary operation and did not alter parts of the image that were not altogether eliminated. The fundamentally different aerodynamic nature of case 1 relative to the others limited the vertical extent of tracer distribution, and as a result data for case 1 will only be presented below $y/h = 0.55$; data for the remainder of the cases will be given for $y/h = 1.1$ and

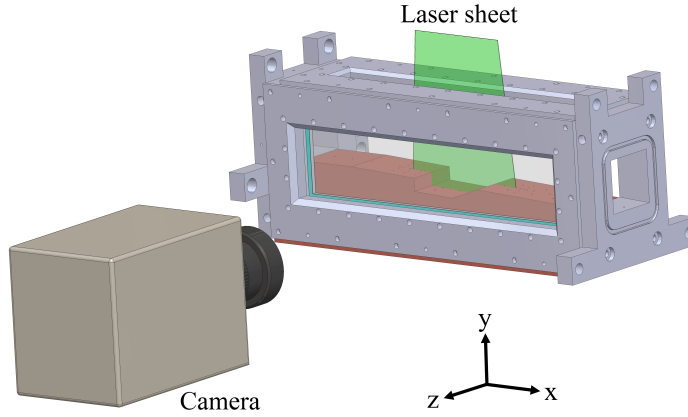


Figure 5.2: Schematic of camera and laser delivery configuration relative to combustor section.

below.

Vector fields for cases 2-6 were calculated by cross-correlation over round Gaussian-weighted interrogation windows, with three passes at a 32-pixel diameter followed by three at a 16-pixel diameter, each with 50% overlap of adjacent windows. A median filter was applied after each pass to reject spurious vectors,¹³⁸ and after the final pass vectors differing from the mean by more than three standard deviations were discarded. This procedure yielded a rectangular grid of vectors with 0.51 mm spacing in both the x and y directions, but due to window overlap spatial resolution is twice this value. The same procedure was applied to case 1 with the exception of the use of an initial interrogation window diameter of 64 pixels in order to accommodate the higher particle displacements of the supersonic main-duct flow.

The influence of tracer injection on flowpath operation may be assessed through an examination of wall pressure data. Figure 5.3 provides a comparison of pressures recorded at the conditions of case 4 with and without tracer injection. Seeding of the flow with graphite velocimetry tracers is seen to have a negligible impact on wall static pressures, confirming the non-intrusive nature of the diagnostic.

The uncertainty of ensemble statistics derived from a series of instantaneous PIV realizations is expected to result from a combination of systematic and random error sources. Uncertainty of mean velocity is a function of the systematic errors and the total measured fluctuations, the latter of which capture both true flow unsteadiness as well as random errors of the measurement technique.¹³⁹ Turbulent fluctuations may be assumed to be normally distributed for sample sizes exceeding 1000, thus allowing the normal distribution to be used to quantify the component of uncertainty resulting from finite sample size.¹⁰⁷ Using the same assumption of normality for random errors of the measurement technique, uncertainty of mean velocity $\epsilon_{|\bar{V}|}$ may be calculated as the root-sum-square of the contributions of systematic and random errors, with the latter calculated at a 95% confidence interval,

$$\epsilon_{|\bar{V}|} = \sqrt{\sum_i \epsilon_{sys,i}^2 + \frac{\left(1.96 \sqrt{V'^2}\right)^2}{N}} \quad (5.1)$$

where $\epsilon_{sys,i}$ are individual sources of systematic error, $\sqrt{V'^2}$ is the root-mean-square of fluctuations in velocity magnitude, and N is sample size. The number of individual vectors contributing to an ensemble statistic at a given location in the measurement plane was usually slightly less than 2000,

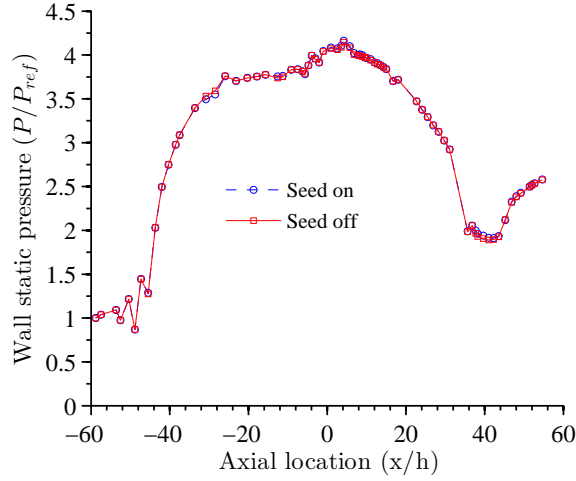


Figure 5.3: Cavity-side axial centerline static pressure distributions with and without graphite tracer injection, for $\phi = 0.40$, shock system $x/h = -45$ (case 4).

the number of image pairs, since the median filters used in vector calculation rejected some vectors, and near the upper limit of the measurement region tracer density was in some images not sufficient to permit a valid measurement, leading to exclusion by the algorithmic mask employed.

Four sources of systematic uncertainty were identified for the measurement configuration of this study. First, the grid fit by the PIV software to the image of the calibration dot card used to define a spatial scale contained a small residual between the imaged location of the dots and the vertices of the fitted grid. This error source, expressed as a root-mean-square calculated over all dot-vertex pairings, captured the combined effects of physical nonuniformity of the dot card, optical distortions induced by flowpath windows and lens aberrations, and errors in the calibration routine. Since this error source is expected to be proportional to the dot spacing of a particular dot card, the root-mean-square of the dot-vertex residuals was normalized by dot spacing and the resulting fraction was multiplied by mean velocity magnitude at each location in the measurement plane. A second source of systematic uncertainty considered was that of the scaling factor of the dot card, specified by the manufacturer as 0.070%, and was similarly applied to the mean velocity magnitude.

The final two uncertainty sources considered were aerodynamic and thermophoretic slip, discussed in Secs. 4.3.3 and 4.3.4, respectively. Since measurements of temperature, density, and viscosity in the measurement plane of this study were not available, the numerical simulations of Ramesh et al.⁵² were used instead. These errors may be considered systematic in the sense of uncertainty of mean velocity since there is a preferential orientation of their motivating phenomena, the mean velocity field and flame front location, respectively.

Perspective error resulting from movement perpendicular to the laser sheet of particles located away from the camera lens central axis was discounted as a systematic error source, since a preferential direction of spanwise velocity is not expected in the spanwise center plane, a result qualitatively confirmed in the experiments discussed in Chapter 6. The resulting random error due to fluctuations in spanwise velocity will be incorporated with all others in the measured fluctuations.

Eq. (5.1) was applied to each point in the measurement plane using the uncertainty sources described, and the result for case 4 is given in Fig. 5.4. It is seen that uncertainty is highest at the location where the shear layer reattaches to the cavity aft face, which is marked by strong fluctuations in velocity, as will be shown in subsequent figures. Across the measurement plane,

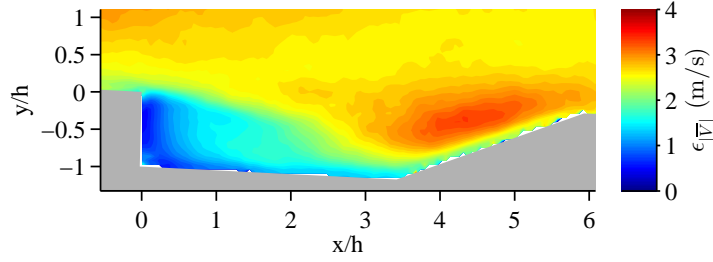


Figure 5.4: Uncertainty of mean velocity for $\phi = 0.40$, shock system $x/h = -45$ (case 4).

uncertainties due to the combined effects of calibration residuals, dot card scaling error, and finite sample size exceed those of thermophoresis and aerodynamic slip by at least two and four orders of magnitude, respectively, indicating flow tracking errors of the graphite particles make a negligible contribution to overall experimental uncertainty. The average uncertainty as a percentage of mean velocity magnitude is 4.2%.

The fractional uncertainty of the variance of velocity is a function only of sample size, and at a 95% confidence interval is given by the following:¹⁰⁷

$$\frac{\epsilon_{\overline{V'^2}}}{\overline{V'^2}} = 1.96\sqrt{\frac{2}{N}} \quad (5.2)$$

Based on the average sample size of 1818, the fractional uncertainty of variance of velocity as averaged across the measurement plane is 6.5%.

5.3 Results

PLIF imaging of the OH radical will first be analyzed in order to characterize combustion behavior within the PIV measurement plane. In premixed hydrocarbon combustion, elevated concentrations of this intermediate species extend from the flame front into the region of high-temperature products, permitting identification of the reaction zone.¹⁴⁰ Measurements of Cantu et al.¹³³ are presented in Fig. 5.5, showing both mean and standard deviation of OH PLIF intensities as well as a single instantaneous image. It is important to consider that these measurements show only the relative variation of OH concentration and do not quantify its absolute magnitude, but for the purposes of this study only the former is needed to characterize the reaction zone. In order to image the region shown, it was necessary to combine the results, acquired separately, of two measurement locations with a mutual boundary at $x/h = 4.5$.

Mean OH PLIF intensity reveals a flame filling the aft region of the cavity and extending into the main duct at a shallow angle. Comparison with standard deviation as well as the instantaneous image implies an unsteady combustion process, whereby products within the cavity are convected out into the main duct, where they may initiate further reactions. Since the incoming flow has been shown to be well-premixed,⁹² and a cavity flameholder will entrain only a small amount of the total combustor flow,¹⁶ these main-duct reactions lead to the majority of flowpath heat release. PIV results may be used to further characterize the flameholding process.

An instantaneous PIV measurement for case 4 is given in Fig. 5.6(a), providing path lines overlaid on contours of velocity magnitude. The irregular boundary of data above $y/h = 0.55$ is a result of variability of tracer density in the main duct, as discussed previously. The spatial variation of the contour levels implies a velocity field strongly influenced by turbulent structures, which are produced by the formation of the shear layer at the cavity leading edge and its subsequent impinge-

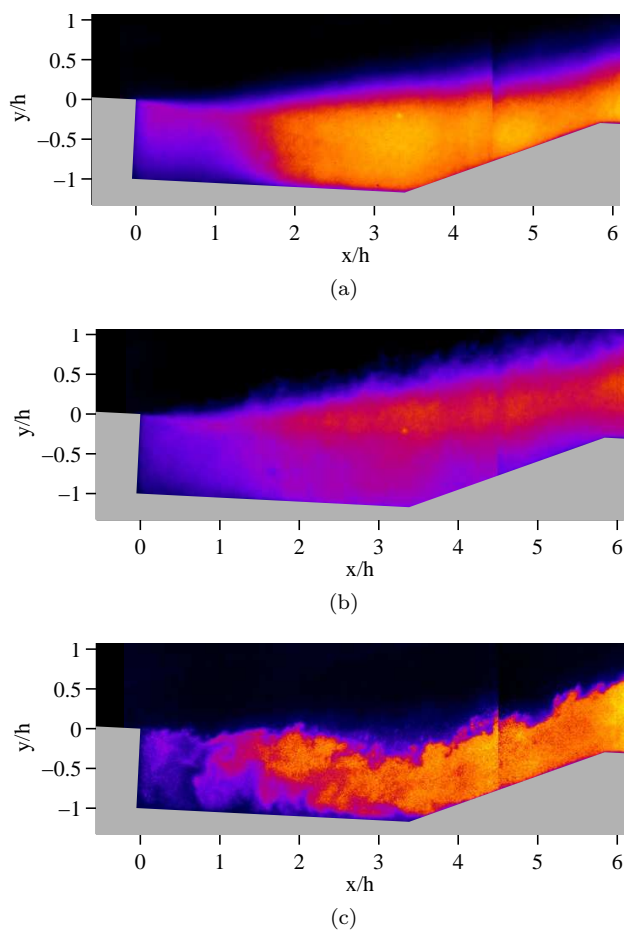


Figure 5.5: Composite mean (a), standard deviation (b), and instantaneous (c) OH PLIF intensity¹³³ for $\phi = 0.40$, shock system $x/h = -45$ (case 4).

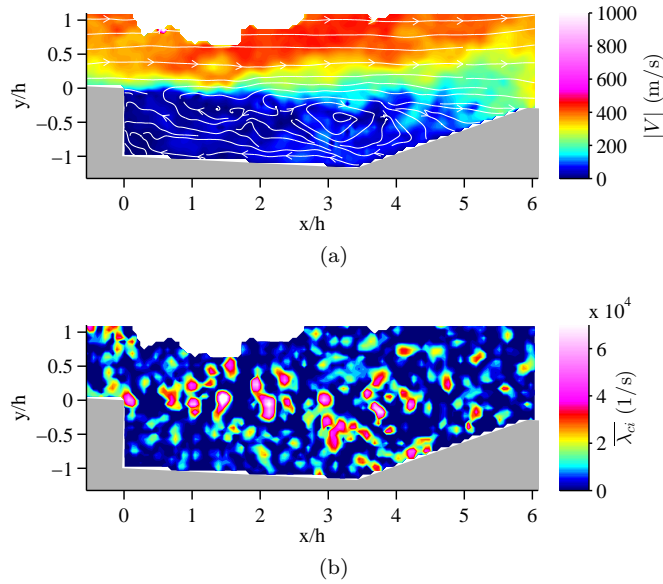


Figure 5.6: Instantaneous magnitudes of velocity (a) and swirling strength (b) for $\phi = 0.40$, shock system $x/h = -45$ (case 4).

ment on the aft face, as well as interactions between the upstream shock system and boundary layers.

Cavity flameholder operation is dependent on the continuous exchange of fluid with the main duct, a process that occurs via transport of turbulent fluid parcels. Such interaction is driven by both eddies in the shear layer as well as main-duct turbulence. Characterization of these eddies by their vorticity is challenged by the dependence of this calculation on the selected frame of reference in conjunction with the high dynamic range of velocity. Swirling strength $\overline{\lambda_{Ci}}$ is a better metric, since it is independent of reference frame and allows characterization of rotational flow by providing the inverse period of revolution of a fluid parcel about a vortex core, so long as the rotational axis is displaced less than approximately 60° from the measurement plane normal.¹⁴¹ Planar compressible shear layers have been shown to produce rotational structures with axes nearly perpendicular to the measurement plane of this study,¹⁴² making this technique ideal for investigating turbulent exchange of mass and momentum between the cavity and main duct.

Swirling strength of the instantaneous velocity field of Fig. 5.6(a) is given in Fig. 5.6(b). As expected of a cavity adjacent to a high-speed flow,³⁹ the highest values are concentrated in the shear layer, with smaller magnitudes in the lower-velocity cavity interior and less-turbulent main duct. It is seen that the curvature of contour levels of velocity magnitude corresponds with locations of high rotational intensity, indicating the velocity field of the cavity center plane is dominated by turbulent structures.

Referring to Fig. 5.6(a), two centers of cavity recirculation are observed: one at $x/h = 1.4$, $y/h = -0.33$ and the other at $x/h = 3.2$, $y/h = -0.44$. This pattern was seen, with some variation in location of the recirculation centers, in other instantaneous realizations as well. As will be seen in the following analysis of mean velocity, this behavior is however dominated by larger-scale recirculation established over the majority of the cavity center plane.

Contours of mean velocity magnitude with overlaid path lines are given in Fig. 5.7 for the six cases examined. Under all conditions the cavity maintains an aerodynamically open geometry, whereby the shear layer does not reattach to the cavity floor.¹⁶ Dynamic range of the flow is high,

with a nearly-uniform velocity profile in the axial direction above the cavity bordering a low-speed recirculation region within it.

Cavity recirculation is well-organized, with both the primary recirculation region that occupies most of the cavity as well as a small corner vortex resolved by the measurement technique. Returning to the two rotational regions seen in the instantaneous measurement of Fig. 5.6(a), it is seen that the magnitudes of velocity associated with them must be smaller than those of the larger recirculation pattern, since only the latter is evident in the ensemble average. Such behavior may be explained in a two-dimensional sense by potential flow theory, by which the interaction of two vortices of the same direction of rotation will revolve about a common center in the same direction as their individual rotation.¹⁴³ Comparison of Figs. 5.6(a) and 5.7 shows that the two rotational regions seen in the instantaneous measurement do indeed have the same clockwise rotation as the primary recirculation region of the ensemble average, and lie on either side of the center of the latter.

Referring to the ensemble averages of Fig. 5.7, it is seen the primary recirculation region takes a nearly-constant structure for all cases when a shock system is established upstream of the cavity (cases 2-6), but is expanded into the main duct relative to its state without a shock system (case 1). Examination of recirculating path lines reveals a tendency for outward expansion, a result that has been previously observed in a different facility.^{39,42,45} This suggests convergence at the measurement plane of spanwise flow, since compressibility is negligible at the low Mach numbers in this region.

The most significant factor affecting the distribution of mean velocity is the addition of an upstream shock system. As seen by comparison of cases 1 and 2, the shock system substantially reduces velocity above the cavity and thickens the shear layer, and its movement farther upstream (case 3 vs. 2) yields similar but smaller changes. Once the shock system is established and combustion has been initiated, changes to its position and the amount of heat release have comparatively minor effects, as seen in comparison of case 4 with cases 5 and 6.

The addition of heat release has a greater effect on mean velocity when the shock system takes the shorter (leading edge $x/h = -38$) of the two lengths studied. Comparison of cases 2 and 5 show a marked decrease in main-duct velocity magnitudes and a thickening of the shear layer, which may be attributed to a combination of increased dynamic viscosity and dilatation due to elevated temperatures as well as baroclinic torque.^{39,77} When the shock system leading edge is moved to $x/h = -45$, greater heat release results in much smaller changes, as seen in comparison of cases 3, 4, and 6, indicating the cavity mean velocity field is dominated by pre-combustion aerodynamics in this configuration.

It has been seen, for example by comparison of cases 2 and 5 of Fig. 5.7, that combustion may influence the velocity field upstream of the flame front. This may be explained by the fact that the flow throughout the measurement plane in cases 2-6 is subsonic, allowing aerodynamic disturbances to propagate freely in all directions, and that the flame front occupies, at least intermittently (Fig. 5.5), the majority of it. The extent of this influence on turbulent velocities will be examined as part of the subsequent discussion.

Contours of mean swirling strength are presented in Fig. 5.8, and represent the average of fields calculated for each of the 2000 instantaneous measurements per case. Several features common to all six cases are observed. Rotational intensities are highest at the shear layer separation point, and diminish in magnitude while broadening in the transverse direction with downstream distance, before reaching a region of elevated magnitudes at the shear layer reattachment point. The turbulent interaction of the shear layer with the cavity aft face is expected to lead to eddy formation, a result that has been previously observed in a cavity flameholder adjacent to supersonic main-duct flow.³⁹ A key difference relative to the supersonic regime is seen in cases 2-6, both in comparison to case 1 as well as the results of Tuttle et al.:³⁹ peak swirling strength is confined to a narrow band within the shear layer when main-duct flow is supersonic, whereas peak magnitudes are more broadly distributed in the subsonic cases. Swirling strength is nearly uniform in the main duct and forward region of the cavity for each case, with the exception of a strong corner vortex for the supersonic

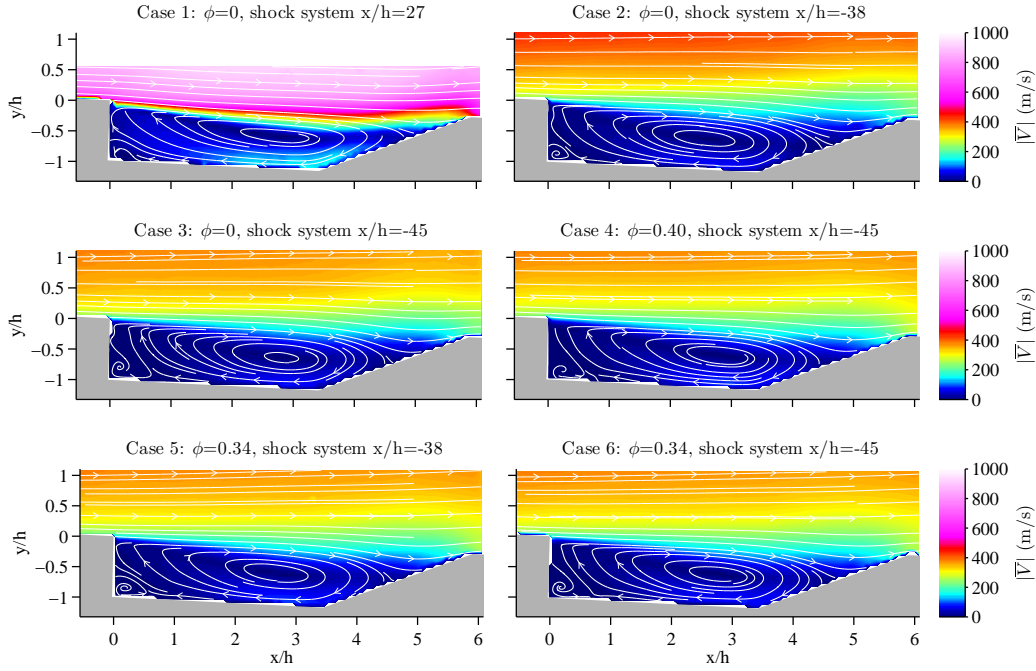


Figure 5.7: Mean velocity magnitude.

case.

The upstream shock system is seen to reduce swirling strength across the measurement plane. Under adiabatic conditions, the main duct is most affected by the movement of the shock system leading edge from $x/h = -38$ to $x/h = -45$, whereas behavior of the shear layer and cavity interior is primarily a function of whether the upstream shock system is present and only marginally influenced by its location. Heat release serves to further reduce rotational intensities, with the most-pronounced change occurring for the $x/h = -38$ shock system location. Adding or increasing heat release for the $x/h = -45$ cases causes a smaller but consistent decrease in swirling strength, an effect that is more pronounced in the shear layer than the main duct. Swirling strength within the shear layer shows a very slight increase with upstream movement of the shock system at constant heat release (cases 5 and 6).

Evaluation of swirling strength also permits insight into the performance of the graphite tracers in tracking flow fluctuations. It was found in Sec. 4.3.3 that the maximum angular frequency that may be adequately resolved is 4.7×10^5 rad/s. Upon comparison with Fig. 5.8, it is seen that the highest rotational intensities are approximately an order of magnitude lower, indicating that measured swirling strength represents true flow behavior and not an upper limit of the measurement system.

In a time-averaged sense, continuity requires zero net mass exchange between the cavity and the remainder of the combustor, and as such it is the fluctuating velocities that provide insight into the means by which the flameholder may entrain reactants and return their products to the main duct. Variance of velocity in both the axial (x) and transverse (y) directions, as well as the correlation between the two, will be used to characterize this process, and is presented in Figs. 5.9-5.11. The rectangular region of absent axial velocity variance data near $x/h = 2.5$, $y/h = -1$ for case 1 (Fig. 5.9) corresponds to a laser reflection that induced spurious axial components of velocity and was thus masked, but whose effect was not evident in the remainder of the presented statistics.

All three quantities display similar trends of distribution of relative magnitudes among the

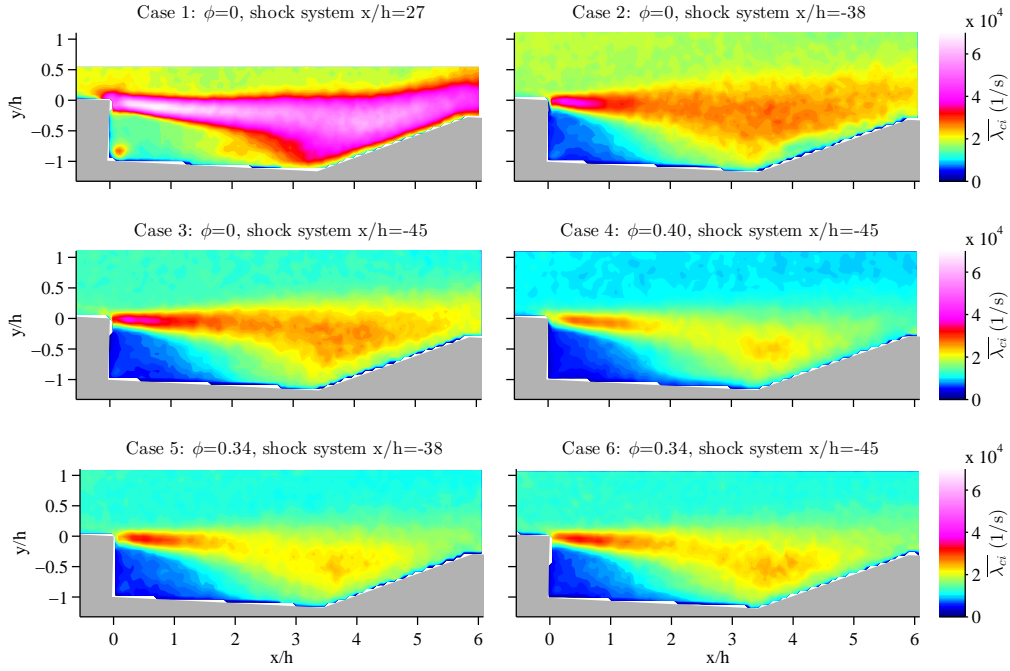


Figure 5.8: Mean swirling strength.

six cases, indicating turbulent anisotropy is not substantially affected by changes in shock system configuration or heat release. Across all cases examined, magnitudes are highest in the shear layer, with maximum values occurring at the reattachment point on the cavity aft face. Similar to the result seen with swirling strength, peak variances under the dual-mode conditions of the present study are much more broadly distributed than in the supersonic cases reported here and by Tuttle et al.³⁹ The smallest magnitudes occur in the boundary layer immediately upstream of the cavity and in the low-speed regions of the cavity interior, the latter of which is in accordance with prior HTV¹⁰⁰ and PIV³⁹ measurements of the supersonic mode.

Addition of the upstream shock system reduces fluctuations in the shear layer and below while increasing them above (case 2 vs. 1), and movement to $x/h = -45$ (case 3) reduces magnitudes throughout the measurement plane. As with swirling strength, upstream movement of the shock system at constant fueling rate of $\phi = 0.34$ results in a very slight increase in magnitudes within the shear layer. The addition of or increase in the rate of heat release at a fixed shock system location is seen to consistently decrease fluctuations in the shear layer and cavity interior, in accordance with prior measurements of the non-premixed supersonic mode.³⁹ In particular, the reduction in spatial extent of the region of elevated axial velocity variance (Fig. 5.9) demonstrates that the range of motion of the shear layer reattachment point at the cavity aft face is reduced by heat release.

The effect of heat release on the main duct is not as simple: when examining the cases with the leading edge of the shock system located at $x/h = -45$, the addition of heat release increases fluctuations (case 6 vs. 3), but greater fueling (case 4) returns them to levels comparable to those in the fuel-off case. In contrast, fluctuations in the main duct are substantially reduced by the addition of heat release when the shock system is fixed at $x/h = -38$ (case 5 vs. 2).

Figure 5.11 shows that the orthogonal components of fluctuating velocity demonstrate negative correlation over nearly the entire measurement plane, with the exception of regions immediately adjacent to the cavity floor and aft face, locations whose low velocities present the greatest challenge to the PIV technique. Tuttle et al.³⁹ reported similar results in an investigation of a supersonic

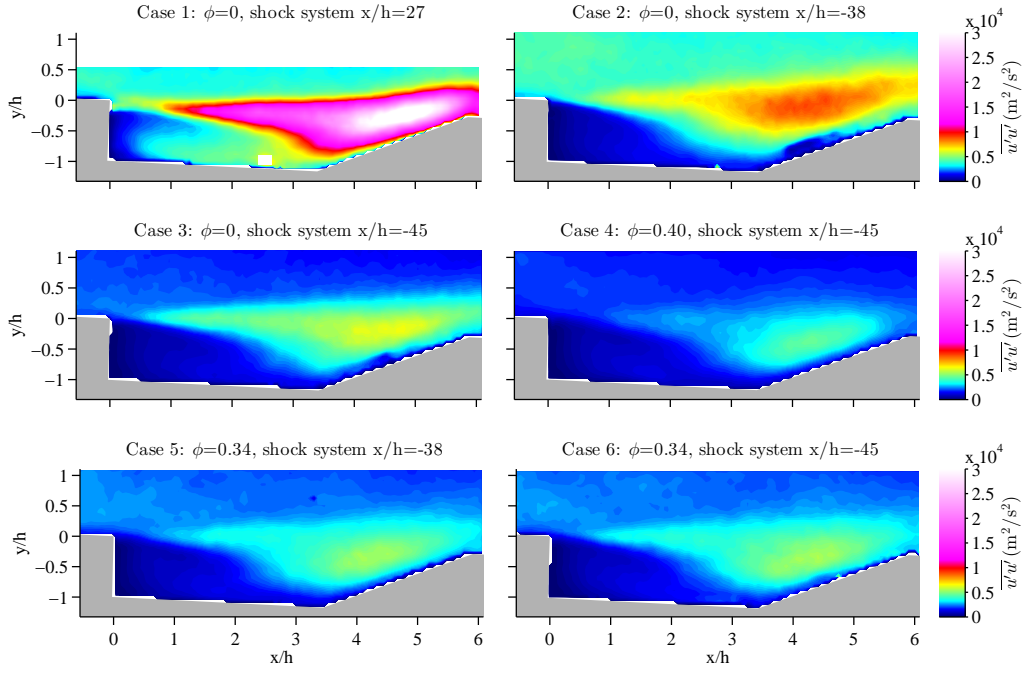


Figure 5.9: Variance of axial velocity.

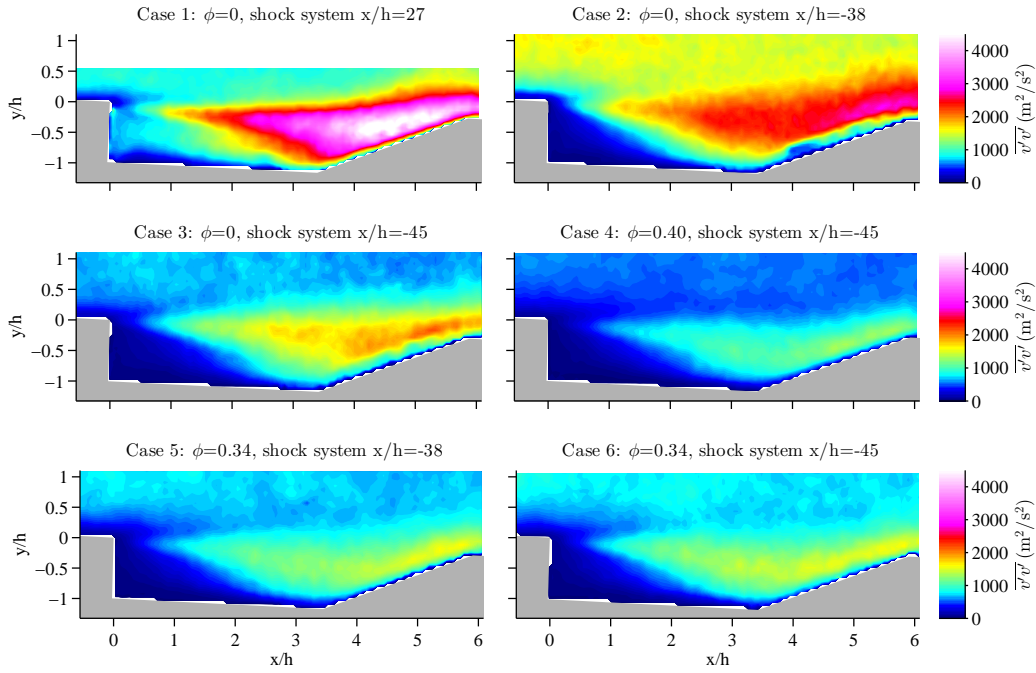
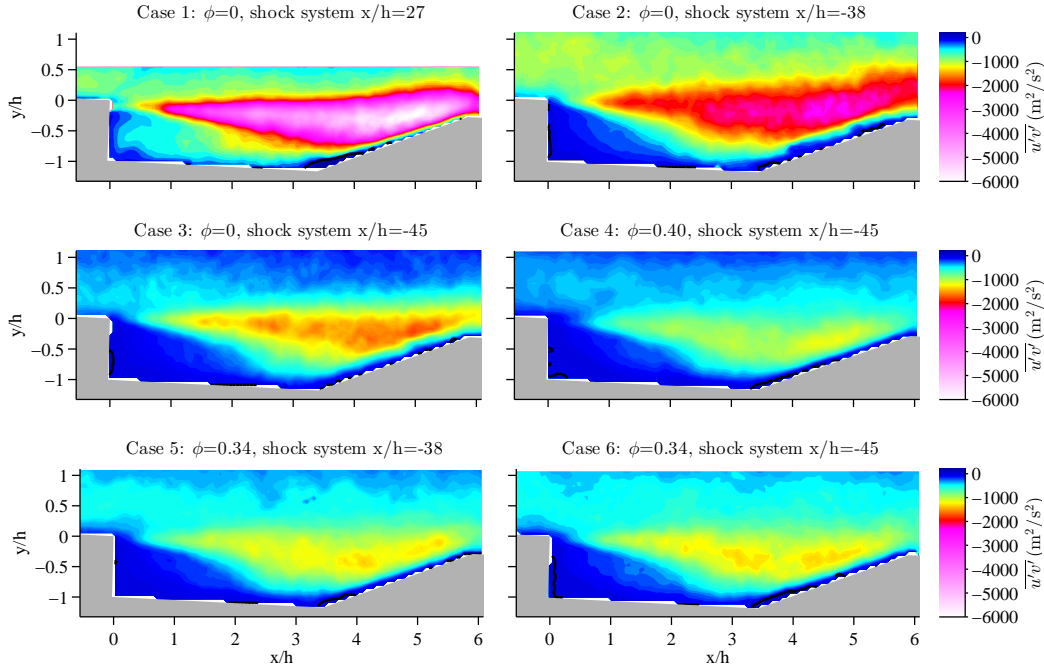


Figure 5.10: Variance of transverse velocity.

Figure 5.11: Covariance of axial and transverse velocities, with contour line at $\overline{u'v'} = 0$.

Case	Turbulence intensity (%)
1	8.51
2	21.7
3	17.0
4	15.6
5	18.0
6	18.2

Table 5.2: Turbulence intensity averaged along a line between points $x/h = 0$, $y/h = 0$, and $x/h = 0$, $y/h = 0.55$.

cavity, with additional small pockets of positive correlation located on the underside of the shear layer in some cases. While Figs. 5.9 and 5.10 show relatively uniformity of variance of axial and transverse velocity above the shear layer, Fig. 5.11 demonstrates that the magnitude of correlation between the two decreases with vertical distance from it.

This result may be explained by the fundamental process of fluid exchange between the cavity and main duct: a fluid parcel moving from the low-speed cavity interior into the main duct represents a negative fluctuation in axial velocity and a positive one in transverse velocity, and vice-versa for one taking the opposite path. Locations higher in the measurement plane are less influenced by this process, explaining the decrease in correlation magnitude with vertical distance from the shear layer, despite relative uniformity of variance of axial and transverse velocities in the upper region of the measurement plane.

Turbulence intensity, here defined as the ratio of the root-mean-square of fluctuating velocity magnitude to mean velocity magnitude, may be examined at the cavity inflow plane to quantify the turbulent state of the reactants approaching the flame front. Table 5.2 represents an average

Velocity component	Integral length scale (mm)	
	Direction [1,0]	Direction [0,1]
Axial	16.2	4.0
Transverse	3.5	2.8

Table 5.3: Integral length scales at point $x = -0.8$ mm, $y = 3.3$ mm, case 4.

Velocity component	Integral length scale (mm)	
	Direction [1,0]	Direction [0,1]
Axial	15.9	4.4
Transverse	3.4	2.9

Table 5.4: Integral length scales at point $x = -0.8$ mm, $y = 3.3$ mm, case 5.

taken over a line between the coordinate origin and the point $x/h = 0$, $y/h = 0.55$. The trend mirrors that reflected in the velocity variances given in Figs. 5.9 and 5.10, keeping in mind the substantial difference in mean velocity of case 1 relative to the others. Based on similarities of turbulent diffusion of a tracer gas in non-reacting flow to flame structure as visualized with OH PLIF, Cantu et al.¹³³ concluded that freestream turbulence levels were the governing parameter for the angle of flame propagation into the main duct. It is expected that higher turbulence levels will result in a greater flame angle due to enhanced interaction of combustion products with unburned reactants and thus an increased turbulent flame speed.¹⁴⁴

Measurements of Cantu et al.¹³³ demonstrated a small but consistent decrease of flame angle with increasing heat release when the shock system leading edge was held constant at $x/h = -45$. Turbulence intensities of cases 4 and 6 of the present study are consistent with this explanation, as it is seen that increased heat release reduces turbulence intensity at the combustor entrance. Additionally, Cantu et al. found an intermediate flame angle resulted from conditions similar to case 5 but at a somewhat lower equivalence ratio ($\phi = 0.31$ vs. $\phi = 0.34$), again consistent with relative turbulence intensities given in Table 5.2.

Turbulent fluctuations are relevant not only to the rate of flame propagation but to the size of turbulent structures that may transport energy and mass between the cavity and main duct. Referring to Eq. (1.2), it is seen that ensemble measurements of a velocity component may be used to define the length over which fluctuations in that component are correlated. Integral length scales in both the axial [1,0] and transverse [0,1] directions were calculated for both measured components of velocity at the point $x = -0.8$ mm, $y = 3.3$ mm, located above the cavity leading edge, and are presented in Tables 5.3 and 5.4.

The result that the integral length scale of axial velocity in the positive axial direction exceeds the others by a factor between three and four is not surprising, since turbulent fluctuations are stronger in the axial direction (Fig. 5.9 vs. 5.10) and the mean flow is predominantly in this direction (Fig. 5.7). Comparison of Tables 5.3 and 5.4 show that changing heat release from near one end of flowpath operability limits to the other has an insignificant effect on length scales, reinforcing the notion seen in Figs. 5.9-5.11 that once heat release is established, changes in its magnitude or the configuration of the pre-combustion shock system yield only minor changes to the turbulent state of the flameholder.

Velocity variance of case 4 may be compared with PLIF imaging of the OH radical to evaluate the impact of turbulent transport on flame stabilization. Relatively-uniform and high mean OH concentrations fill the aft two-thirds of the cavity, a region that includes the maximum velocity variances but whose shape does not suggest correlation with them. Referring to Fig. 5.5b, the

greatest fluctuations in OH concentration occur in a narrow region extending from a few millimeters aft of the top of the cavity forward face and out into the main duct at a shallow angle. Upon comparison with Figs. 5.9-5.11, it is seen that the highest velocity variances border the greatest fluctuations in heat release, lending support to the expectation that main-duct combustion is piloted by the unsteady transport of high-temperature products and radical species from the cavity interior through the shear layer.

The present data do not by themselves indicate whether these maximum fluctuations in OH concentration result primarily from turbulent transport of OH generated within the cavity or that produced locally by reactions piloted by products of cavity combustion. Corresponding measurements of CH^* chemiluminescence by Allison et al.⁶⁰ suggest the latter, as they found the highest intensities occur in the same region where OH fluctuations are the highest. The distribution of the CH^* radical is limited to regions closer to the flame front than that of OH, making it a better indicator than OH of the precise location of heat release.¹⁴⁵ Simultaneous PLIF measurements of OH and CH_2O would provide additional insight into this mechanism, since the reaction zone of hydrocarbon flames may be identified by the maximum product of the concentrations of these two species.¹⁴⁶

A comparison of OH PLIF results with variance of transverse velocity and its covariance with axial velocity (Figs. 5.10 and 5.11, respectively) is most relevant, since it is the unsteadiness in transverse velocity that drives mass exchange. Referring to Fig. 5.8, it is seen that the vertical limit of the region of maximum swirling strength is coincident with that of these two quantities. Vortical structures serve to rapidly exchange mass and momentum across the shear layer, and this result suggests localized combustion in the main duct adjacent to the cavity is dependent upon the ejection of combustion products from the cavity interior by rotational fluid parcels in the shear layer. Similarly, sustained reactions within the cavity are dependent on turbulent entrainment of unreacted fuel and air from the main duct, although the much higher residence time of the cavity serves to decrease temporal variation in its heat release, as the lower standard deviation of OH concentration in this region demonstrates.¹³³

5.4 Conclusions

Particle image velocimetry measurements were acquired in the spanwise center plane of the cavity flameholder of a hydrocarbon-fueled scramjet operating in the premixed dual-mode regime, as well as a baseline fuel-off supersonic case. Persistent challenges in maintaining optical access to similar flowpaths were resolved with the novel use of graphite tracers, which were shown to yield acceptable flow tracking and durability in the high-temperature environment. The use of an air throttle to match the pre-combustion pressure rise for both of two fueling rates studied, but under adiabatic conditions, allowed the impact of heat release on flameholder operation to be decoupled from upstream aerodynamics.

The addition of a shock system upstream of the combustor served to broaden the shear layer and reduce peak magnitudes of fluctuating velocity and swirling strength. Mean velocity magnitudes were reduced by the inclusion and lengthening of the shock system, but once it reached the longer of the two configurations examined the addition of heat release had insignificant effects. In contrast, comparison of cases with and without combustion indicated flameholder turbulent aerodynamics were dominated by the presence of heat release and not its magnitude or shock system strength, since variation among fuel-on cases was minor compared to that among the adiabatic cases. Heat release reduced the magnitude of the shear layer velocity gradient as well as turbulent fluctuations and eddy production throughout the cavity. The importance of reaction models in numerical simulations is thus highlighted, since modeling a downstream obstruction that produces a pre-combustor shock system in a non-reacting flow will yield aerodynamic similarity only for the mean and not turbulent velocities, the latter of which govern the ability of a cavity flameholder to pilot combustion in the

remainder of the flowpath.

Turbulence intensity at the combustor entrance was shown to be positively correlated with flame angle, demonstrating that flame propagation into the main duct is governed by the upstream turbulent boundary condition. Comparison of variance and covariance of velocity with measurements of the OH radical showed that the strongest turbulent fluctuations and vortical structures were adjacent to the greatest fluctuations in OH concentration, demonstrating how main-duct combustion is governed by the intermittent release through the shear layer of high-temperature products and radical species generated in the low-speed cavity interior. Interpretation of these results in light of an earlier investigation of CH^* chemiluminescence suggested this region of maximum variation in OH concentration represented local production of OH by cavity piloting, and not turbulent transport of OH generated within the cavity.

Chapter 6

Flameholder-Main Duct Interface: Dual-Mode

6.1 Introduction

Several investigators have applied two-component particle image velocimetry to the spanwise center plane of a scramjet cavity flameholder,^{39,40,42,45} in addition to the present research. Given the fundamental role of the cavity flameholder in allowing fuel and air to react and pilot main-duct reactions, evaluating the complete three-dimensional velocity field is critical to understanding both the residence time offered to reactants as well as the process of turbulent exchange that enables hot combustion products to be transported into the main duct and fresh reactants to become entrained in the cavity.¹⁶ The relevance of prior PIV studies in the spanwise center plane of the cavity is thus contingent on the degree of two-dimensionality of the flow, since spanwise variation of any velocity component will affect flameholding performance.

Combustion imaging studies have provided an indication of the existence of spanwise variation in flow patterns. Donohue⁸⁵ found substantial spanwise asymmetry of broadband chemiluminescence in the cavity of a hydrocarbon-fueled dual-mode scramjet, attributing the result to aerodynamic coupling with unsteady flow in the pre-combustor isolator section. PLIF measurements by Milligan et al.¹⁰³ demonstrated spanwise asymmetry of the OH radical under conditions of simulated inlet-generated distortion, and Hammack et al.⁸⁰ found indications of unsteady spanwise flow in 10 kHz OH PLIF measurements of an undistorted configuration. Additionally, Reynolds-averaged Navier-Stokes (RANS) simulations of Freeborn et al.¹⁴⁷ suggested small regions of recirculating flow would be established immediately downstream of the forward cavity face, in a plane parallel to the floor.

The only reported experimental configurations able to capture spanwise variation of velocity have applied hydroxyl-tagging velocimetry (HTV) in planes parallel to the cavity floor.^{100,137,148} Of these, only Pitz et al.¹⁴⁸ performed such analysis, finding that spanwise variation in mean and fluctuating velocity magnitude was greatest approximately midway between the cavity floor and the interface with the main duct, and that recirculation in the streamwise floor-normal plane was greatest closer to the spanwise centerline. Corresponding PIV studies have been limited to configurations not specific to high-speed combustion. Beresh et al.¹¹⁰ found in a study of a rectangular cavity adjacent to supersonic flow that turbulence intensity and magnitude of mean spanwise velocity were greatest near the outer edges of the cavity, with each quantity distributed in a spanwise-symmetric manner. An additional study by the same authors¹⁴⁹ found similar behavior of turbulence intensity for various width-to-length ratios of a rectangular cavity adjacent to a high-subsonic flow.

Three-component velocimetry applied to scramjet-specific cavities has to date been absent from

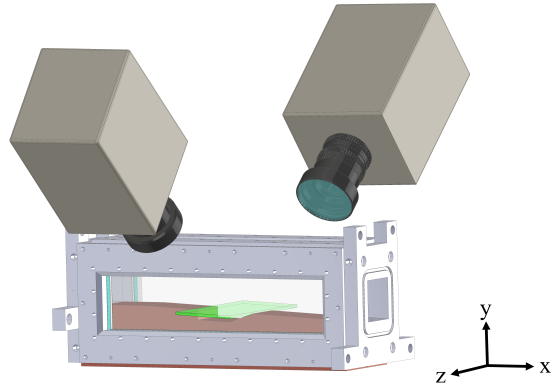


Figure 6.1: Schematic of measurement configuration in cavity top plane.

the literature, although several investigators have applied stereoscopic PIV (SPIV) to other high-speed cavities.^{110,149–152} In addition to the obvious advantage of resolving all three components of velocity, SPIV has the advantage of offering much greater spatial resolution than HTV. It is thus desirable to extend the SPIV technique to the cavity flameholder of a scramjet combustor, and by applying it to the interface of the cavity and main duct of the UVaSCF, spanwise variations may be additionally examined.

This effort addresses the third scientific objective of this dissertation, characterization of the cavity flameholder at steady-state dual-mode conditions, by examining three-component velocity in the plane dividing the cavity and the remainder of the combustor. This is the first reported application of PIV to a scramjet flameholder in a spanwise-oriented plane, as well as the first to apply SPIV to a scramjet cavity in any configuration. This chapter continues with a description of the experimental method, including an evaluation of uncertainty by direct quantification of correlation error. Interpretation of mean and turbulent velocities is presented next, and the chapter concludes with a comparison with the center plane data of Chapter 5 along the line of intersection.

6.2 Experimental Approach

In order to extend the analysis of center plane aerodynamics presented in Chapter 5, the same flowpath configuration and test matrix were used, although as will be subsequently discussed not all test conditions were completed. The measurement plane extends between the leading and trailing edges of the cavity, as depicted schematically in Fig. 6.1. This plane defines the interface across which aerodynamic exchange between the cavity and main duct occurs, and thus may be used to examine the fundamental process by which combustion is maintained.

Laser output was formed into a sheet with a set of integrated optics and propagated through the test section in the spanwise direction, entering and exiting through the side windows, and was viewed obliquely by one camera per side. The shock system present between the tracer injection location and the measurement plane for cases 2-6 resulted in greater mixing of seeded flow and thus lower tracer density than for case 1, and as a result for the subsonic cases a cylindrical lens with a focal length of 38 mm was placed after the exit of the integrated sheet optics in order to reduce the spread of the non-collimated sheet and increase incident laser intensity. A schematic of the measurement configuration is included in Fig. 6.1, where laser optics are omitted for clarity.

The oblique viewing angles of the cameras necessitated use of Scheimpflug adapters, which tilt the camera lens relative to the image sensor to ensure that the planes of the laser sheet, lens,

and image sensor meet at a single line.⁹³ The viewing angle, defined as the difference between the camera lens axis and measurement plane normal, was restricted by available optical access, and was set at approximately 53° , the minimum value that still permitted viewing of the entire measurement plane. In order to have the measurement plane fill nearly the entire image sensor while still maintaining a camera position compatible with the physical constraints of the test facility, each camera was fitted with a 55 mm focal length Nikon lens mounted on a 12 mm extension tube.

Light passing through an interface between media with unequal indices of refraction will experience an angular displacement. In the case of light passing through a window bounded by air on either side, light rays will be displaced laterally, as viewed in the plane of propagation. As a result, the apparent and actual positions of imaged objects in the measurement plane will differ. This does not present complications when particles and the calibration target are both viewed through flowpath windows, as was the case with the center plane measurements, which permitted the target to be inserted by removing the opposite window. Since the measurement plane is viewed through both windows of the present experiment, the only means by which a calibration target could be viewed through both windows simultaneously would have required insertion through the flowpath exit, a solution deemed impractical.

Instead, the cameras and laser optics were mounted on a traverse providing sufficient movement in the y direction such that the measurement plane could be moved clear of the test section while preserving relative alignment of the cameras and laser sheet. Since this removed the apparent displacement due to refraction by the side windows, actual particle images were subsequently compared with an automated routine and the resulting lateral disparity subtracted, a procedure that will be described in greater detail later in this section. A two-level calibration target (LaVision model 058-5) was used, which permitted the calculation of a three-dimensional calibration function without requiring that several images at varying distances between the cameras and target be obtained.

The optical environment of this experiment was substantially more challenging than that of the center plane measurements, resulting in a lower signal-to-noise ratio. Optical performance of the tracer particles of the present study is governed by Mie scattering, since the mean tracer size is smaller than several wavelengths of the incident laser light.¹⁵³ Intensity of scattered light is a strong function of direction, and is greater along rays nearly parallel to incident light than antiparallel, regimes termed “forward” and “back” scattering, respectively. Accordingly, the mean intensity of particle signal was much greater for one camera than the other.

This challenge was compounded by the necessity of viewing flowpath surfaces in the background of the measurement plane, which received laser energy directly from the edges of the sheet itself as well as from reflections from tracer particles and flowpath windows. Since subsequent reflections from flowpath surfaces were diffuse, the noise level was comparable for each camera. This resulted in unequal signal-to-noise ratios between cameras, limiting the utility of adjusting camera aperture, which scales both signal and noise by equal amounts. In an effort to produce equal scattered intensity at each camera location, a mirror was used to reflect the laser sheet back through the test section after its initial exit. This improved the signal-to-noise ratio of the camera viewing backscatter from the initial pass of the laser beam, but not to the level of the other. Since the particular configuration of the laser optics did not result in a collimated light sheet, its dimensions changed slightly as it traversed the test section, and measurements revealed a thickness of 1.2 ± 0.2 mm. In order to equalize signal intensity between cameras, unequal aperture settings were used, and the camera with the higher signal-to-noise ratio was fitted with a 2x neutral density filter to avoid image sensor saturation at scattered intensities sufficient for the other camera. Sample raw images for cases 1 and 4 are given in Figs. 6.2 and 6.3, respectively, where the mean flow direction is from bottom to top.

The raw images for case 4 presented in Fig. 6.3 are representative of all reacting-flow cases, and for reasons discussed previously are distinct from those of case 1. The lower signal-to-noise ratio in camera 2 relative to camera 1 is readily apparent for both regimes, and in the reacting-flow images

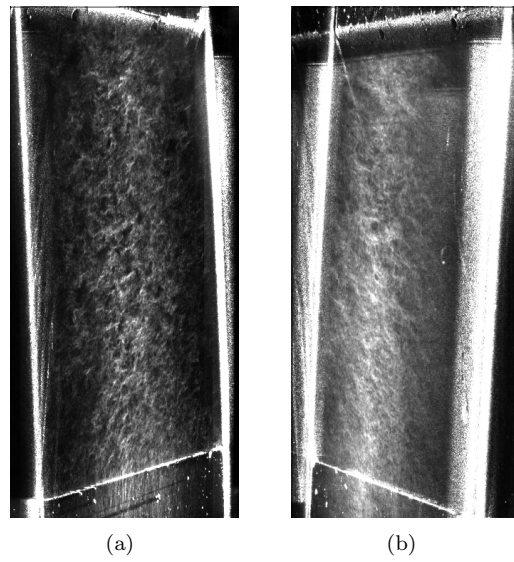


Figure 6.2: Raw images for cameras 1 (a) and 2 (b) for case 1.

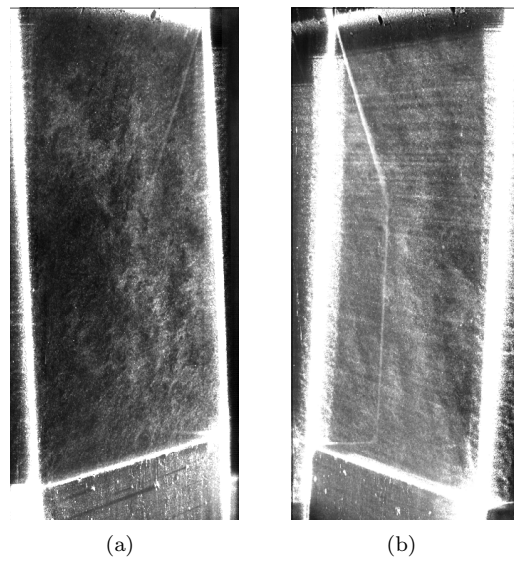


Figure 6.3: Raw images for cameras 1 (a) and 2 (b) for case 4.

a horizontal banding artifact was noted. These bands moved with the mean flow, and an average of all images confirmed that they took no preferential distribution. Their source was not identified but may be related to aero-optical aberrations.

The tracer delivery configuration was unchanged from that used for the center plane measurements, and the flow rate of air required for acceptable tracer density was slightly lower, between 10-11 standard cubic feet per hour (SCFH) versus 13-15 SCFH for the earlier measurements. Since it was already shown (Fig. 5.3) that the higher flow rate resulted in negligible changes to flowpath static pressures, aerodynamic influence of tracer injection is similarly discounted for this experiment. It was found that proper signal levels were much more sensitive to changes in tracer density than in the center plane experiments (laser power was maintained at its maximum value since any reduction leads to increased pulse length and smearing of particle images, degrading correlation accuracy). As a result, a greater number of trials were required to complete each test case, and for cases 2 and 3 tracer densities were ultimately found to have been insufficient to permit meaningful measurements, and will be excluded from subsequent analysis.

2000 image sets were acquired at a rate of 1 kHz for each test condition, with each set consisting of one pair of double-frame single-exposed images per camera. As with the center plane measurements, laser pulse separation was fixed at $1 \mu\text{s}$ for all cases. Vectors were calculated with a procedure very similar to that used with the center plane data. An algorithmic mask was not used, since a fixed mask applied to raw images in the first step of processing adequately excluded areas of poor seeding, and the remaining area contained tracer densities of sufficient uniformity to consistently permit vector calculation. Rather, only pixels whose intensities reached the saturation level of the image sensor were excluded. Prior to vector calculation all images were processed to find the minimum intensity at each pixel location, and this global minimum was subtracted from raw images to reduce the effects of background luminosity on vector calculation.

Vector fields for all cases were again calculated by cross-correlation over round Gaussian-weighted interrogation windows, with iterative increases of spatial resolution with 50% overlap of adjacent windows. Median filters were applied after each pass of the correlation algorithm in the same manner as described in Chapter 5. Final interrogation was performed with windows 8 pixels in diameter, yielding 0.35 mm vector spacing from interrogation windows with a diameter twice this value but overlapped by 50%. Initial interrogation window diameter was 16 pixels for all cases except the first, where it was doubled to accommodate the higher mean velocity.

As discussed previously, the procedure used to acquire a calibration resulted in a non-negligible apparent translation of particle images relative to a corresponding location on the calibration target. This translation may be identified by application of a routine similar to that used to calculate particle displacement between frames of an image, and allows the original calibration function to be modified accordingly.¹⁵⁴ This “self-calibration” procedure resulted in a mean residual of 0.2 pixel, or 2.5% of the diameter of the final interrogation windows. As a result, registration error, which results from erroneous pairings of two-component vectors from each camera used to form a three-component vector,¹⁵⁵ was neglected.

Owing to the relatively poor signal-to-noise ratio observed with camera 2, it is desirable to directly quantify the performance of the vector calculation algorithm for the particular conditions of this study. One method of doing so is by deforming the first frame of each raw image pair by the corresponding instantaneous vector field and applying the same processing algorithm as used to calculate the original vector fields to it and the undeformed image. This *a posteriori* method has the advantage of accounting for factors including tracer particle size and distribution, laser power, background intensity, and flow gradients.^{44,156}

The difference between instantaneous fields of the original and replica PIV data sets was calculated and analyzed statistically to determine measures of systematic and random errors of the correlation technique. For each quantity derived from the original data set, the same was calculated of the replica and normalized by the original to determine a fractional uncertainty. The results of this procedure for each of the three components of mean and variance of velocity are presented in

Figs. 6.4 and 6.5. Due to the similar optical nature of cases 4-6, all are represented by case 4, and case 1 is examined separately. The perspective of the plots views the cavity from above, and regions of absent data represent areas masked due to strong background intensity relative to that of the tracers. For example, the diagonal masked strip in the plots for case 4 corresponds to a reflection from the intersection of the side window with the cavity aft face.

It is easily seen that although mean and variance of axial velocity have uncertainties that clearly permit quantitative analysis, the same cannot be said of the other two components. Transverse velocity, which corresponds to the out-of-plane component, demonstrates near-100% uncertainty, and spanwise velocity does little better. Therefore, only axial velocity will be examined in a quantitative sense; spanwise velocity will be considered only via its variance and instantaneous contributions to velocity magnitude and swirling strength, all on a qualitative basis; and transverse velocity will be excluded entirely.

Additional sources of systematic uncertainty are those due to calibration errors in target scaling and residuals of the mapping function, as discussed in Chapter 5. Statistical convergence error will again be considered as a contributor to random error. Since particle slip and thermophoresis were found to be orders-of-magnitude lower than other error sources in the spanwise center plane, where the corresponding velocity and thermal gradients are stronger, they will be neglected in the present analysis. Correlation error as calculated according to the methods described earlier in this chapter has the advantage of isolating systematic error for mean quantities and random error for fluctuations, and thus captures the relevant errors of vector calculation for both average and variance of velocity.

6.3 Results

A series of four consecutive instantaneous velocity fields is presented for each of the four test cases in Figs. 6.6-6.9. Since transverse velocity was neglected, the plots include the magnitude of the in-plane components and overlaid path lines. As with all plots presented in this section, contours for case 1 are given with a color scaling distinct from the remainder to accommodate the disparity in magnitudes. Particularly notable is the substantial variation in velocity magnitude near the downstream end of the measurement region, corresponding to the zone of shear layer impingement on the cavity aft face. Velocities near both extremes of the range observed over the entire plane are found here, and the lowest magnitudes are accompanied by local path line curvature, suggesting the presence of vortices convected with the local mean velocity. The strong temporal variation of in-plane velocity magnitude supports the findings of the center plane analysis, since the present measurement plane is located near the maximum mean velocity gradient in the shear layer, which is maintained by the continuous and unsteady exchange of fluid between the high-speed main duct and the low-speed cavity interior.

Also of note is substantial concentration of missing vectors, the result of rejection by median filters. Since the same filters were applied to this data set as that in the center plane, this result provides additional indication of the lower quality of the images of the present experiment. Strong correlation of particle signal and little background noise would be expected to yield few candidate vectors differing sufficiently from their immediate neighbors to merit rejection by the median filters.

Mean axial velocity is presented in Fig. 6.10. The reacting-flow cases are broadly similar but show greater variation among themselves than in the center plane (see Fig. 5.7 for plots of velocity magnitude, which at the line of intersection is dominated by the axial component). Velocity is greater near the spanwise centerline than toward the edges of the cavity, a result particularly pronounced in the lone case with the leading edge of the shock system at $x/h = -38$ (case 5). Axial velocity steadily increases as the mean flow moves downstream from the leading edge of the cavity, then slows slightly as the shear layer interacts with and is slowed by the aft face.

The fuel-off supersonic case displays a unique characteristic in the streamwise-orientated strip

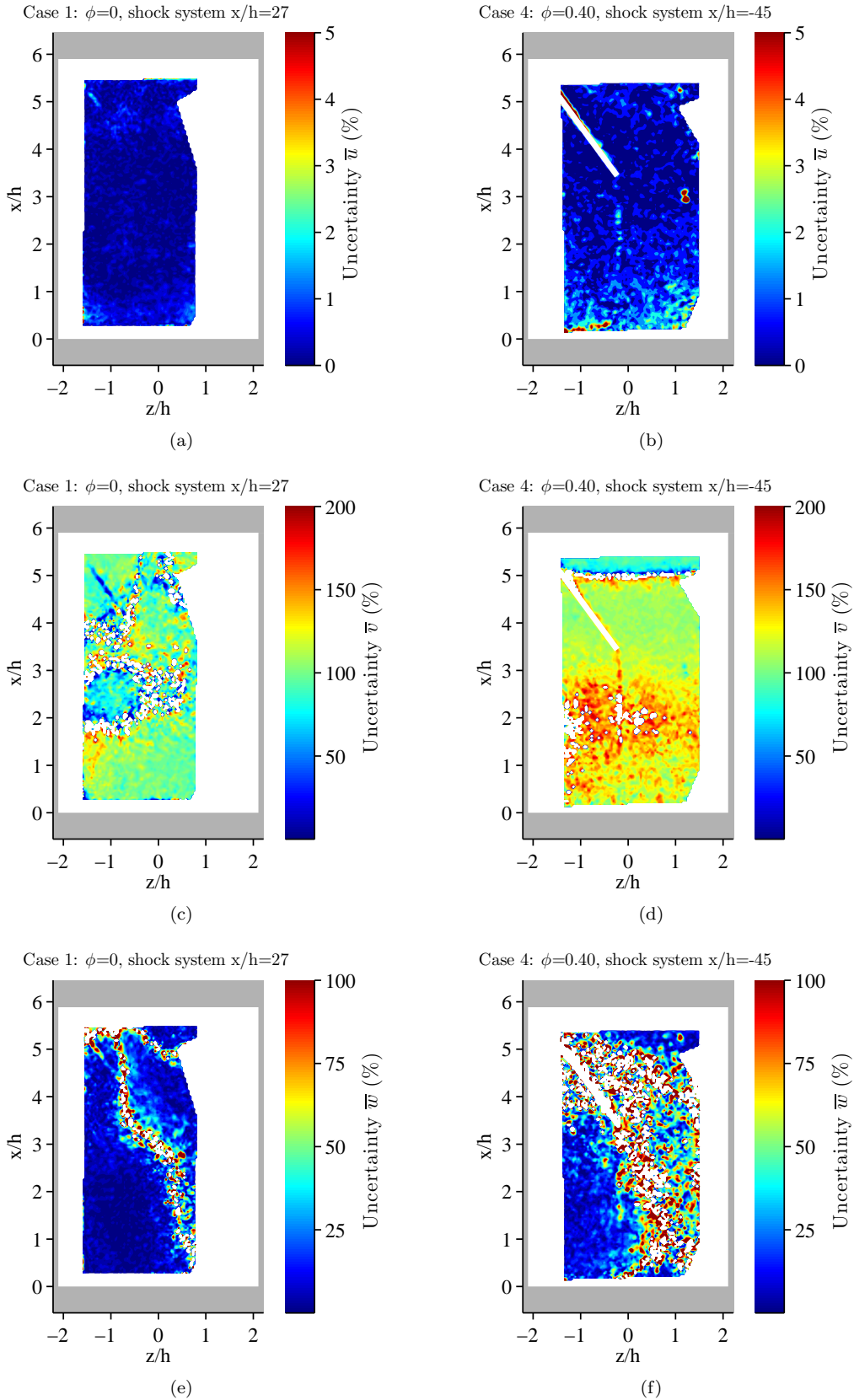


Figure 6.4: Correlation uncertainty of mean velocity.

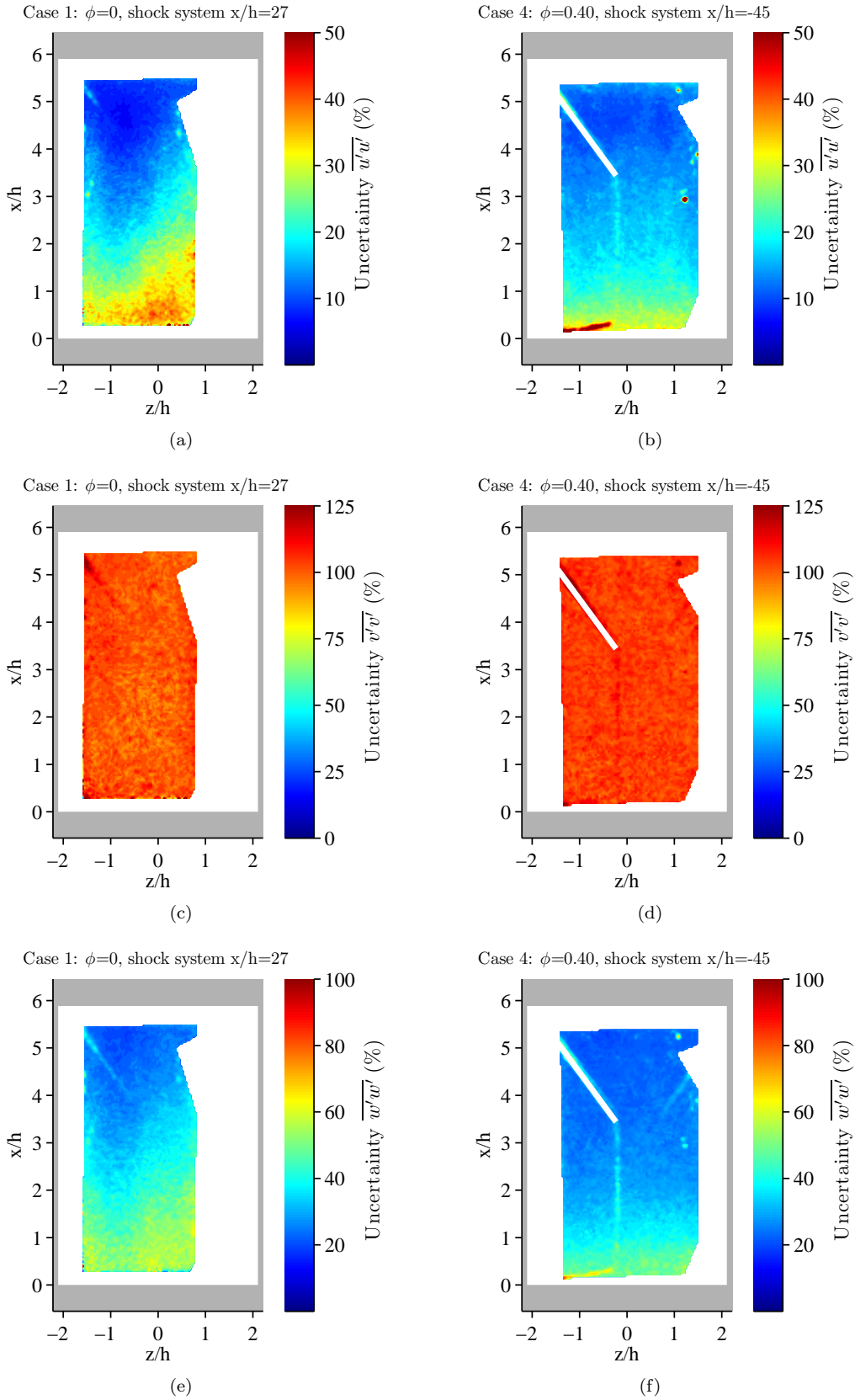


Figure 6.5: Correlation uncertainty of variance of velocity.

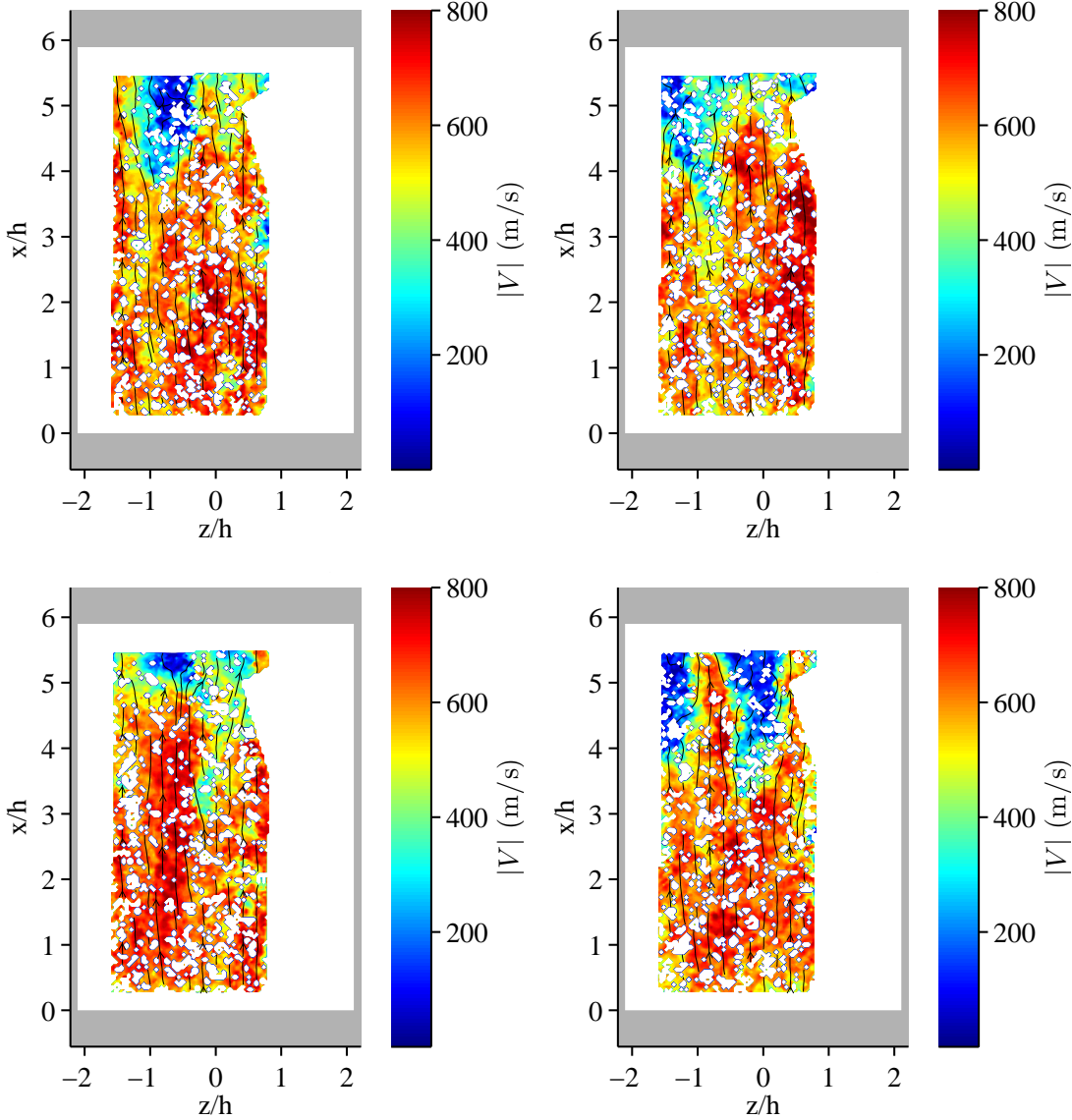


Figure 6.6: Sequences of instantaneous velocity fields, case 1 ($\phi = 0$, shock system $x/h = 27$).

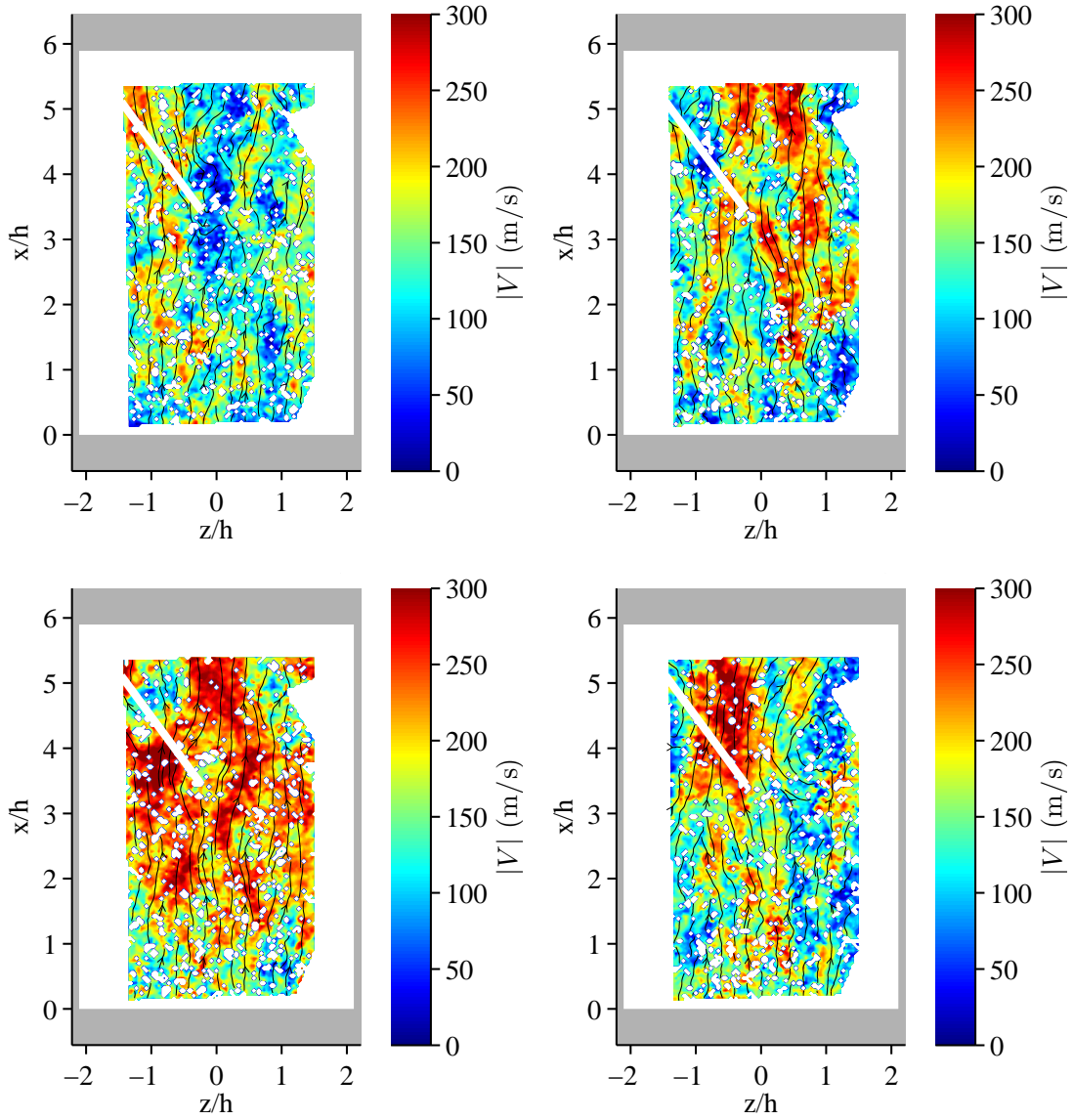


Figure 6.7: Sequences of instantaneous velocity fields, case 4 ($\phi = 0.40$, shock system $x/h = -45$).

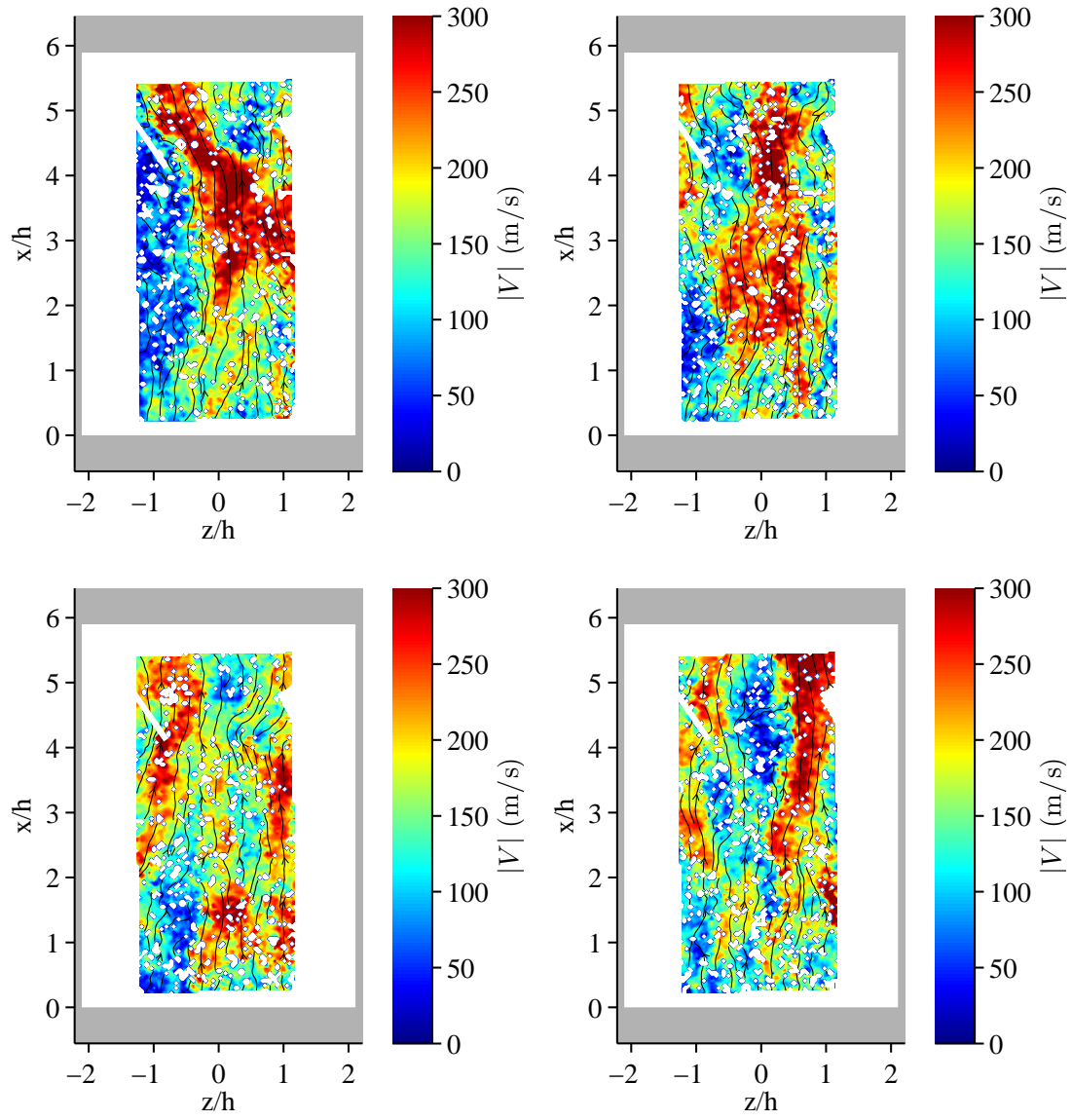


Figure 6.8: Sequences of instantaneous velocity fields, case 5 ($\phi = 0.34$, shock system $x/h = -38$).

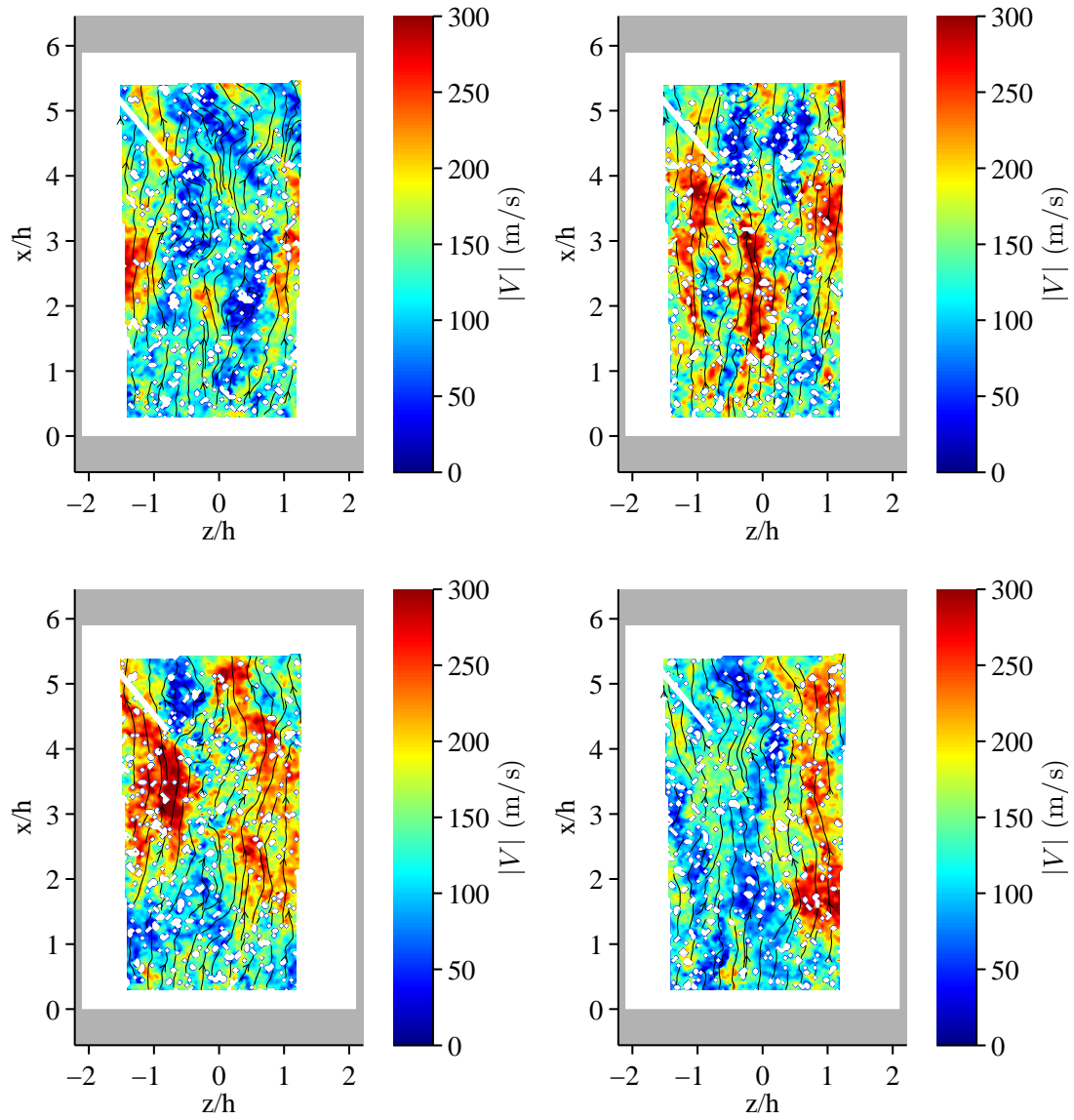


Figure 6.9: Sequences of instantaneous velocity fields, case 6 ($\phi = 0.34$, shock system $x/h = -45$).

of lower mean axial velocity centered at $z/h = -0.7$. On comparison with variance of axial velocity given in Fig. 6.11, it is seen that this corresponds to a region of exceptional unsteadiness. The four realizations of instantaneous velocity magnitude in Fig. 6.6 provide a limited but nonetheless instructive visualization of the phenomena leading to these statistical results, where it is seen that the downstream end of this finger-like region demonstrates large changes in velocity between successive acquisitions.

Variance of axial velocity for the fuel-on cases steadily increases with downstream distance from the cavity leading edge, reaching a maximum at the location of shear layer reattachment at the aft face (see Fig. 5.9 for corresponding center plane data). Cases 4 and 5 display a spanwise-symmetric pair of regions of elevated variance above the cavity aft face, a behavior that may barely be distinguished in case 6. Trends in variance in spanwise velocity are largely similar (Fig. 6.12), with the exception of greater spanwise uniformity.

It is instructive to examine turbulence intensity, which relates the magnitude of velocity fluctuations to the mean value. Fig. 6.13 presents this metric as calculated from only in-plane velocity, since the third component was previously shown to have excessive uncertainty. It is seen that for the subsonic cases turbulence intensity is higher near the spanwise edges of the cavity, and reaches a maximum just upstream of the trailing edge. This corresponds with findings of Beresh et al.¹⁴⁹ in a rectangular cavity also adjacent to a high-subsonic freestream but under non-reacting conditions. Beresh et al. did find separately¹¹⁰ that a supersonic non-reacting cavity demonstrated the same behavior, which does not correspond with the present results, as seen for case 1 in Fig. 6.13. Both studies by Beresh et al.^{110,151} considered a measurement plane displaced above the top of cavity by 5% of its depth. The half-width of the laser sheet of the present study is 7% of the cavity depth, whereas the corresponding figure for the studies of Beresh et al. is 3%, so the measurement regions of the two investigations may be considered to overlap. It bears repeating that variance of spanwise velocity (and its contribution to turbulence intensity) must be considered in the context of correlation uncertainty (Figs. 6.5(e) and 6.5(f)), and provides only an indication of qualitative trends across the measurement plane.

Mean swirling strength is presented in Fig. 6.14. Case 1 is the only one of the four considered that displays any notable variation across the measurement plane. Swirling strength in approximately the upstream third of the plane is at least 50% lower than elsewhere, and values steadily increase as the mean flow approaches the cavity aft face. The region of maximum mean swirling strength corresponds with that of variance of turbulence intensity, indicative of the highly unsteady nature of shear layer reattachment. The subsonic reacting-flow cases show much greater spatial uniformity. Cases 4 and 6, which both place the leading edge of the shock system at $x/h = -45$, are nearly identical, and have intensities approximately 10% lower than in case 5, where the shock system begins at $x/h = -38$, suggesting swirling strength in the top plane is more strongly influenced by isolator aerodynamics than heat release. This analysis is limited by the lack of data at subsonic non-reacting conditions, but the results are consistent with those in the center plane (Fig. 5.8).

The validity of the PIV technique may be assessed by comparison of data acquired in the center and top planes along their line of intersection. Such a comparison is presented for the mean and variance of axial velocity, since this is the only component considered suitable for quantitative analysis common to both measurement configurations. Figs. 6.15 and 6.16 present the quantities themselves as solid lines, with dashed lines corresponding to uncertainty intervals. Both quantities consider uncertainty due to correlation error (as described in Sec. 6.2) and finite sample size (see Sec. 5.2.2), while that of mean velocity also includes the systematic error terms due to calibration.

An additional source of uncertainty results from the spatial averaging in the out-of-plane direction inherent to the PIV technique. As a result, true flow variations within the thickness of the laser sheet are not captured. This becomes a concern in comparison of orthogonal PIV planes when the laser sheet thickness of one plane is substantially greater than the vector spacing of the other. The top plane sheet thickness is 240% of the distance between adjacent center plane vectors, whereas

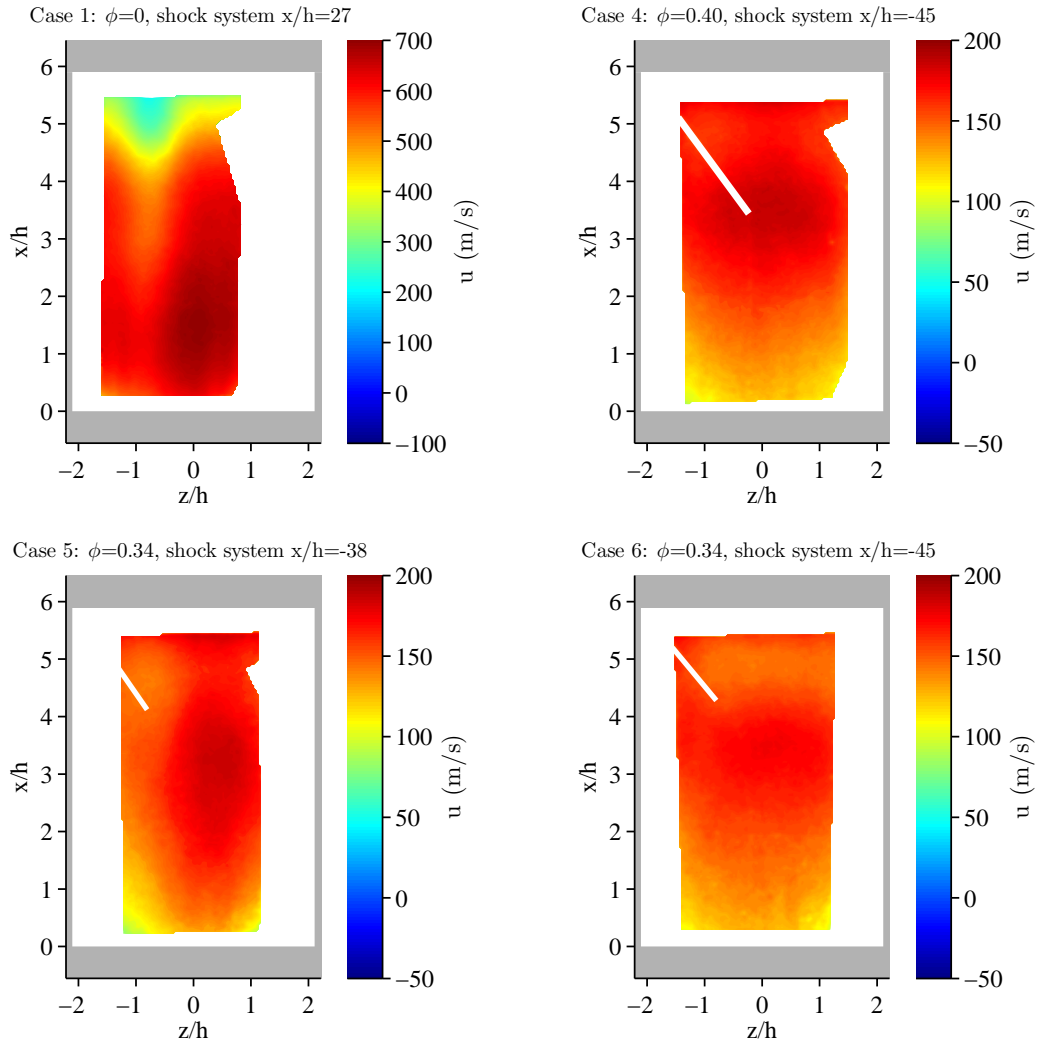


Figure 6.10: Mean axial velocity.

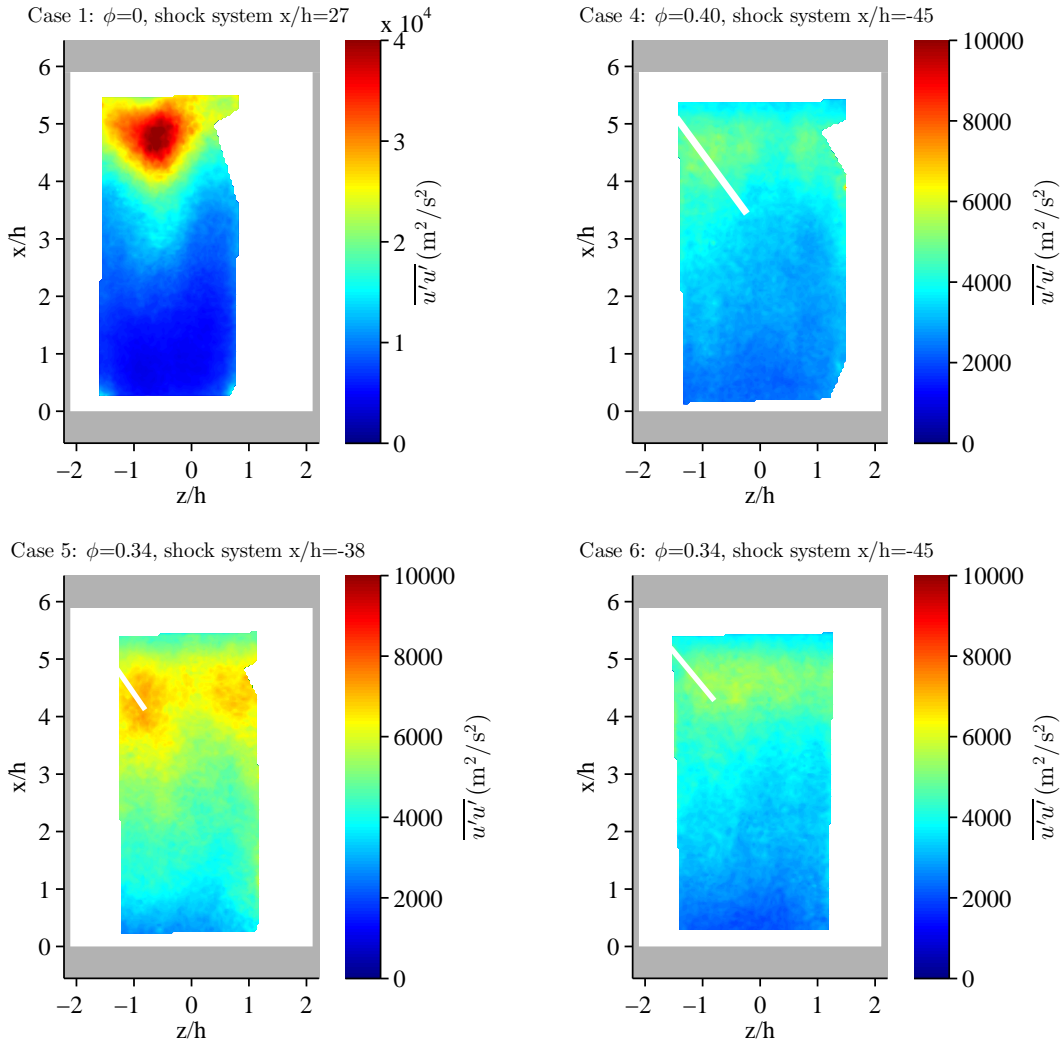


Figure 6.11: Variance of axial velocity.

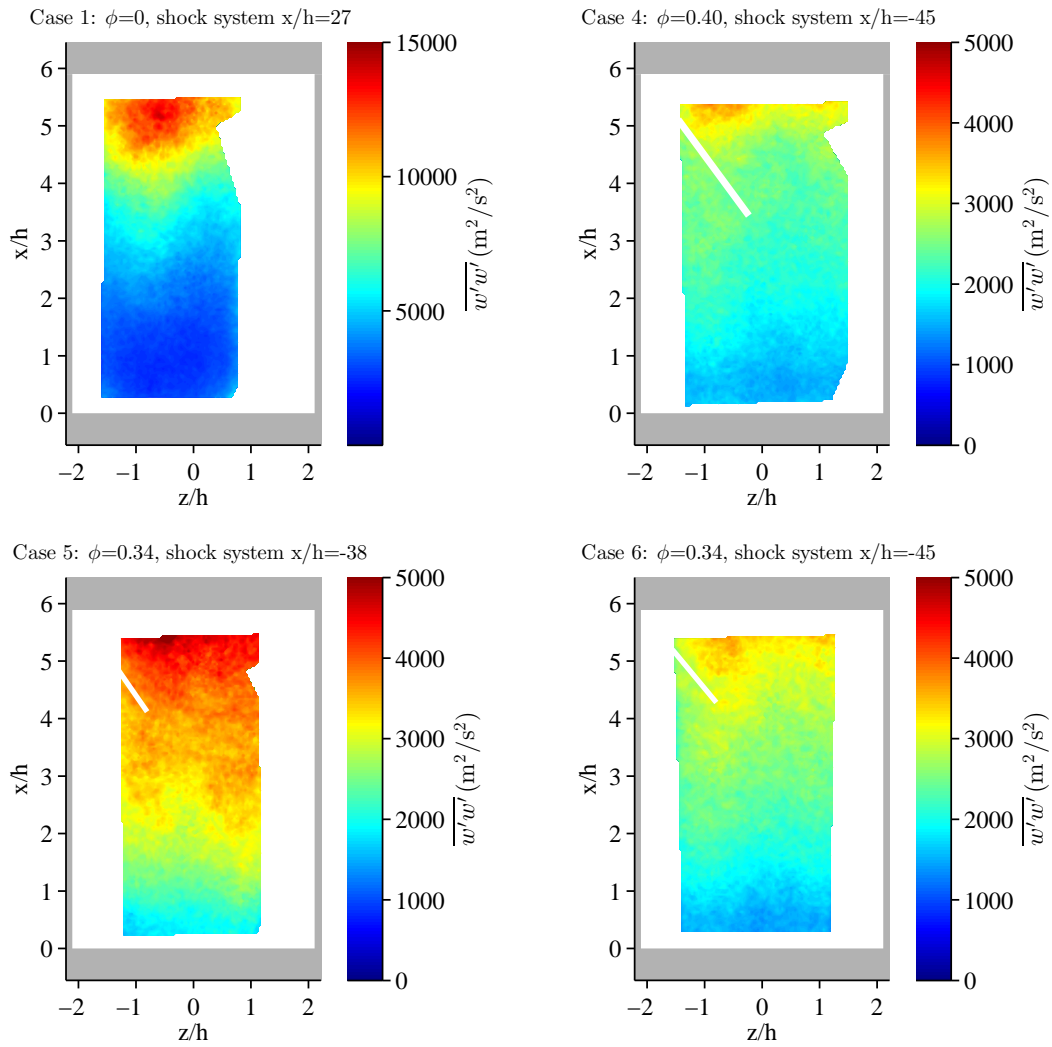


Figure 6.12: Variance of spanwise velocity.

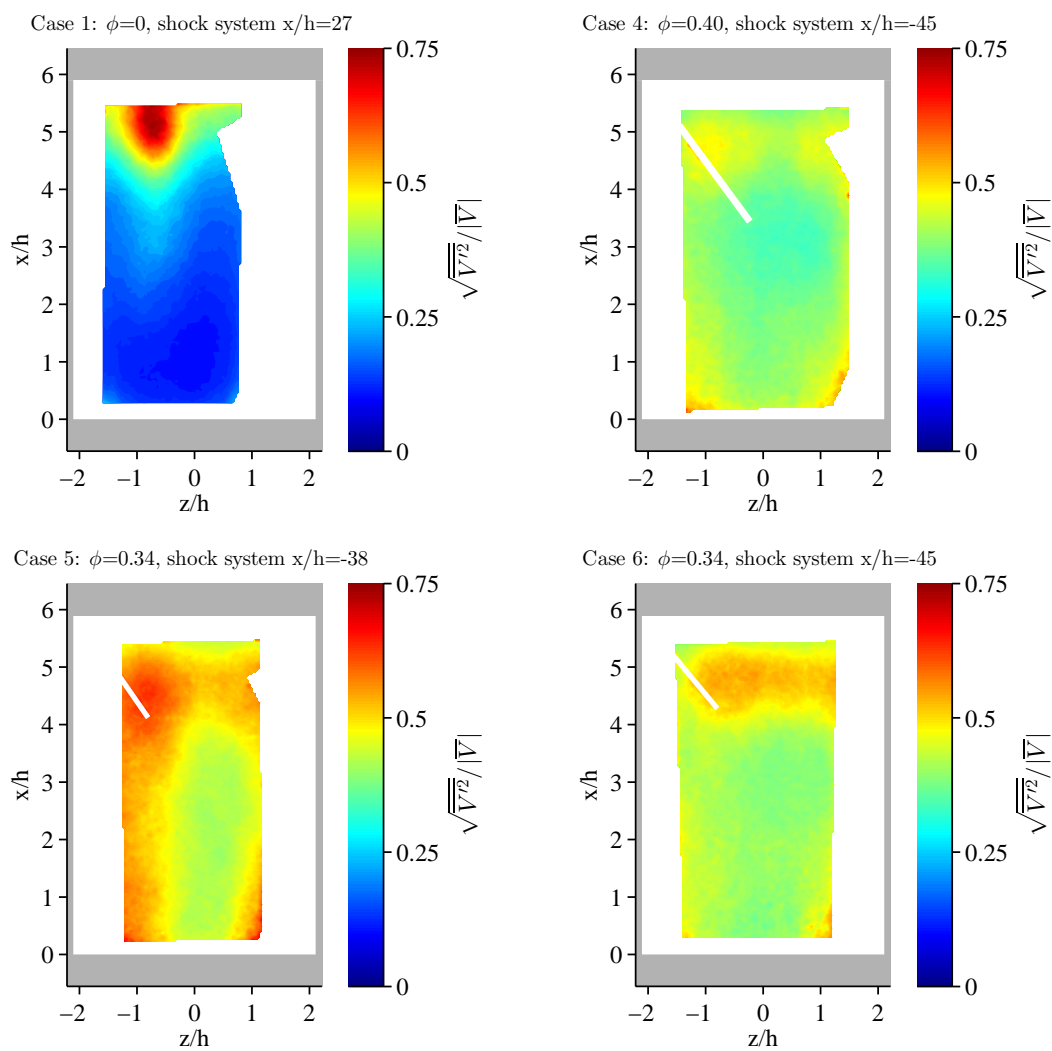


Figure 6.13: In-plane turbulence intensity.

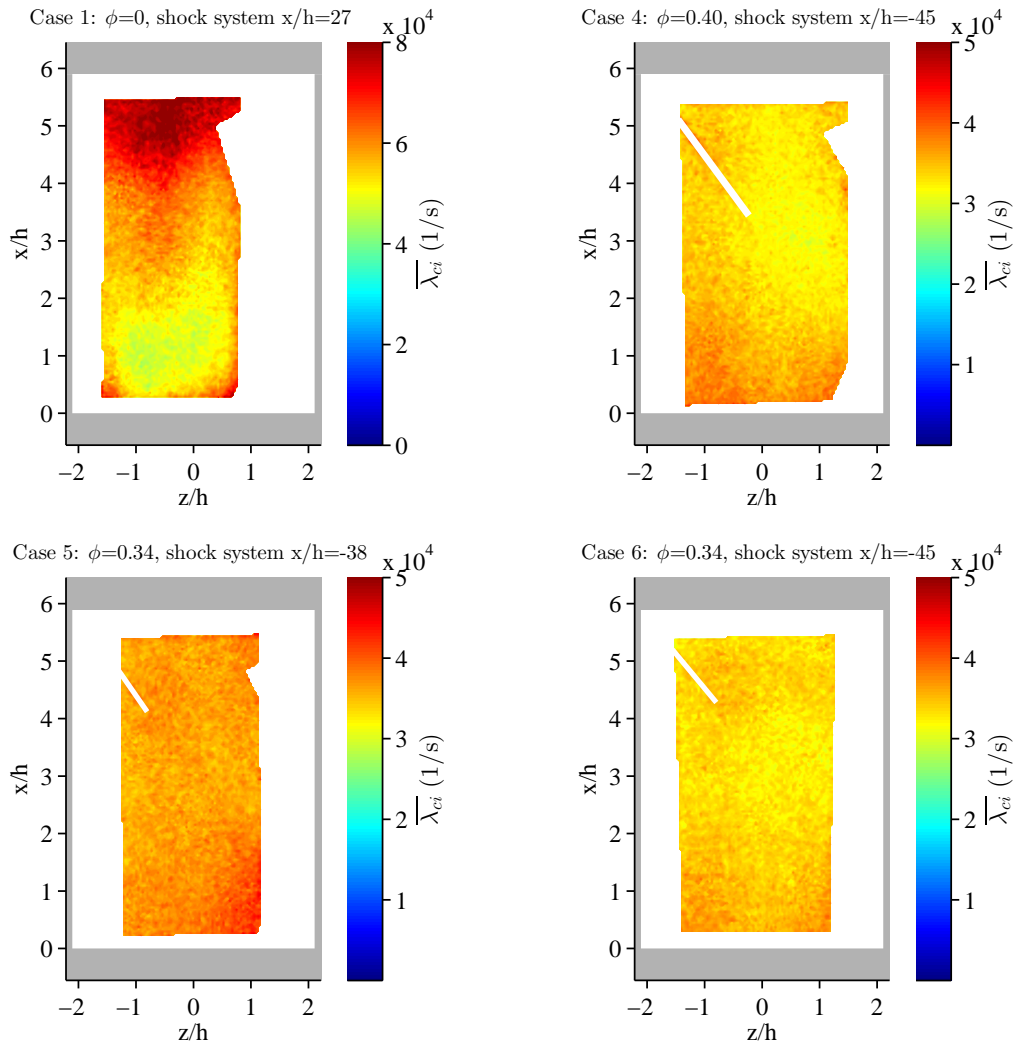


Figure 6.14: Mean swirling strength.

the converse is 70%. This indicates that three center plane vectors fit within the thickness of the top plane measurement volume, lending ambiguity to comparison of data notionally distributed along a line. As a result, the maximum variation of center plane data over its intersection with the entire top plane measurement volume was found and included in the total uncertainty interval. A similar calculation was not performed for the top plane due to its large vector spacing relative to the thickness of the center plane laser sheet.

The configuration of data acquisition in the cavity top plane resulted in strong laser reflections from the cavity edges, which were used to align vector fields with flowpath boundaries. Whereas cavity reference features were identified with negligible spatial uncertainty in the center plane measurements, there was 1.2 mm of uncertainty in defining a reference location for measurements in the top plane. Since the through-plane boundaries of an interrogation volume imaged by a camera will be parallel to the angle at which the camera views the measurement plane, the particular configuration of the present experiment yielded interrogation volumes whose intersection with the top of the laser sheet was displaced spanwise relative to that with the bottom. It can be easily shown that the magnitude of this displacement equals the product of the laser sheet thickness and the tangent of the camera viewing angle, and was 1.7 mm for this study. These two terms were combined in a root-sum-square fashion to find the uncertainty due to spatial averaging and alignment error in the spanwise direction of 2.1 mm. Similar to the calculation performed with the center plane data, the top plane data were probed across a strip of width equal to this uncertainty, and the maximum variation was added to the total uncertainty interval.

The total uncertainty represented by the dashed lines in Figs. 6.15 and 6.16 was calculated by combining uncertainties due to correlation error and finite sample size (at a 95% confidence interval) in a root-sum-square, then adding the terms resulting from uncertainty in defining the line of intersection of the two planes. These alignment terms are considered to be systematic errors, and as such were not included in the root-sum-square along with correlation error and statistical uncertainty, which are random errors.

Referring to Figs. 6.15 and 6.16, it is seen that the mean and variance of axial velocity agree within experimental uncertainty for all four test conditions, and that qualitative trends are replicated. The dominant source of uncertainty in comparison of mean velocity is due to flow variations through the thickness of the top plane, which leads to uncertainty in excess of 50% near the leading edge of the cavity, where velocity gradients are greatest (cf. Fig. 5.7). Fig. 5.9 shows gradients of axial velocity variance are shallower along the line of intersection of the two planes, resulting in smaller confidence intervals. The uncertainty intervals presented here must be interpreted with caution, since terms accounting for uncertainty in locating the line of intersection of the two planes have been included in addition to the uncertainties of the independent measurements themselves.

Finally, swirling strength in the two measurement planes will be compared. Unlike in Figs. 6.15 and 6.16, Fig. 6.17 presents distinct quantities, orthogonal components of swirling strength, which would be expected to be equal only in the case of isotropic turbulent structure. Only terms resulting from relative alignment of the two planes and spanwise spatial averaging of the top plane data are included in the plotted uncertainty intervals. The reacting-flow cases demonstrate a nearly-constant degree of eddy anisotropy, both along the axial profile as well as among the three cases, with eddies in the top plane much stronger than those in the center. This finding of only small changes in eddy behavior among the three reacting-flow cases is similar to that found in the center plane (cf. Fig. 5.8). Case 1 is distinct, and demonstrates both smaller magnitude as well as a notable spatial dependence of the ratio of the two components, which crosses through unity near the cavity midpoint.

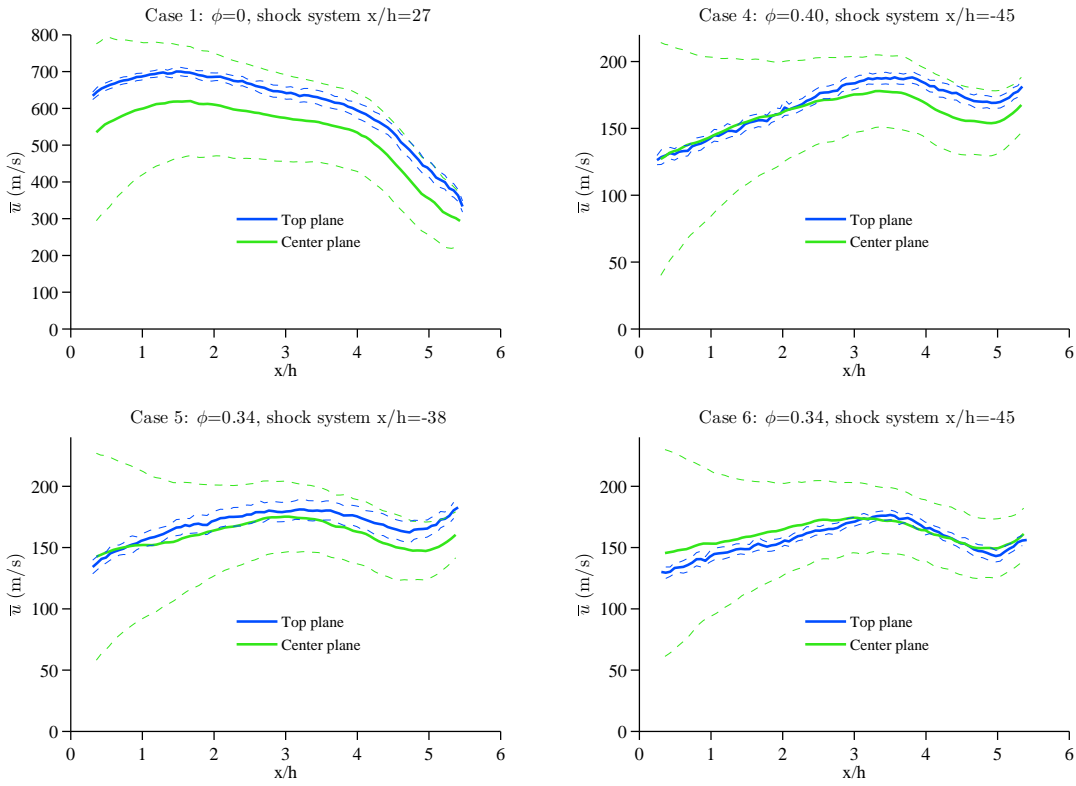


Figure 6.15: Comparison of mean axial velocity (solid lines) in center and top planes with corresponding uncertainty intervals (dashed lines).

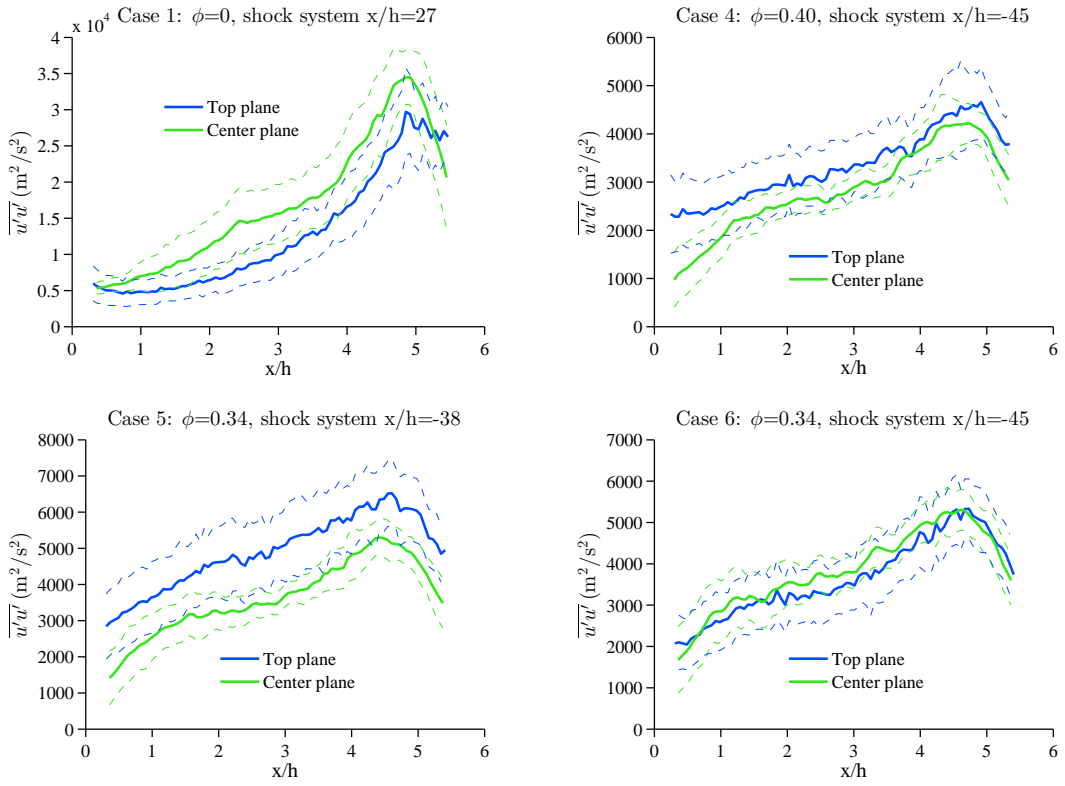


Figure 6.16: Comparison of variance of axial velocity (solid lines) in center and top planes with corresponding uncertainty intervals (dashed lines).

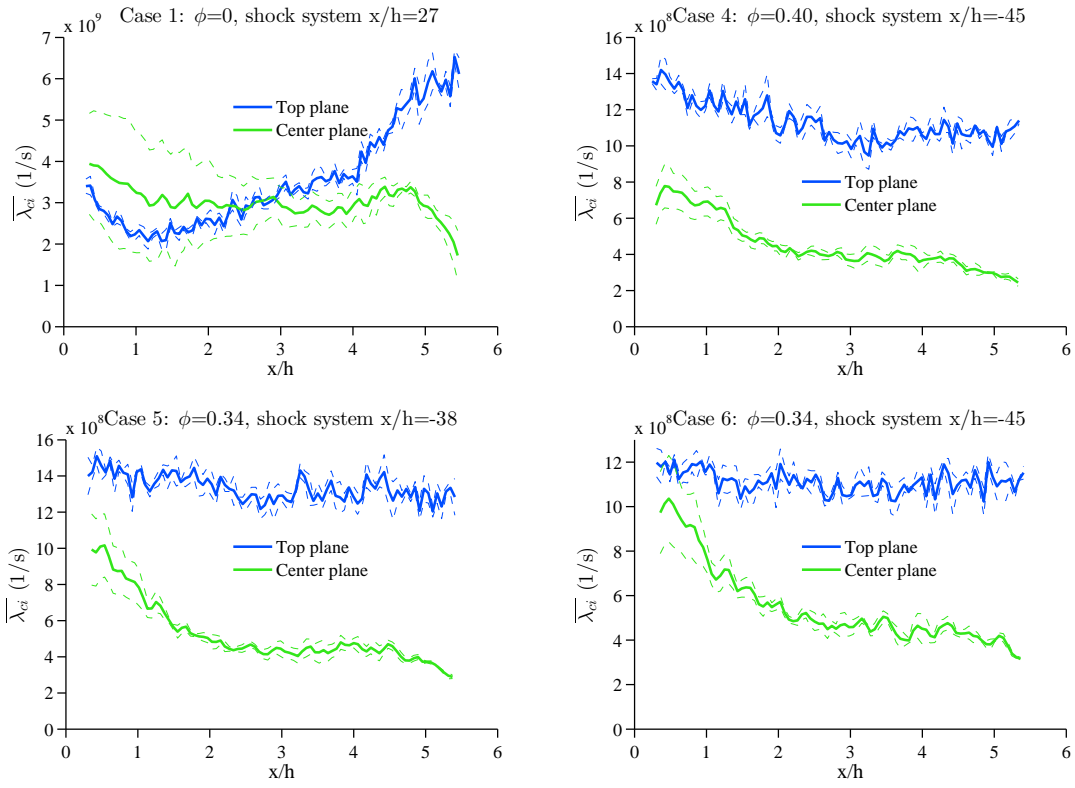


Figure 6.17: Comparison of mean swirling strength (solid lines) in center and top planes with corresponding uncertainty intervals (dashed lines).

6.4 Conclusions

Stereoscopic particle image velocimetry (SPIV) measurements were acquired in the upper boundary plane of the UVaSCF cavity flameholder in order to quantify the degree of spanwise variation of velocity statistics as well as investigate application of the SPIV technique to a cavity-based supersonic combustor. This study represents the first application of SPIV to a scramjet cavity flameholder, as well as the first PIV measurements for such a flameholder not in the spanwise center plane. Experiments were challenged by a low signal-to-noise ratio, a result of reflections from flowpath surfaces as well as directionally-unequal intensity of scattered light from tracer particles. Geometric constraints required an angle between the camera lens axis and the measurement plane normal so great that the rhombohedral interrogation volumes had bases displaced by an amount greater than their height, resulting in spatial averaging in the direction of displacement. When located within a strong flow gradient, this effect increases the variation of velocity present within the volume, diminishing correlation of particle images between frames. Similarly, the placement of the measurement plane in a region of strong through-plane gradients weakened correlation via spatial averaging across the thickness of the laser sheet, which exceeded vector spacing by a factor of 3.6. Accordingly, future investigations would benefit from examination of measurement planes parallel to that of the present experiment but closer to the cavity floor, where flow gradients are expected to be weaker, as seen in Fig. 5.7. The necessity of reflecting the laser sheet back through the test section to present equal particle scattering to each camera and the use of non-collimating optics complicated efforts to reduce sheet thickness, suggesting volumetrically-resolved (tomographic) PIV would be beneficial to future investigations.

The physical constraints of the flowpath required calibration images be acquired externally, and a self-calibration routine based on correlation of particle images was performed to reconcile the disparity in apparent position due to refraction of light rays by flowpath windows. This process was itself challenged by thick laser sheets and large viewing angles, since the technique is dependent on identical images between cameras. Greater differences in perspective between the two cameras and a thicker laser sheet will decrease the similarity of the views acquired by each camera of tracers in a particular location, leading to degraded accuracy in determination of the calibration disparity.¹⁵¹

A direct analysis of correlation performance was performed by deforming raw particle images by the measured velocity field and processing the result with the same vector calculation routine. Comparison with the original velocity field showed that only the axial component was captured with accuracy sufficient to warrant quantitative analysis. The spanwise component, which suffered from spatial averaging due to large camera viewing angle, was interpreted only via its variance and in a strictly-qualitative sense. Mean spanwise velocity demonstrated strong spatial variation in its uncertainty, while that of the variance was more uniform, suggesting background intensity features introduced a bias into the correlation field. Both mean and variance of transverse velocity were excluded from analysis due to uncertainties on the order of the quantities themselves.

Select instantaneous measurements revealed a highly unsteady flow dominated by turbulent structures, which became most prominent near the location of shear layer reattachment at the cavity aft face. In-plane turbulence intensity was found to be highest at this location, corresponding with prior measurements in the spanwise center plane. The subsonic reacting-flow cases additionally demonstrated that turbulence intensity was greatest toward the spanwise edges of cavity, corresponding with prior studies of a subsonic but non-reacting rectangular cavity.¹⁴⁹ Similar results were not observed in the non-reacting supersonic case, but owing to limitations on the extent of the measurement plane due to high background intensity such previously-documented¹¹⁰ behavior cannot be discounted.

Mean swirling strength was found to be largely uniform over the measurement plane, with the exception of a region of lower values in the upstream third of the cavity for the non-reacting supersonic case. Comparison with the center plane data showed that eddies tended to be stronger in the top plane for cases 4-6, but for case 1 anisotropy was much smaller and additionally dependent on

axial location. Axial velocity was the only quantity captured by both measurement configurations with sufficient accuracy to enable quantitative comparison, and agreement within experimental uncertainty was found for both the mean and variance.

Chapter 7

Flameholder Center Plane: Lean Blowout

7.1 Introduction

Critical to a definition of the range of flight conditions over which a dual-mode scramjet would be applicable is an understanding of the operability limits of the engine itself, as well as its behavior when these limits are approached and crossed. A number of investigators have established rich and lean blowout limits for hydrocarbon-fueled configurations,^{84,86-89,157} and correlations of these limits have been established for high-speed combustion of both hydrogen and hydrocarbons,⁹⁰ but public literature lacks detailed investigation of the blowout process. Additionally, most studies have addressed the non- or partially-premixed regimes, introducing a dependency of operability limits on the location and orientation of fuel injection.^{86,90,91} In the case of direct cavity fueling, the effect on local equivalence ratio resulting from changes in fueling rate may be amplified relative to that in the main duct, potentially leading to flameholder extinction while the remainder of the combustor is still within flammable limits.⁸⁴

The strong gradients in local equivalence ratio resulting from non-premixed fueling have also been shown to make mean flame structure a function of fueling rate.^{111,146} In contrast, Cantu et al.¹³³ found that there was no such dependency in the premixed regime, indicating its fundamentally different nature relative to non- or partially-premixed combustion. Regardless of the level of fuel-air mixing prior to the flame front, flameholding is dependent on the maintenance of a local equivalence ratio suitable for the local temperature and pressure. Accordingly, near the rich blowout (RBO) limit the cavity flameholder contains mostly fuel and combustion products, whereas near lean blowout (LBO) it contains mostly air and products.^{86,90,91,146}

LBO will result from aerodynamic changes alone if the residence time of flow within either the shear layer or cavity interior falls below the ignition delay time. In the first case, unreacted mixture in the main duct will not be exposed to the combustion products of the cavity for a sufficient duration,⁹⁰ whereas in the second case mixture that enters the cavity will exit before it is able to fully react.¹³⁷ On the other hand, LBO can result from changes in reaction chemistry alone if the equivalence ratio within the cavity falls below the flammable threshold.

Investigations of combustion behavior leading up to blowout are limited, and do not include velocimetry. Hammack et al.⁸⁰ performed 10 kHz OH PLIF in the spanwise center plane of a non-premixed ethylene-fueled scramjet, including at near-LBO conditions. The investigators found combustion was highly intermittent at this operating point, but did not examine the LBO process itself. Schultz et al.¹¹⁵ performed tunable diode laser absorption spectroscopy (TDLAS) to measure water column density and temperature during LBO of the UVaSCF in the non-premixed ethylene-

fueled scramjet mode of operation. Measurements at a 16 kHz rate showed both quantities covered 90% of the change between pre- and post-blowout values in approximately 3 ms.

Allison et al.⁶⁰ performed 1 kHz CH^* chemiluminescence imaging of the UVaSCF in the premixed ethylene-fueled configuration, finding that total CH^* intensity steadily decreased in the sense of a temporal local average (but with strong fluctuations) on approach to LBO. The spatial extent and anchoring point of the flame was seen to vary substantially shortly before LBO, indicating unsteadiness on time scales much shorter than those of the reduction in fueling rate. This finding suggests that the previously-observed variation in the lean operability limit of this flowpath⁸⁷ may be a result of the stochastic nature of the flame.

Prior investigations have not provided a characterization of the turbulent state of the cavity flameholder during LBO, leaving unexplored the role combustor aerodynamics play in the collapse of flameholding. Measurements under steady-state conditions presented in Chapter 5 demonstrated that the presence of heat release had a much greater effect on cavity aerodynamics than the configuration of the pre-combustor shock system. When considered in light of the findings of Allison et al.⁶⁰ that combustion is highly unsteady in the fractions of a second prior to LBO, the question of whether changes in flameholder aerodynamics lead or lag those in heat release remains unanswered. By presenting the first reported PIV measurements of the LBO process as well as the first LBO measurements of any type in the premixed regime, this chapter provides the first answers to this question, and in so doing satisfies the fourth scientific objective of this dissertation. Additionally, it is the first reported application of PIV to any transient process in a scramjet combustor.

As demonstrated by the time scales of the LBO process identified in earlier studies, measurements must be acquired at a rate on the order of kilohertz, thus making the high acquisition rate of PIV system 3 an enabling technology for the present work. This chapter continues with a description of the experimental approach used to capture synchronized measurements of velocity, static pressure, and fueling rate, followed by an analysis of velocimetry during the LBO process, and concludes with an assessment of the underlying mechanism and its implications for identifying imminent blowout via aerodynamic measurement.

7.2 Experimental Approach

A single test condition was used for this study, and involved a steady decrease in fueling rate from the initial state of test case 5, an equivalence ratio of 0.34 and no use of the air throttle. Since the moment at which LBO will occur cannot be predicted within the duration of a single series of PIV measurements (a limitation imposed by the capacity of camera internal memory), data were acquired in a continuously-overwriting loop, which ceased soon after blowout was achieved. A number of strategies for terminating data acquisition were considered, and ultimately it was decided that the PIV system would be manually triggered based on the distinctive acoustic signature of the LBO event. This of course does not identify the precise moment of blowout, and in order to synchronize PIV measurements with flame behavior a second Photron SA 1.1 camera was mounted opposite the first to observe broadband chemiluminescence, as seen schematically in Fig. 7.1. Accordingly, the chemiluminescence camera was not fitted with a laser line filter. The PIV camera was again operated in double-frame mode, while the combustion camera acquired single-frame images that straddled the two frames of each PIV image, allowing simultaneous characterization of the state of the flame and combustor aerodynamics. Apart from the use of the second camera, the experimental configuration was identical to that discussed in Sec. 5.2.2.

A series of measurements of fueling rate and flowpath wall static pressure were made during PIV acquisition in order to verify the achievement of desired test conditions. These data were acquired at 10 Hz, the maximum rate allowed by the measurement system, over a period of 30 seconds, which was adequate to capture the entire LBO process from the initial reduction of fueling rate to flame extinction. In order to synchronize these measurements with PIV and chemiluminescence

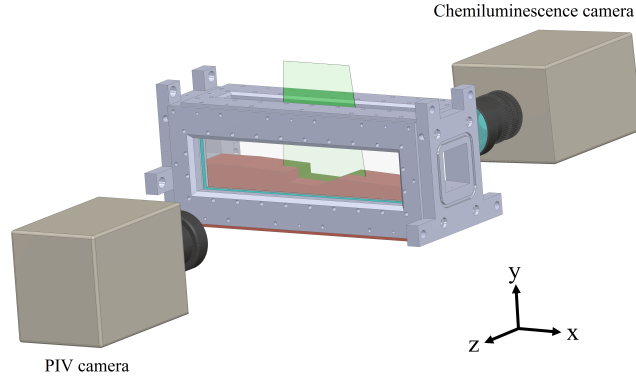


Figure 7.1: Schematic of experimental configuration for LBO measurements.

imaging, one additional channel of the pressure measurement system was devoted to recording the 5 V signal used to manually trigger the PIV system.

The imaging system was configured to acquire a continuously-overwriting series of 5000 image sets, with the trigger signal occurring on set 2000. This way, 2 seconds (at a 1 kHz rate) of data were acquired before the moment of trigger activation and 3 seconds of data after. Since both the imaging and pressure measurement systems received the trigger signal at the same moment in time, the two could be synchronized within the precision of their respective temporal resolutions.

The tracer delivery system was the same as that used in the steady-state center plane measurements (the two experiments were performed concurrently), and the flow rate of seeded air was 15 standard cubic feet per hour (SCFH), within the range of 13-15 SCFH used for the steady-state measurements (refer to Fig. 5.3 for the effects of this seeding rate on wall static pressure). Given that the post-blowout conditions were very nearly those of case 1 (the only differences resulting from the aerodynamics of fuel injection), the same PIV processing routine was applied to these data (see Sec. 5.2.2 for a full description). This applied interrogation windows that iteratively decreased in diameter from 64 to 16 pixels, with three passes at each and one at the intermediate diameter of 32 pixels. Adjacent windows were overlapped by 50%, again resulting in 0.51 mm vector spacing and 1.02 mm spatial resolution.

7.3 Results

A series of pressure scans acquired between 0.8 s prior to until 0.8 s after the moment of blowout is presented in Fig. 7.2. Since measurements were acquired at 10 Hz, it is seen that the majority of the change in the flowpath pressure distribution occurred over an approximately half-second interval. Although the measurement times of individual pressure traces are not depicted in the interest of clarity, it was found that the magnitude of pre-combustion pressure rise decreased monotonically in time, thus an arrow is included to indicate temporal progression. The time history of equivalence ratio is given in Fig. 7.3. Blowout occurred at an equivalence ratio of 0.33, within the range 0.29-0.33 found in earlier work.⁸⁷

Prior investigation of the UVaSCF in the same configuration as the present study found that pure scramjet-mode operation could not be achieved with a fully-premixed flow, since LBO would occur before the combustion-induced pressure rise moved to a stable location downstream of the cavity. Transition between dual-mode and scramjet-mode operation was possible only with the use

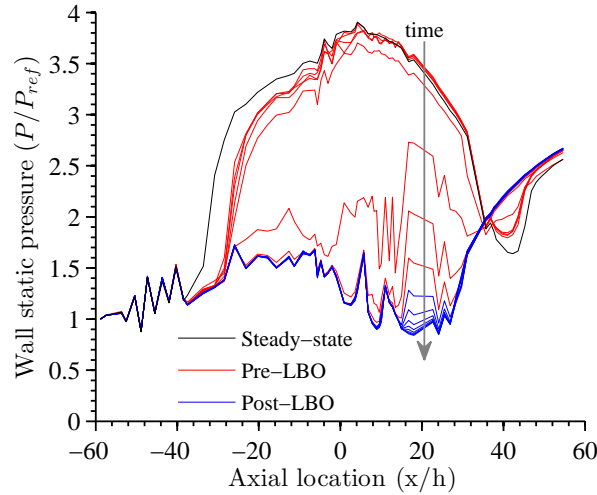


Figure 7.2: Series of 10 Hz wall static pressure measurements during LBO sequence as well as initial steady-state condition.

of supplemental fueling a short distance upstream of the cavity, resulting in a partially-premixed flow with fuel concentration highest near the cavity-side wall.⁸⁷ Considering Fig. 7.2, it is seen that the pre-combustion shock system in the present case is largely unchanged until within a half-second of blowout.

A series of combustor images acquired at 1 kHz during the LBO sequence is presented in Fig. 7.4, where the field of view extends well downstream of the cavity. LBO was defined to occur at the first frame not displaying any notable combustion luminosity, and is assigned the temporal value $t = 0$. This sequence of images displays substantial variation in the spatial extent of the flame in the moments leading up to blowout, all the while maintaining a nearly-linear flame front, in accordance with prior OH PLIF measurements.¹³³ Notable exceptions are the frames at $t = -3$ and $t = -2$ ms, where the flame fills the entire duct before diminishing in the next frame to a faint remnant concentrated near the lower flowpath wall.

In order to quantify the time scales of changes in velocity during the LBO transient, averages will be examined. Fig. 7.5 presents velocity magnitude averaged over successive 10 ms intervals. All sets prior to blowout are similar except the last, which displays increased velocity magnitude above the shear layer. The two post-blowout fields are similar, with supersonic velocities above the cavity. It is important to consider that even at a 1 kHz acquisition rate, prior to blowout the typical velocity of 500 m/s above the shear layer results in flow traversing the length of the cavity in a tenth of the time between successive measurements, so there remains an unexplored additional order of magnitude of possible temporal dynamics.

Examination of instantaneous fields is the only recourse, and these are given along with corresponding chemiluminescence images in Figs. 7.6-7.8. It is important to consider that the individual vector fields represent a measurement duration equal to the $1 \mu s$ laser pulse separation, while the combustion images were gated over the inverse sampling rate, a time period three orders of magnitude longer. Since the camera image sensor records the total luminosity received at each pixel during an exposure, these combustion images represent more of a maximum than average intensity, thus exaggerating the strength and extent of the flame. The 1 ms exposure duration imposes a temporal low-pass filter on imaged flame dynamics, thus variation at longer time scales is still captured.

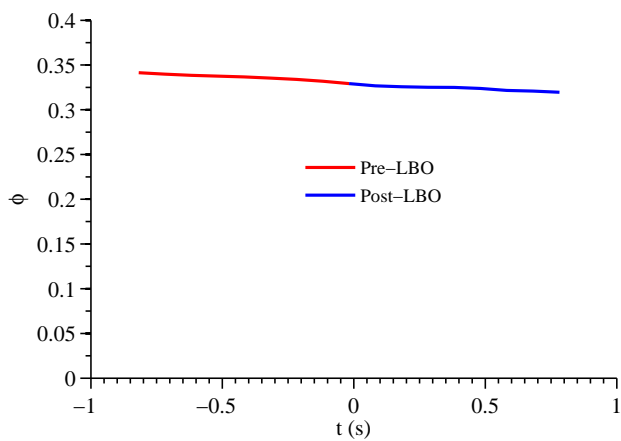


Figure 7.3: Equivalence ratio history during LBO sequence.

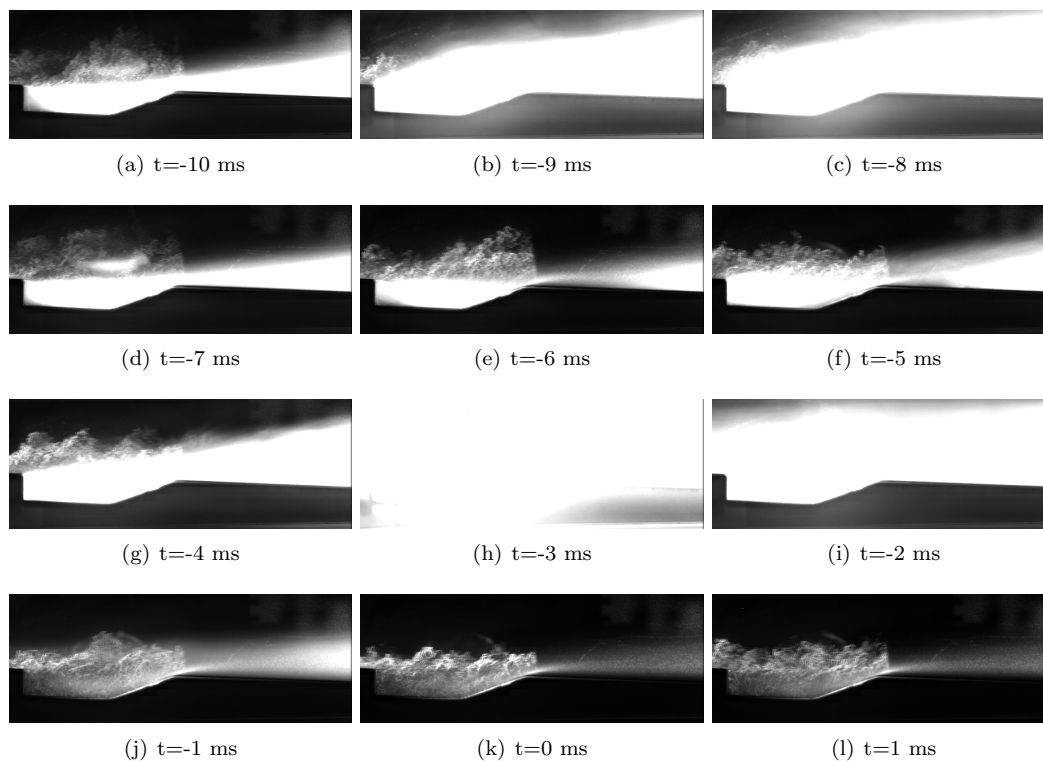


Figure 7.4: Series of images of combustion luminosity acquired at 1 kHz during the LBO transient.

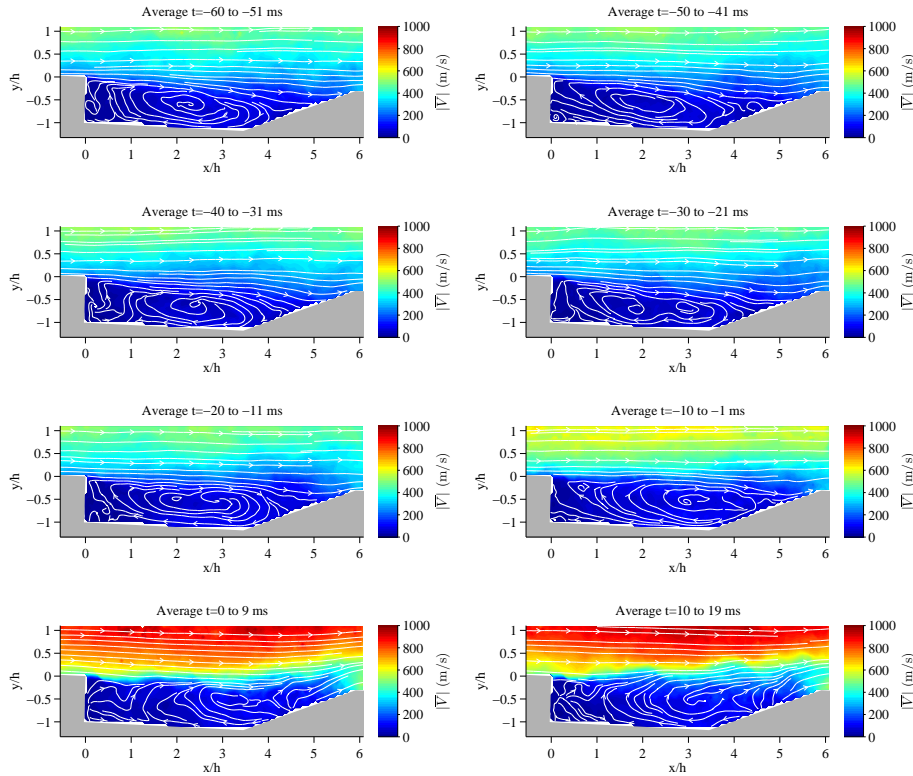


Figure 7.5: Velocity magnitude averaged over successive 10 ms intervals.

Beginning 6 ms before blowout, velocities above 700 m/s begin to intrude into the upper regions of the measurement plane, and the two acquisitions immediately prior to LBO show successively greater changes. Referring to Fig. 7.2, it is seen that the pre-combustion shock system collapsed 0.2 s prior to blowout, thus by the point these PIV fields were acquired the pre-combustor aerodynamics were supersonic (in a one-dimensional sense).

Referring to the earlier examination of steady-state aerodynamics, it was found that the presence of heat release and not the configuration of the shock system dominated cavity aerodynamics. This is in accordance with the results of Figs. 7.6-7.8, where it is seen that the majority of the flow above the cavity becomes supersonic only in the final frame prior to blowout, when combustion is only evident downstream of the cavity (cf. Fig. 7.4(j)), even though the leading edge of the shock system has already moved downstream of the cavity. Although few conclusions can be drawn from such a limited number of samples, the fact that high-speed flow enters the measurement region only well after the shock system moves downstream can be explained by sudden flame extinction: heat release would force oncoming high-velocity flow away from the cavity and broaden velocity gradients via volumetric expansion and increased viscosity,³⁹ respectively, in addition to decreasing local Mach number. Upon comparison with Fig. 7.5 it is seen that differences among post-LBO instantaneous fields represent turbulent fluctuations and not steady changes in the mean flow.

The results presented to this point suggest the mean velocity field does not appreciably change until 5 ms prior to blowout. Although limited sample sizes preclude rigorous quantification of the turbulent state at these time scales, it is worth examining velocity fluctuations to determine if their qualitative trends differ from those of the mean. Root-mean-square velocity magnitude as calculated over a 10 ms window is given in Fig. 7.9. As with mean velocity magnitude (Fig. 7.5), it is seen that substantial changes occur only in the final 10 ms prior to LBO, and are concentrated

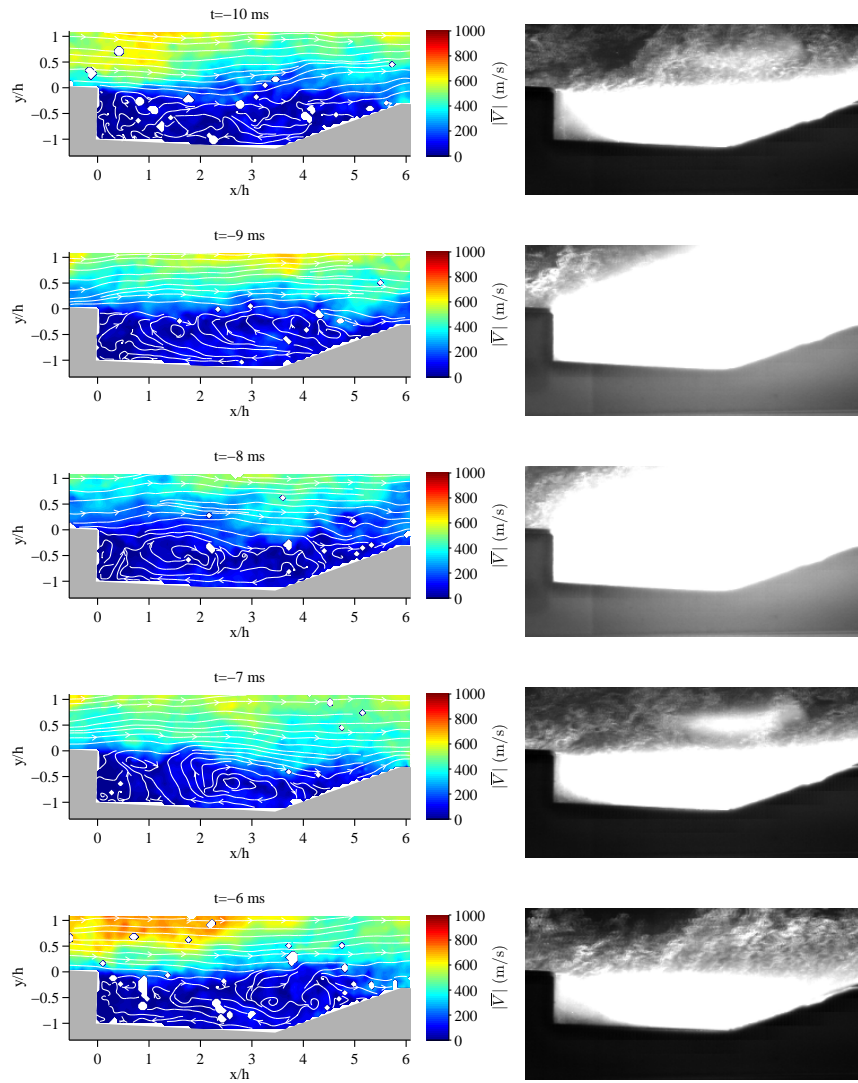


Figure 7.6: Paired instantaneous vector fields and raw images between 10 and 6 ms prior to lean blowout.

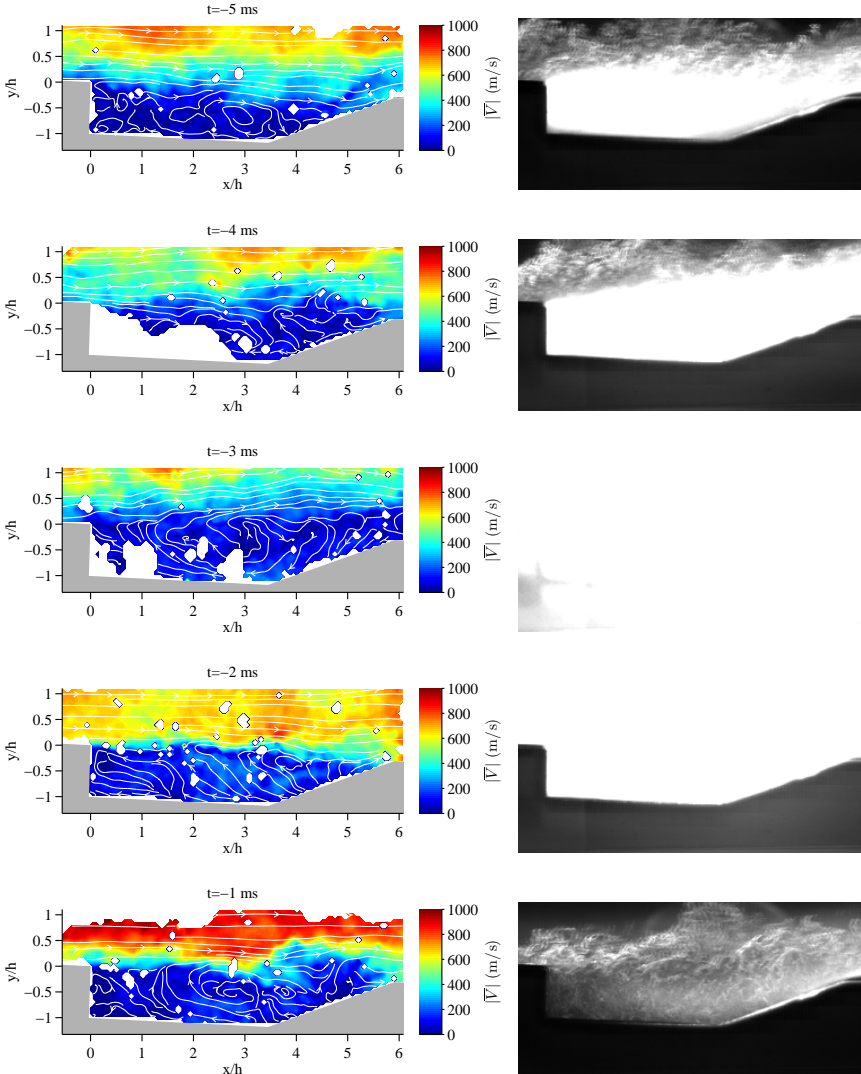


Figure 7.7: Paired instantaneous vector fields and raw images within 5 ms prior to lean blowout.

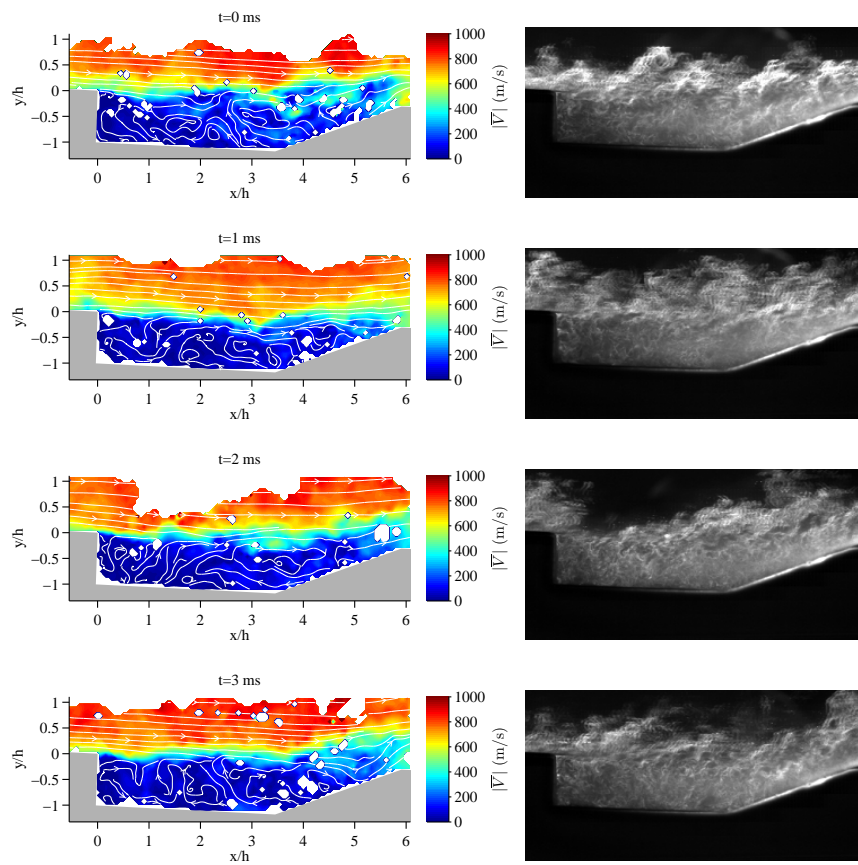


Figure 7.8: Paired instantaneous vector fields and raw images immediately after lean blowout.

above the cavity. Despite the higher mean velocity magnitudes present after blowout, fluctuations decrease above the cavity, and are instead greatest in the shear layer, as was seen earlier (Figs. 5.9 and 5.10).

Root-mean-square velocity magnitude will not be presented as calculated with fewer than ten source fields due to the resultant increase in statistical uncertainty beyond what could be reasonably construed as offering even qualitative value: according to the analysis of Benedict and Gould,¹⁰⁷ uncertainty increases from 44% to 62% when sample size decreases from 10 to 5 (see Eq. (3.6)).

It has been shown that cavity aerodynamics, in the sense of mean and fluctuating velocity magnitudes, change significantly only within the final 5 ms prior to LBO. As seen in the series of pressure scans acquired at 10 Hz (Fig. 7.2), the overall flowpath aerodynamic state changes over a time span greater by two orders of magnitude. Additionally, the time scale of reduction in fueling rate (Fig. 7.3) is much greater than that of the collapse of the pre-combustion shock system. These results indicate that it is not a change in cavity aerodynamics resulting from the slow retreat of the shock system prior to collapse that disrupts the mechanism of flameholding analyzed in Chapter 5. Rather, it is the sudden dissolution of the reaction process and attendant cessation of heat release that eliminates the shock system and transforms cavity aerodynamics.

This process is explained by the local equivalence ratio in the cavity falling below a flammable threshold. Given the location of the flame within the cavity (cf. Fig. 5.5), little of the cavity mixture will be unchanged in composition relative to that entering the combustor. Rather, reactions will have consumed fuel and oxygen and added combustion products, thus maintaining the local reactant concentration below that of the main duct. It is thus reasonable to expect that during a reduction in fueling rate, the cavity would be the first of the two to fall below flammability limits. This would account for the robust main-duct combustion seen immediately prior to blowout (Fig. 7.4), which would cease only when deprived of a continuous source of heat and radicals from the cavity.

As discussed previously, the definition of flowpath operability limits is critical to the development of flight vehicles, since in some cases it may be desirable to operate as close to a limit as possible. For example, during transition from dual-mode to scramjet-modes of operation the flowpath may operate near its lean limit,⁸⁷ introducing a requirement for a means to detect imminent blowout so that fuel delivery may be adjusted accordingly. These results indicate velocimetry of at least 1 kHz rate could allow operation closer to the LBO point, assuming fuel delivery could be controlled on comparable time scales. In particular, continuous measurement of RMS velocity magnitude immediately above the cavity on a 10 ms sliding interval would provide clear identification of imminent LBO, as seen in Fig. 7.9. 1 kHz TDLAS has been demonstrated in the inlet of a flight test vehicle, enabling measurement of velocity, temperature, and water concentration.¹⁵⁸ The technique has additionally been applied to the combustor of a direct-connect scramjet ground test rig,^{114, 115, 159, 160} indicating kHz-rate in-flight measurements of combustor velocity are within reach of current technology.

Alternatively, LBO could be predicted by 10 Hz static pressure measurements, well within the 930 Hz bandwidth that has been demonstrated in flight.⁹⁸ The magnitude of pre-combustion pressure rise is indicative of total heat release and thus thrust that would be produced by a DMSJ installed in a flight vehicle.¹ Since thrust would have already decreased substantially prior to the moment of blowout (see Fig. 7.2), the choice of whether pressure or velocity measurement is used to drive a fuel control algorithm is dependent on required thrust. Accordingly, if a specific thrust level is desired then pressure measurement may be more suitable, but velocimetry may be more appropriate if the goal is to maintain operation at the lowest allowable fueling rate.

7.4 Conclusions

Particle image velocimetry was performed during the lean blowout transient of a premixed ethylene-fueled dual-mode scramjet, providing the first reported velocity measurements of blowout as well

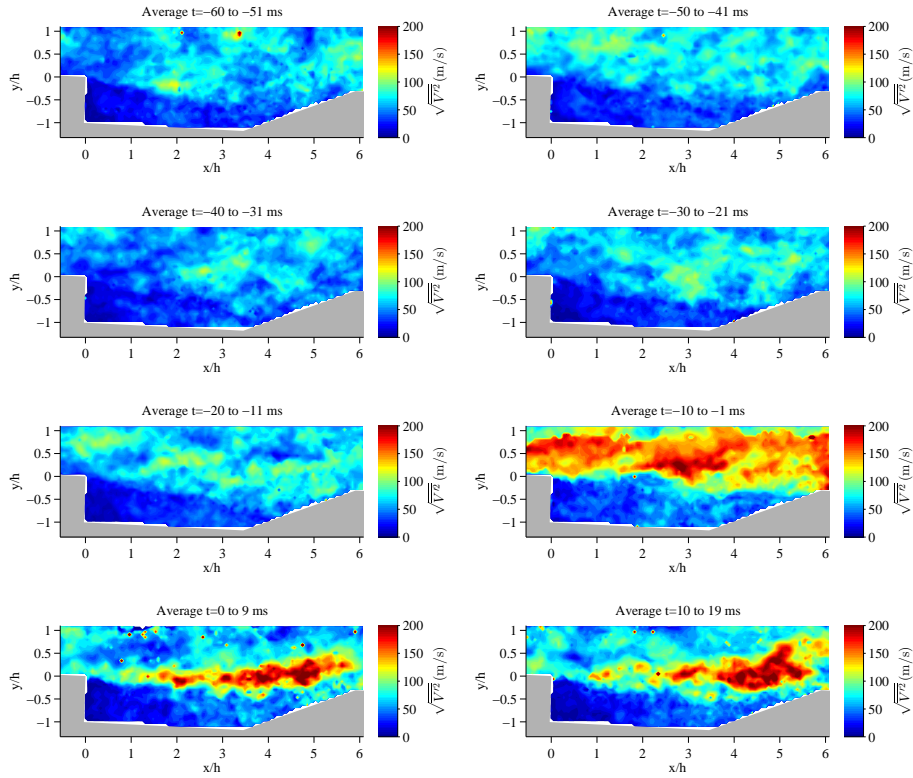


Figure 7.9: Magnitude of root-mean-square velocity calculated over successive 10 ms intervals.

as the first measurements of any kind during blowout in the premixed regime. The 1 kHz sampling rate revealed that changes in cavity flameholder aerodynamics prior to blowout occurred over a time span approximately two orders of magnitude smaller than those in the structure of the pre-combustion shock system. These results suggest that blowout occurred not because of a change in cavity aerodynamics, but rather that the reactant mixture in the cavity fell below flammable limits, removing the means by which main-duct combustion could be sustained.

It was found that the aerodynamic state of the cavity changed only within 5 ms prior to blowout, and was characterized by the rapid increase of velocity magnitude at the interface with the main duct. These measurements, when considered in light of earlier steady-state results, indicate that the termination of heat release permitted supersonic flow to approach the cavity, increasing turbulent exchange as a result. kHz-rate velocimetry techniques developed to a state of near-term applicability to flight vehicles could thus be used to detect imminent lean blowout and allow fueling to be adjusted accordingly, enabling operation closer to flowpath limits.

Chapter 8

Conclusions

8.1 Summary of Findings

Particle image velocimetry (PIV) was used to characterize the cavity flameholder of two configurations of a direct-connect dual-mode scramjet, examining conditions corresponding to notional design points as well as those close to and crossing operability limits. Prior measurements of flameholder aerodynamics had not attempted to replicate the system of shock waves and expansion fans generated by a flight vehicle inlet. The configuration of this distortion would be expected to change with flight Mach number and angle of attack, resulting in substantial departures of typical operating conditions from those of most ground test environments. Additionally, published data lacked characterization of flameholder aerodynamics as directly influenced by heat release and not instead coupled with fuel-air mixing, nor had velocity measurements been presented during the lean-blowout transient. This study provides the first such analyses, establishing a more detailed definition of flameholder aerodynamics across a range of operating conditions.

A full-span wedge was used to produce a single oblique shock wave and expansion fan in the combustor of a direct-connect scramjet flowpath, allowing the influence on the cavity flameholder of replicated inlet distortion and its interaction with crossflow jet injection to be examined. PIV was applied to a plane along the spanwise centerline of the flowpath, enabling the cavity as well as an adjacent region of the main duct to be examined. Shock impingement upstream of the cavity was found to compress the recirculation region and consequently increase the length of the aft face exposed to non-recirculating flow, which would limit entrainment of fuel injected from this location to an extent dependent on the spanwise uniformity of the flow. Direct impingement of the shock on the cavity increased the area of recirculating flow, an effect that was amplified when upstream jet injection was active.

The shock was found to increase unsteadiness throughout the shear layer separating cavity recirculation from the remainder of the combustor, and in particular at the locations of its formation and reattachment. Jet injection was found to thicken the shear layer in all distortion configurations and smooth peaks in root-mean-square velocity, whereby magnitudes were reduced at their maxima but generally greater across the measurement plane, an effect less pronounced with replicated inlet distortion than without. These results, which were the first of their kind to be published, demonstrated that the aerodynamics of a scramjet in flight may differ sharply from a conceptual design point free of compression and expansion waves propagating downstream from the engine inlet.

These experiments and subsequent attempts at measurements in a different scramjet flowpath revealed limitations of conventional velocimetry tracers in confined high-enthalpy flows. An investigation into alternative tracers led to the identification of graphite flakes as being compatible with flowpath windows at all operating conditions. It was shown that these particles survived passage

through the reaction zone of the cavity flameholder, and subsequent measurements were the first to use this tracer type in a high-speed flow or downstream of a flame front. Aerodynamic and thermophoretic slip were quantified with analytical models and found to make a contribution to overall experimental error several orders of magnitude smaller than those due to finite sample size and the PIV calibration process.

PIV was applied to the spanwise center plane of the cavity flameholder of a premixed dual-mode scramjet, encompassing six notional design points at both reacting and non-reacting conditions. These results were the first reported in either the dual-mode or premixed regimes, and the use of an air throttle allowed the effects of heat release to be decoupled from changes to the pre-combustion shock system. It was found that the mean velocity field was dominated by the presence and length of this shock system, whereas turbulent velocities were most dependent on whether or not heat release occurred and not its magnitude or shock system length.

Similarly, integral length scales at a point located above the cavity leading edge were nearly unaffected by a change of fueling rate from near one end of the operability range to the other. This finding suggests that flameholder turbulent aerodynamics cannot be recreated if combustion is neglected, even if a device such as an air throttle is used to replicate mean velocities or the pre-combustion pressure rise. As a result, experimental or numerical replications of a particular scramjet operating point must incorporate combustion for the full on-design condition to be captured.

Knowledge of the turbulent state of the cavity flameholder is critical to understanding the process by which the main-duct reactions that constitute the majority of heat release in a scramjet are maintained. It was shown that turbulence intensity as averaged over a line extending from the cavity leading edge into the main duct was positively correlated with prior measurements of flame spreading angle, providing experimental verification of the relationship between turbulent flame speed and the mean configuration of the flame front. The variances and covariance of orthogonal velocity components were compared with prior measurements of radical species to demonstrate how main-duct combustion is piloted by the turbulent transport through the shear layer of products generated in the cavity interior.

Stereoscopic PIV (SPIV) was applied to the plane defining the boundary between the cavity and main duct of the combustor. This is the first reported application of SPIV to a scramjet cavity, as well as the first to perform PIV measurements in a plane of the cavity other than that at the spanwise center, allowing investigation of both the spanwise variation of velocity as well as its spanwise component. Turbulent velocities were found to be highest near the location of shear layer reattachment at the cavity aft face, in accordance with prior studies and the center plane measurements of the present work. Spanwise variation was found to be minor for all velocity statistics considered, with the most notable feature being regions of higher in-plane turbulence intensity near the outer edges of the cavity in the reacting-flow cases.

The SPIV measurements were challenged by a low signal-to-noise ratio, non-optimal camera viewing angles, and strong velocity gradients within the thickness of the laser sheet. These precluded meaningful analysis of the component of velocity normal to the cavity floor, as determined by a direct analysis of correlation uncertainty in the vector calculation process, but comparison of the other component of velocity captured by both this and the center plane measurements demonstrated agreement to within the overall experimental uncertainty.

To explore flameholder aerodynamics near the limits of steady-state operability, PIV measurements were made in the spanwise center plane during the lean blowout transient of the same flowpath, providing the first reported velocimetry of this process as well as the first measurements of any type in the premixed regime. It was found that flameholder aerodynamics were nearly unchanged until approximately 5 ms prior to blowout, whereas the pre-combustion shock system receded on a time scale two orders of magnitude longer. Taken together with the steady-state measurements showing that the aerodynamic state of the cavity was largely unaffected by changes in heat release or shock system length once combustion was established, this finding suggested that the loss of a combustible fuel-air mixture ratio in the cavity led to the sudden collapse of reactions

throughout the combustor, rather than an alteration of the turbulent exchange between the cavity and main duct. The time scales of changes in the flameholder velocity field indicative of imminent lean blowout are within the capabilities of flight-proven optical diagnostics, and the inclusion of such a system in a flight vehicle would enable operation of the scramjet flowpath closer to design limits.

8.2 Recommendations for Future Work

It is recommended that future investigations examine the relationship between reaction chemistry and flameholder aerodynamics in greater detail. Though much was learned from a comparison of ensemble statistics of separately-acquired velocimetry and imaging of combustion radicals, simultaneous measurements⁷⁵ would provide greater insight into the process by which products of cavity combustion pilot main-duct reactions, as well as how this process breaks down as the lean operability limit is crossed. Comparison of the mean flow-through time above the cavity with the PIV acquisition rate suggests an additional order of magnitude of temporal dynamics is available for study, making higher-rate PIV measurements desirable for quantifying this and other transient phenomena.

The limitations on spatial resolution of SPIV became apparent in measurements of the cavity-main duct interface, where spatial averaging in the through-sheet direction limited the value of higher in-plane resolution. This was compounded by large camera angles relative to the measurement plane normal, resulting in rhombohedral interrogation volumes that captured a larger spanwise extent of the flow than the width of their bases. Such line-of-sight bias is removed by tomographic PIV (TPIV), which permits equal spatial resolution in all three dimensions of a measurement volume. This feature is particularly important to measurements that seek to approach the Kolmogorov scales, since in SPIV a minimum laser sheet thickness must be maintained to minimize out-of-plane loss of tracers between frames of an image, even if camera resolution and tracer density permit much higher in-plane spatial resolution.

Reported hydroxyl-tagging velocimetry^{100,137,148} of scramjet cavity flameholders has suggested spanwise flow is stronger at locations closer to the floor than the interface with the main duct, a result qualitatively suggested by the greater metal oxide tracer deposition on combustor windows seen in this study, as well as the expectation that flow over the top of the cavity would be dominated by the strong axial velocity component. It is recommended that PIV be applied in floor-parallel planes within the cavity, once the optical challenges encountered in the present experiments are addressed. A better solution would be the implementation of TPIV, so that not only would all three components of velocity be resolved, but the six independent components of the velocity gradient tensor as well, thereby aiding the quantification of the turbulent state of the flameholder.

References

- [1] Heiser, W. H. and Pratt, D. T., *Hypersonic Airbreathing Propulsion*, American Institute of Aeronautics and Astronautics, Washington, DC, 1994.
- [2] Avery, W. H., “Twenty-Five Years of Ramjet Development,” *Journal of Jet Propulsion*, Vol. 25, No. 11, 1955, pp. 604–614. doi:10.2514/8.6833.
- [3] Sabel’nikov, V. A. and Penzin, V. I., “Scramjet Research and Development in Russia,” *Scramjet Propulsion*, edited by E. T. Curran and S. N. B. Murthy, American Institute of Aeronautics and Astronautics, Reston, VA, 2000, pp. 223–367.
- [4] Segal, C., *The Scramjet Engine: Processes and Characteristics*, Cambridge University Press, New York, 2009.
- [5] Daum, N., “The Griffon Aircraft and the Future of the Turbo-Ram-Jet Combination in the Propulsion of Supersonic Aeroplanes,” *Journal of the Royal Aeronautical Society*, Vol. 63, No. 582, 1959, pp. 327–339.
- [6] Jenkins, D. R., Landis, T., and Miller, J., “American X-Vehicles: An Inventory, X-1 to X-50,” NASA SP-2003-4531, June 2003.
- [7] Anderson, J. D., *Hypersonic and High-Temperature Gas Dynamics*, 2nd ed., American Institute of Aeronautics and Astronautics, Reston, VA, 2006.
- [8] Curran, E. T., “Scramjet Engines: The First Forty Years,” *Journal of Propulsion and Power*, Vol. 17, No. 6, 2001, pp. 1138–1148. doi:10.2514/2.5875.
- [9] Andrews, E. H., “Scramjet Development and Testing in the United States,” AIAA Paper 2001-1927, April 2001. doi:10.2514/6.2001-1927.
- [10] Adelgren, R. G., Elliott, G. S., Knight, D. D., Zheltovodov, A. A., and Beutner, T. J., “Energy Deposition in Supersonic Flows,” AIAA Paper 2001-885, Jan. 2001. doi:10.2514/6.2001-885.
- [11] Smart, M. K., Hass, N. E., and Paull, A., “Flight Data Analysis of the HyShot 2 Scramjet Flight Experiment,” *AIAA Journal*, Vol. 44, No. 10, 2006, pp. 2366–2375. doi:10.2514/1.20661.
- [12] McClinton, C. R., “X-43 Scramjet Power Breaks the Hypersonic Barrier: Dryden Lectureship in Research for 2006,” AIAA Paper 2006-1, Jan. 2006. doi:10.2514/6.2006-1.
- [13] Hank, J. M., Murphy, J. S., and Mutzman, R. C., “The X-51A Scramjet Engine Flight Demonstration Program,” AIAA Paper 2008-2540, April 2008. doi:10.2514/6.2008-2540.
- [14] Maurice, L., Edwards, T., and Griffiths, J., “Liquid Hydrocarbon Fuels for Hypersonic Propulsion,” *Scramjet Propulsion*, edited by E. T. Curran and S. N. B. Murthy, American Institute of Aeronautics and Astronautics, Reston, VA, 2000, pp. 757–822.

- [15] Goyne, C. P., McDaniel, J. C., Krauss, R. H., and Day, S., "Velocity Measurement in a Dual-mode Supersonic Combustor using Particle Image Velocimetry," AIAA Paper 2001-1761, April 2001. doi:10.2514/6.2001-1761.
- [16] Ben-Yakar, A. and Hanson, R. K., "Cavity Flame-Holders for Ignition and Flame Stabilization in Scramjets: An Overview," *Journal of Propulsion and Power*, Vol. 17, No. 4, 2001, pp. 869–877. doi:10.2514/2.5818.
- [17] Gruber, M. R., Baurle, R. A., Mathur, T., and Hsu, K.-Y., "Fundamental Studies of Cavity-Based Flameholder Concepts for Supersonic Combustors," *Journal of Propulsion and Power*, Vol. 17, No. 1, 2001, pp. 146–153. doi:10.2514/2.5720.
- [18] Gruber, M. R., Donbar, J. M., Carter, C. D., and Hsu, K.-Y., "Mixing and Combustion Studies Using Cavity-Based Flameholders in a Supersonic Flow," *Journal of Propulsion and Power*, Vol. 20, No. 5, 2004, pp. 769–778. doi:10.2514/1.5360.
- [19] Steva, T. B., Goyne, C. P., Rockwell, R. D., Cresci, D., and Osborne, J. W., "Comparison of a Direct-Connect and Freejet Dual-Mode Scramjet," *Journal of Propulsion and Power*, Vol. 31, No. 5, 2015, pp. 1380–1392. doi:10.2514/1.B35221.
- [20] Doherty, L. J., Smart, M. K., and Mee, D. J., "Experimental Testing of an Airframe-Integrated Three-Dimensional Scramjet at Mach 10," *AIAA Journal*, Vol. 53, No. 11, 2014, pp. 3196–3207. doi:10.2514/1.J053785.
- [21] Tam, C.-J., Hsu, K.-Y., Hagenmaier, M. A., and Raffoul, C., "Studies of Inlet Distortion in a Direct-Connect Axisymmetric Scramjet Isolator," *Journal of Propulsion and Power*, Vol. 29, No. 6, 2013, pp. 1382–1390. doi:10.2514/1.B34944.
- [22] Hagenmaier, M. A., Eklund, D. R., and Milligan, R. T., "Improved Simulation of Inflow Distortion for Direct-Connect Scramjet Studies," AIAA Paper 2011-233, Jan. 2011. doi:10.2514/6.2011-233.
- [23] Krauss, R. H. and McDaniel, J. C., "A Clean Air Continuous Flow Propulsion Facility," AIAA Paper 1992-3912, July 1992. doi:10.2514/6.1992-3912.
- [24] Gruber, M. R. and Nejad, A., "New Supersonic Combustion Research Facility," *Journal of Propulsion and Power*, Vol. 11, No. 5, 1995, pp. 1080–1083. doi:10.2514/3.23940.
- [25] Huh, H., *An Experimental Study of Supersonic Hydrogen-Air Flames for Scramjet Applications*, Ph.D. thesis, University of Michigan, 1996.
- [26] Campioli, T. L., Maddalena, L., and Schetz, J. A., "Studies of Shock Wave/Transverse Injection Interaction on Supersonic Mixing Processes," AIAA Paper 2006-8135, Nov. 2006. doi:10.2514/6.2006-8135.
- [27] Gruber, M. R., Hagenmaier, M. A., and Mathur, T., "Simulating Inlet Distortion Effects in a Direct-Connect Scramjet Combustor," AIAA Paper 2006-4680, July 2006. doi:10.2514/6.2006-4680.
- [28] Ogorodnikov, D. A., Vinogradov, V. A., Shikhman, Y. M., and Strokin, V. N., "Russian Research on Experimental Hydrogen-Fueled Dual-Mode Scramjet: Conception and Preflight Tests," *Journal of Propulsion and Power*, Vol. 17, No. 5, 2001, pp. 1041–1048. doi:10.2514/2.5842.

- [29] Laurence, S. J., Lieber, D., Martinez Schramm, J., Hannemann, K., and Larsson, J., “Incipient thermal choking and stable shock-train formation in the heat-release region of a scramjet combustor. Part I: Shock-tunnel experiments,” *Combustion and Flame*, Vol. 162, No. 4, 2015, pp. 921–931. doi:10.1016/j.combustflame.2014.09.016.
- [30] Kondo, A., Sakaue, S., and Arai, T., “Measurement Method of Mass Flux and Concentration in Supersonic Mixing by Hot-Wire Anemometry,” *International Journal of Emerging Multidisciplinary Fluid Sciences*, Vol. 2, No. 1, 2010, pp. 15–26.
- [31] Arai, T., Sakaue, S., Morisaki, T., Kondo, A., Hiejima, T., and Nishioka, M., “Supersonic Streamwise Vortices Breakdown in Scramjet Combustor,” AIAA Paper 2006-8025, Nov. 2006. doi:10.2514/6.2006-8025.
- [32] Petrie, H. L., Samimy, M., and Addy, A. L., “Compressible Separated Flows,” *AIAA Journal*, Vol. 24, No. 12, 1986, pp. 1971–1978. doi:10.2514/3.9555.
- [33] McDaniel, J. C., Fletcher, D. G., Hartfield, R. J., and Hollo, S. D., “Transverse Injection into Mach 2 Flow Behind a Rearward-Facing Step: A 3-D, Compressible Flow Test Case for Hypersonic Combustor CFD Validation,” AIAA Paper 1991-5071, Dec. 1991. doi:10.2514/6.1991-5071.
- [34] Elliott, G. S., Mosedale, A., Gruber, M. R., Nejad, A. S., and Carter, C. D., “The Study of a Transverse Jet in a Supersonic Cross-Flow Using Molecular Filter Based Diagnostics,” AIAA Paper 1997-2999, July 1997. doi:10.2514/6.1997-2999.
- [35] Das, R., Kim, H.-D., and Kurian, J., “Experimental Study of Supersonic Entrainment Using a Cavity,” *Journal of Propulsion and Power*, Vol. 30, No. 5, 2014, pp. 1143–1151. doi:10.2514/1.B35047.
- [36] Scheel, F., “PIV Measurement of a 3-Dimensional Reacting Flow in a Scramjet Combustion Chamber,” AIAA Paper 2004-1038, Jan. 2004. doi:10.2514/6.2004-1038.
- [37] Goyne, C. P., Rodriguez, C. G., Krauss, R. H., McDaniel, J. C., and McClinton, C. R., “Experimental and Numerical Study of a Dual-Mode Scramjet Combustor,” *Journal of Propulsion and Power*, Vol. 22, No. 3, 2006, pp. 481–489. doi:10.2514/1.13215.
- [38] Smith, C. T. and Goyne, C. P., “Application of Stereoscopic Particle Image Velocimetry to a Dual-Mode Scramjet,” *Journal of Propulsion and Power*, Vol. 27, No. 6, 2011, pp. 1178–1185. doi:10.2514/1.B34106.
- [39] Tuttle, S. G., Carter, C. D., and Hsu, K.-Y., “Particle Image Velocimetry in a Nonreacting and Reacting High-Speed Cavity,” *Journal of Propulsion and Power*, Vol. 30, No. 3, 2014, pp. 576–591. doi:10.2514/1.B34974.
- [40] Peltier, S. J., Kirik, J. W., Goyne, C. P., and Carter, C. D., “Response of a Ramped Cavity to Shock-Induced Distortions in a Mach 3 Freestream,” AIAA Paper 2013-3699, July 2013. doi:10.2514/6.2013-3699.
- [41] Rice, B. E., Goyne, C. P., McDaniel, J. C., and Rockwell, R. D., “Characterization of a Dual-Mode Scramjet via Stereoscopic Particle Image Velocimetry,” AIAA Paper 2014-0986, Jan. 2014. doi:10.2514/6.2014-0986.
- [42] Kirik, J. W., Goyne, C. P., Peltier, S. J., Carter, C. D., and Hagenmaier, M. A., “Velocimetry Measurements of a Scramjet Cavity Flameholder with Inlet Distortion,” *Journal of Propulsion and Power*, Vol. 30, No. 6, 2014, pp. 1568–1576. doi:10.2514/1.B35195.

- [43] Rockwell, R. D., Goyne, C. P., Rice, B. E., Kouchi, T., McDaniel, J. C., and Edwards, J. R., “Collaborative Experimental and Computational Study of a Dual-Mode Scramjet Combustor,” *Journal of Propulsion and Power*, Vol. 30, No. 3, 2014, pp. 530–538. doi:10.2514/1.B35021.
- [44] Rice, B. E., Goyne, C. P., and McDaniel, J. C., “Seeding Bias in Particle Image Velocimetry Applied to Dual-Mode Scramjet,” *Journal of Propulsion and Power*, Vol. 31, No. 5, 2015, pp. 1393–1403. doi:10.2514/1.B35443.
- [45] Peltier, S. J. and Carter, C. D., “Response of a Mach 3 Cavity Flameholder to a Shock-Induced Distortion,” AIAA Paper 2015-0883, Jan. 2015. doi:10.2514/6.2015-0883.
- [46] Westerweel, J., Elsinga, G. E., and Adrian, R. J., “Particle Image Velocimetry for Complex and Turbulent Flows,” *Annual Review of Fluid Mechanics*, Vol. 45, 2013, pp. 409–436. doi:10.1146/annurev-fluid-120710-101204.
- [47] Samimy, M. and Wernet, M. P., “Review of Planar Multiple-Component Velocimetry in High-Speed Flows,” *AIAA Journal*, Vol. 38, No. 4, 2000, pp. 553–574. doi:10.2514/2.1004.
- [48] Tennekes, H. and Lumley, J. L., *A First Course in Turbulence*, MIT Press, Cambridge, MA, 1972.
- [49] Thurow, B., Jiang, N., and Lempert, W., “Review of ultra-high repetition rate laser diagnostics for fluid dynamic measurements,” *Measurement Science and Technology*, Vol. 24, No. 1, 2013. doi:10.1088/0957-0233/24/1/012002.
- [50] Filatyev, S. A., Driscoll, J. F., Carter, C. D., and Donbar, J. M., “Measured properties of turbulent premixed flames for model assessment, including burning velocities, stretch rates, and surface densities,” *Combustion and Flame*, Vol. 141, No. 1-2, 2005, pp. 1–21. doi:10.1016/j.combustflame.2004.07.010.
- [51] Rice, B. E., *Characterization of a Dual-Mode Scramjet via Stereoscopic Particle Image Velocimetry*, Ph.D. thesis, University of Virginia, 2014.
- [52] Ramesh, K. K., Edwards, J. R., Chelliah, H. K., Goyne, C. P., McDaniel, J. C., Rockwell, R. D., Kirik, J. W., Cutler, A. D., and Danehy, P. M., “Large Eddy Simulation of High-Speed, Premixed Ethylene Combustion,” AIAA Paper 2015-0356, Jan. 2015. doi:10.2514/6.2015-0356.
- [53] Gamba, M. and Clemens, N. T., “Requirements, Capabilities and Accuracy of Time-Resolved PIV in Turbulent Reacting Flows,” AIAA Paper 2011-362, Jan. 2011. doi:10.2514/6.2011-362.
- [54] Sutton, J. A., “Highly Turbulent Combustion: Scientific Challenges, Measurement Requirements, and Diagnostic Needs,” AFOSR-ARO Basic Combustion Review, Dayton, OH, June 2013.
- [55] Steinberg, A. M., Boxx, I., Arndt, C. M., Frank, J. H., and Meier, W., “Experimental study of flame-hole reignition mechanisms in a turbulent non-premixed jet flame using sustained multi-kHz PIV and crossed-plane OH PLIF,” *Proceedings of the Combustion Institute*, Vol. 33, No. 1, 2011, pp. 1663–1672. doi:10.1016/j.proci.2010.06.134.
- [56] Steinberg, A. M., Driscoll, J. F., and Ceccio, S. L., “Three-dimensional temporally resolved measurements of turbulence/flame interactions using orthogonal-plane cinema-stereoscopic PIV,” *Experiments in Fluids*, Vol. 47, No. 3, 2009, pp. 527–547. doi:10.1007/s00348-009-0677-7.

- [57] Fotia, M. L. and Driscoll, J. F., “Ram-Scram Transition and Flame/Shock-Train Interactions in a Model Scramjet Experiment,” *Journal of Propulsion and Power*, Vol. 29, No. 1, 2013, pp. 261–273. doi:10.2514/1.B34486.
- [58] Wang, Z., Wang, H., and Sun, M., “Review of cavity-stabilized combustion for scramjet applications,” *Proceedings of the Institution of Mechanical Engineers, Part G: Journal of Aerospace Engineering*, Vol. 228, No. 14, 2014, pp. 2718–2735. doi:10.1177/0954410014521172.
- [59] Lin, K.-C., Jackson, K. R., Behdadnia, R., Jackson, T., Ma, F., and Yang, V., “Acoustic Characterization of an Ethylene-Fueled Scramjet Combustor with a Cavity Flameholder,” *Journal of Propulsion and Power*, Vol. 26, No. 6, 2010, pp. 1161–1169. doi:10.2514/1.43338.
- [60] Allison, P. M., Frederickson, K., Lempert, W. R., Sutton, J. A., Kirik, J. W., Rockwell, R. D., and Goyne, C. P., “Investigation of Flame Structure and Combustion Dynamics using CH₂O PLIF and High-Speed CH* Chemiluminescence in a Premixed Dual-Mode Scramjet Combustor,” AIAA Paper 2016-441, Jan. 2016. doi:10.2514/6.2016-0441.
- [61] Sick, V., “High speed imaging in fundamental and applied combustion research,” *Proceedings of the Combustion Institute*, Vol. 34, No. 2, 2013, pp. 3509–3530. doi:10.1016/j.proci.2012.08.012.
- [62] Driscoll, J. F., “Turbulent premixed combustion: Flamelet structure and its effect on turbulent burning velocities,” *Progress in Energy and Combustion Science*, Vol. 34, No. 1, 2008, pp. 91–134. doi:10.1016/j.pecs.2007.04.002.
- [63] Steinberg, A. M., Driscoll, J. F., and Ceccio, S. L., “Measurements of turbulent premixed flame dynamics using cinema stereoscopic PIV,” *Experiments in Fluids*, Vol. 44, No. 6, 2008, pp. 985–999. doi:10.1007/s00348-007-0458-0.
- [64] Fajardo, C. and Sick, V., “Development of a high-speed UV particle image velocimetry technique and application for measurements in internal combustion engines,” *Experiments in Fluids*, Vol. 46, No. 1, 2008, pp. 43–53. doi:10.1007/s00348-008-0535-z.
- [65] Barbosa, S., Scouffaire, P., and Ducruix, S., “Time resolved flowfield, flame structure and acoustic characterization of a staged multi-injection burner,” *Proceedings of the Combustion Institute*, Vol. 32, No. 2, 2009, pp. 2965–2972. doi:10.1016/j.proci.2008.06.139.
- [66] Coriton, B. and Frank, J. H., “High-speed tomographic PIV measurements of strain rate intermittency and clustering in turbulent partially-premixed jet flames,” *Proceedings of the Combustion Institute*, Vol. 35, No. 2, 2015, pp. 1243–1250. doi:10.1016/j.proci.2014.06.045.
- [67] Konle, M., Kiesewetter, F., and Sattelmayer, T., “Simultaneous high repetition rate PIV-LIF-measurements of CIVB driven flashback,” *Experiments in Fluids*, Vol. 44, No. 4, 2008, pp. 529–538. doi:10.1007/s00348-007-0411-2.
- [68] Boxx, I., Stöhr, M., Carter, C. D., and Meier, W., “Sustained multi-kHz flamefront and 3-component velocity-field measurements for the study of turbulent flames,” *Applied Physics B: Lasers and Optics*, Vol. 95, No. 1, 2009, pp. 23–29. doi:10.1007/s00340-009-3420-4.
- [69] Boxx, I., Heeger, C., Gordon, R., Böhm, B., Aigner, M., Dreizler, A., and Meier, W., “Simultaneous three-component PIV/OH-PLIF measurements of a turbulent lifted, C₃H₈-Argon jet diffusion flame at 1.5 kHz repetition rate,” *Proceedings of the Combustion Institute*, Vol. 32, No. 1, 2009, pp. 905–912. doi:10.1016/j.proci.2008.06.023.

- [70] Heeger, C., Böhm, B., Ahmed, S. F., Gordon, R., Boxx, I., Meier, W., Dreizler, A., and Mastorakos, E., “Statistics of relative and absolute velocities of turbulent non-premixed edge flames following spark ignition,” *Proceedings of the Combustion Institute*, Vol. 32, No. 2, 2009, pp. 2957–2964. doi:10.1016/j.proci.2008.07.006.
- [71] Konle, M. and Sattelmayer, T., “Interaction of heat release and vortex breakdown during flame flashback driven by combustion induced vortex breakdown,” *Experiments in Fluids*, Vol. 47, No. 4-5, 2009, pp. 627–635. doi:10.1007/s00348-009-0679-5.
- [72] Heeger, C., Gordon, R. L., Tummers, M. J., Sattelmayer, T., and Dreizler, A., “Experimental analysis of flashback in lean premixed swirling flames: upstream flame propagation,” *Experiments in Fluids*, Vol. 49, No. 4, 2010, pp. 853–863. doi:10.1007/s00348-010-0886-0.
- [73] Boxx, I., Stöhr, M., Carter, C., and Meier, W., “Temporally resolved planar measurements of transient phenomena in a partially pre-mixed swirl flame in a gas turbine model combustor,” *Combustion and Flame*, Vol. 157, No. 8, 2010, pp. 1510–1525. doi:10.1016/j.combustflame.2009.12.015.
- [74] Steinberg, A. M., Boxx, I., Stöhr, M., Carter, C. D., and Meier, W., “Flow-flame interactions causing acoustically coupled heat release fluctuations in a thermo-acoustically unstable gas turbine model combustor,” *Combustion and Flame*, Vol. 157, No. 12, 2010, pp. 2250–2266. doi:10.1016/j.combustflame.2010.07.011.
- [75] Stöhr, M., Boxx, I., Carter, C., and Meier, W., “Dynamics of lean blowout of a swirl-stabilized flame in a gas turbine model combustor,” *Proceedings of the Combustion Institute*, Vol. 33, No. 2, 2011, pp. 2953–2960. doi:10.1016/j.proci.2010.06.103.
- [76] Coriton, B., Steinberg, A. M., and Frank, J. H., “High-speed tomographic PIV and OH PLIF measurements in turbulent reactive flows,” *Experiments in Fluids*, Vol. 55, No. 1743, 2014. doi:10.1007/s00348-014-1743-3.
- [77] Steinberg, A. M., Coriton, B., and Frank, J. H., “Influence of combustion on principal strain-rate transport in turbulent premixed flames,” *Proceedings of the Combustion Institute*, Vol. 35, No. 2, 2015, pp. 1287–1294. doi:10.1016/j.proci.2014.06.089.
- [78] Kirik, J. W., Johnson, R. F., Goynes, C. P., Chelliah, H. K., McDaniel, J. C., and Rockwell, R. D., “Velocimetry Using Graphite Tracer Particles in a Scramjet Flowpath,” AIAA Paper 2015-355, Jan. 2015. doi:10.2514/6.2015-0355.
- [79] Sinibaldi, J. O., Driscoll, J. F., Mueller, C. J., Donbar, J. M., and Carter, C. D., “Propagation speeds and stretch rates measured along wrinkled flames to assess the theory of flame stretch,” *Combustion and Flame*, Vol. 133, No. 3, 2003, pp. 323–334. doi:10.1016/S0010-2180(03)00016-6.
- [80] Hammack, S. D., Lee, T., Hsu, K.-Y., and Carter, C. D., “High-Repetition-Rate OH Planar Laser-Induced Fluorescence of a Cavity Flameholder,” *Journal of Propulsion and Power*, Vol. 29, No. 5, 2013, pp. 1248–1251. doi:10.2514/1.B34756.
- [81] Willert, C. E. and Jarius, M., “Planar flow field measurements in atmospheric and pressurized combustion chambers,” *Experiments in Fluids*, Vol. 33, No. 6, 2002, pp. 931–939. doi:10.1007/s00348-002-0515-7.
- [82] Willert, C., Stockhausen, G., Voges, M., Klinner, J., Schodl, R., Hassa, C., Schurmans, B., and Guthe, F., “Selected Applications of Planar Imaging Velocimetry in Combustion Test Facilities,” *Particle Image Velocimetry*, Vol. 112 of *Topics in Applied Physics*, Springer Berlin Heidelberg, 2008, pp. 283–309. doi:10.1007/978-3-540-73528-1_15.

- [83] Sadanandan, R., Stöhr, M., and Meier, W., “Simultaneous OH-PLIF and PIV measurements in a gas turbine model combustor,” *Applied Physics B: Lasers and Optics*, Vol. 90, No. 3, 2008, pp. 609–618. doi:10.1007/s00340-007-2928-8.
- [84] Rasmussen, C. C., Driscoll, J. F., Hsu, K.-Y., Donbar, J. M., Gruber, M. R., and Carter, C. D., “Stability limits of cavity-stabilized flames in supersonic flow,” *Proceedings of the Combustion Institute*, Vol. 30, No. 2, 2005, pp. 2825–2833. doi:10.1016/j.proci.2004.08.185.
- [85] Donohue, J. M., “Dual-Mode Scramjet Flameholding Operability Measurements,” *Journal of Propulsion and Power*, Vol. 30, No. 3, 2014, pp. 592–603. doi:10.2514/1.B35016.
- [86] Lin, K.-C., Tam, C.-J., Boxx, I., Carter, C., Jackson, K., and Lindsey, M., “Flame Characteristics and Fuel Entrainment Inside a Cavity Flame Holder in a Scramjet Combustor,” AIAA Paper 2007-5381, July 2007. doi:10.2514/6.2007-5381.
- [87] Rockwell, R. D., Goyne, C. P., Rice, B. E., Chelliah, H. K., McDaniel, J. C., Edwards, J. R., Cantu, L. M. L., Gallo, E. C. A., Cutler, A. D., and Danehy, P. M., “Development of a Premixed Combustion Capability for Dual-Mode Scramjet Experiments,” AIAA Paper 2015-0353, Jan. 2015. doi:10.2514/6.2015-0353.
- [88] Ghodke, C. D., Pranatharthikaran, J., Retaureau, G. J., and Menon, S., “Numerical and Experimental Studies of Flame Stability in a Cavity Stabilized Hydrocarbon-Fueled Scramjet,” AIAA Paper 2011-2365, April 2011. doi:10.2514/6.2011-2365.
- [89] Retaureau, G. J., Kovitch, S., Verma, S., and Menon, S., “Experimental Studies of Cavity Flame-Holding in a Mach 2.5 Cross Flow,” AIAA Paper 2009-810, Jan. 2009. doi:10.2514/6.2009-810.
- [90] Driscoll, J. F. and Rasmussen, C. C., “Correlation and Analysis of Blowout Limits of Flames in High-Speed Airflows,” *Journal of Propulsion and Power*, Vol. 21, No. 6, 2005, pp. 1035–1044. doi:10.2514/1.13329.
- [91] Rasmussen, C. C., Driscoll, J. F., Carter, C. D., and Hsu, K.-Y., “Characteristics of Cavity-Stabilized Flames in a Supersonic Flow,” *Journal of Propulsion and Power*, Vol. 21, No. 4, 2005, pp. 765–768. doi:10.2514/1.15095.
- [92] Cantu, L. M. L., Gallo, E. C. A., Cutler, A. D., Bathel, B. F., Danehy, P. M., Rockwell, R. D., Goyne, C. P., and McDaniel, J. C., “Visualization of Simulated Fuel-Air Mixing in a Dual-Mode Scramjet,” *Journal of Propulsion and Power*, Vol. 32, No. 2, 2016, pp. 373–382. doi:10.2514/1.B35760.
- [93] Raffel, M., Willert, C. E., Wereley, S. T., and Kompenhans, J., *Particle Image Velocimetry*, 2nd ed., Springer-Verlag Berlin Heidelberg, New York, 2007.
- [94] Adrian, R. J. and Westerweel, J., *Particle Image Velocimetry*, Cambridge University Press, New York, 2011.
- [95] Adrian, R. J., “Twenty years of particle image velocimetry,” *Experiments in Fluids*, Vol. 39, No. 2, 2005, pp. 159–169. doi:10.1007/s00348-005-0991-7.
- [96] Billig, F. S., “Research on Supersonic Combustion,” *Journal of Propulsion and Power*, Vol. 9, No. 4, 1993, pp. 499–514. doi:10.2514/3.23652.
- [97] Neely, A. J., Riley, C., Boyce, R. R., Mudford, N. R., Houwing, A. F. P., and Gruber, M. R., “Hydrocarbon and hydrogen-fuelled scramjet cavity flameholder performance at high flight Mach numbers,” AIAA Paper 2003-6989, Dec. 2003. doi:10.2514/6.2003-6989.

- [98] Jackson, K. R., Gruber, M. R., and Buccellato, S., "HIFiRE Flight 2- A Program Overview," AIAA Paper 2013-695, Jan. 2013. doi:10.2514/6.2013-695.
- [99] Tam, C.-J., Hsu, K.-Y., Hagenmaier, M. A., and Raffoul, C., "Simulations of Inlet Distortion Effects in a Direct-Connect Scramjet Isolator," AIAA Paper 2011-5540, July 2011. doi:10.2514/6.2011-5540.
- [100] Lahr, M. D., Pitz, R. W., Douglas, Z. W., and Carter, C. D., "Hydroxyl-Tagging-Velocimetry Measurements of a Supersonic Flow over a Cavity," *Journal of Propulsion and Power*, Vol. 26, No. 4, 2010, pp. 790–797. doi:10.2514/1.47264.
- [101] Samimy, M., Petrie, H. L., and Addy, A. L., "A Study of Compressible Turbulent Reattaching Free Shear Layers," *AIAA Journal*, Vol. 24, No. 2, 1986, pp. 261–267. doi:10.2514/3.9254.
- [102] Etheridge, S., Lee, J. G., Carter, C. D., and Hagenmaier, M., "Characterization of Supersonic Flow Interaction with a Shockwave Using Laser-based Diagnostics," AIAA Paper 2012-3776, July 2012. doi:10.2514/6.2012-3776.
- [103] Milligan, R. T., Boles, J. A., Hagenmaier, M. A., Donbar, J. M., Carter, C. D., and Hsu, K.-Y., "Flow Distortion: A Computational Investigation of a Shocked Cavity Flameholder," AIAA Paper 2013-2838, June 2013. doi:10.2514/6.2013-2838.
- [104] Loth, E., "Numerical approaches for motion of dispersed particles, droplets and bubbles," *Progress in Energy and Combustion Science*, Vol. 26, No. 3, 2000, pp. 161–223. doi:10.1016/S0360-1285(99)00013-1.
- [105] Samimy, M. and Lele, S. K., "Motion of particles with inertia in a compressible free shear layer," *Physics of Fluids A: Fluid Dynamics*, Vol. 3, No. 8, 1991, pp. 1915–1923. doi:10.1063/1.857921.
- [106] Westerweel, J., Dabiri, D., and Gharib, M., "The effect of a discrete window offset on the accuracy of cross-correlation analysis of digital PIV recordings," *Experiments in Fluids*, Vol. 23, No. 1, 1997, pp. 20–28. doi:10.1007/s003480050082.
- [107] Benedict, L. H. and Gould, R. D., "Towards better uncertainty estimates for turbulence statistics," *Experiments in Fluids*, Vol. 22, No. 2, 1996, pp. 129–136. doi:10.1007/s003480050030.
- [108] Peterson, D. M., Hagenmaier, M., Carter, C. D., and Tuttle, S. G., "Hybrid Reynolds-Averaged and Large-Eddy Simulations of a Supersonic Cavity Flameholder," AIAA Paper 2013-2483, June 2013. doi:10.2514/6.2013-2483.
- [109] Zhuang, N., Alvi, F. S., Alkisar, M., and Shih, C., "Supersonic Cavity Flows and Their Control," *AIAA Journal*, Vol. 44, No. 9, 2006, pp. 2118–2128. doi:10.2514/1.14879.
- [110] Beresh, S. J., Wagner, J. L., Pruett, B. O. M., Henfling, J. F., and Spillers, R. W., "Supersonic Flow over a Finite-Width Rectangular Cavity," *AIAA Journal*, Vol. 53, No. 2, 2015, pp. 296–310. doi:10.2514/1.J053097.
- [111] Hsu, K.-Y., Carter, C. D., Gruber, M. R., Barhorst, T., and Smith, S., "Experimental Study of Cavity-Strut Combustion in Supersonic Flow," *Journal of Propulsion and Power*, Vol. 26, No. 6, 2010, pp. 1237–1246. doi:10.2514/1.45767.
- [112] Estruch, D., Lawson, N. J., and Garry, K. P., "Application of Optical Measurement Techniques to Supersonic and Hypersonic Aerospace Flows," *Journal of Aerospace Engineering*, Vol. 22, No. 4, 2009, pp. 383–395. doi:10.1061/(ASCE)0893-1321(2009)22:4(383).

- [113] Cutler, A. D., Magnotti, G., Cantu, L., Gallo, E., Rockwell, R., and Goyne, C., “Dual-Pump Coherent Anti-Stokes Raman Spectroscopy Measurements in a Dual-Mode Scramjet,” *Journal of Propulsion and Power*, Vol. 30, No. 3, 2014, pp. 539–549. doi:10.2514/1.B34964.
- [114] Schultz, I. A., Goldenstein, C. S., Jeffries, J. B., Hanson, R. K., Rockwell, R. D., and Goyne, C. P., “Spatially Resolved Water Measurements in a Scramjet Combustor Using Diode Laser Absorption,” *Journal of Propulsion and Power*, Vol. 30, No. 6, 2014, pp. 1551–1558. doi:10.2514/1.B35219.
- [115] Schultz, I. A., Goldenstein, C. S., Spearrin, R. M., Jeffries, J. B., Hanson, R. K., Rockwell, R. D., and Goyne, C. P., “Multispecies Midinfrared Absorption Measurements in a Hydrocarbon-Fueled Scramjet Combustor,” *Journal of Propulsion and Power*, Vol. 30, No. 6, 2014, pp. 1595–1604. doi:10.2514/1.B35261.
- [116] Busa, K. M., Ellison, E. N., McGovern, B. J., McDaniel, J. C., Diskin, G. S., DePiro, M. J., Capriotti, D. P., and Gaffney, R. L., “Measurements on NASA Langley Durable Combustor Rig by TDLAT: Preliminary Results,” AIAA Paper 2013-0696, Jan. 2013. doi:10.2514/6.2013-696.
- [117] Xu, J., Ma, J., Gu, R., Mo, J., and Zhang, K., “PIV Experimental and Numerical Investigation of Cold Flowfield of Scramjet Combustor with Inlet/Isolator,” AIAA Paper 2011-2312, April 2011. doi:10.2514/6.2011-2312.
- [118] Melling, A., “Tracer particles and seeding for particle image velocimetry,” *Measurement Science and Technology*, Vol. 8, No. 12, 1997, pp. 1406–1416.
- [119] Santoro, R. J., Pal, S., Woodward, R. D., and Schaaf, L., “Rocket Testing at University Facilities,” AIAA Paper 2001-748, Jan. 2001. doi:10.2514/6.2001-748.
- [120] Love, B. T., *Particle Size Control for PIV Seeding Using Dry Ice*, Master’s thesis, Air Force Institute of Technology, 2010.
- [121] Neubert, V., Leick, P., Stirn, R., and Dreizler, A., “Analysis of In-Cylinder Air Motion in a Fully Optically Accessible 2V-Diesel Engine by Means of Conventional and Time Resolved PIV,” *9th International Symposium on Particle Image Velocimetry*, July 2011.
- [122] Buschbeck, M., Bittner, N., Halfmann, T., and Arndt, S., “Dependence of combustion dynamics in a gasoline engine upon the in-cylinder flow field, determined by high-speed PIV,” *Experiments in Fluids*, Vol. 53, No. 6, 2012, pp. 1701–1712. doi:10.1007/s00348-012-1384-3.
- [123] Welker, R. W., “Basics and Sampling of Particles for Size Analysis and Identification,” *Developments in Surface Contamination and Cleaning*, edited by R. Kohli and K. L. Mittal, Vol. 4, William Andrew, Waltham, MA, 2012, pp. 1–80.
- [124] Melehy, M. A., “A new thermodynamic theory of adhesion of particles on surfaces,” *8th International Symposium on Particles on Surfaces: Detection, Adhesion, and Removal*, June 2002.
- [125] Corn, M. and Stein, F., “Mechanisms of Dust Redispersion,” *1st International Symposium on Surface Contamination*, June 1964.
- [126] Owens, Z. C., Goyne, C. P., Krauss, R. H., and McDaniel, J. C., “Assessment of Particle Seeder Performance via Direct Flowfield Sampling,” AIAA Paper 2003-0918, Jan. 2003. doi:10.2514/6.2003-918.

- [127] Howison, J. C. and Goyne, C. P., "Assessment of Seeder Performance for Particle Velocimetry in a Scramjet Combustor," *Journal of Propulsion and Power*, Vol. 26, No. 3, 2010, pp. 514–523. doi:10.2514/1.44469.
- [128] Loth, E., "Drag of non-spherical solid particles of regular and irregular shape," *Powder Technology*, Vol. 182, No. 3, 2008, pp. 342–353. doi:10.1016/j.powtec.2007.06.001.
- [129] Lazar, E., DeBlauw, B., Glumac, N., Dutton, C., and Elliott, G., "A Practical Approach to PIV Uncertainty Analysis," AIAA Paper 2010-4355, June 2010. doi:10.2514/6.2010-4355.
- [130] Keh, H. J. and Ou, C. L., "Thermophoresis of Aerosol Spheroids," *Aerosol Science and Technology*, Vol. 38, No. 7, 2004, pp. 675–684. doi:10.1080/02786820490486006.
- [131] Mathur, T., Gruber, M. R., Jackson, K. R., Donbar, J. M., Donaldson, W., Jackson, T., and Billig, F., "Supersonic Combustion Experiments with a Cavity-Based Fuel Injector," *Journal of Propulsion and Power*, Vol. 17, No. 6, 2001, pp. 1305–1312. doi:10.2514/2.5879.
- [132] Ma, F., Li, J., Yang, V., Lin, K.-C., and Jackson, T. A., "Thermoacoustic Flow Instability in a Scramjet Combustor," AIAA Paper 2005-3824, July 2005. doi:10.2514/6.2005-3824.
- [133] Cantu, L. M. L., Gallo, E. C. A., Cutler, A. D., Danehy, P. M., Johansen, C. T., Rockwell, R. D., Goyne, C. P., and McDaniel, J. C., "OH PLIF Visualization of a Premixed Ethylene-fueled Dual-Mode Scramjet Combustor," AIAA Paper 2016-1763, Jan. 2016. doi:10.2514/6.2016-1763.
- [134] Cutler, A. D., Gallo, E. C. A., Cantu, L. M. L., Rockwell, R. D., and Goyne, C. P., "WIDE-CARS Measurements of the Turbulent, Premixed, Ethylene-Air Flame in a Dual-Mode Scramjet," AIAA Paper 2016-3111, June 2016. doi:10.2514/6.2016-3111.
- [135] Gallo, E. C. A., Cantu, L. M. L., Cutler, A. D., Rockwell, R. D., Goyne, C. P., and McDaniel, J. C., "WIDECARS Measurements of a Premixed Ethylene-Air Flame in a Small-Scale Dual-Mode Scramjet Combustor," AIAA Paper 2016-656, Jan. 2016. doi:10.2514/6.2016-0656.
- [136] Baurle, R. A. and Eklund, D. R., "Analysis of Dual-Mode Hydrocarbon Scramjet Operation at Mach 4-6.5," *Journal of Propulsion and Power*, Vol. 18, No. 5, 2002, pp. 990–1002. doi:10.2514/2.6047.
- [137] Grady, N., Pitz, R. W., Carter, C. D., Hsu, K.-Y., Godke, C., and Menon, S., "Supersonic Flow over a Ramped-Wall Cavity Flame Holder with an Upstream Strut," *Journal of Propulsion and Power*, Vol. 28, No. 5, 2012, pp. 982–990. doi:10.2514/1.B34394.
- [138] Westerweel, J. and Scarano, F., "Universal outlier detection for PIV data," *Experiments in Fluids*, Vol. 39, No. 6, 2005, pp. 1096–1100. doi:10.1007/s00348-005-0016-6.
- [139] Moffat, R. J., "Describing the Uncertainties in Experimental Results," *Experimental Thermal and Fluid Science*, Vol. 1, No. 1, 1988, pp. 3–17. doi:10.1016/0894-1777(88)90043-X.
- [140] Donbar, J. M., Gruber, M. R., Jackson, T. A., Carter, C. D., and Mathur, T., "OH planar laser-induced fluorescence imaging in a hydrocarbon-fueled scramjet combustor," *Proceedings of the Combustion Institute*, Vol. 28, No. 1, 2000, pp. 679–687. doi:10.1016/S0082-0784(00)80269-6.
- [141] Adrian, R. J., Christensen, K. T., and Liu, Z.-C., "Analysis and interpretation of instantaneous turbulent velocity fields," *Experiments in Fluids*, Vol. 29, No. 3, 2000, pp. 275–290. doi:10.1007/s003489900087.

- [142] Clemens, N. T. and Mungal, M. G., "Large-scale structure and entrainment in the supersonic mixing layer," *Journal of Fluid Mechanics*, Vol. 284, 1995, pp. 171–216. doi:10.1017/S0022112095000310.
- [143] Kundu, P. K. and Cohen, I. M., *Fluid Mechanics*, 4th ed., Academic Press, Burlington, MA, 2008.
- [144] Glassman, I., Yetter, R. A., and Glumac, N. G., *Combustion*, 5th ed., Academic Press, Waltham, MA, 2015.
- [145] Micka, D. J., Torrez, S. M., and Driscoll, J. F., "Heat Release Distribution in a Dual-Mode Scramjet Combustor - Measurements and Modeling," AIAA Paper 2009-7362, Oct. 2009. doi:10.2514/6.2009-7362.
- [146] Rasmussen, C. C., Dhanuka, S. K., and Driscoll, J. F., "Visualization of flameholding mechanisms in a supersonic combustor using PLIF," *Proceedings of the Combustion Institute*, Vol. 31, No. 2, 2007, pp. 2505–2512. doi:10.1016/j.proci.2006.08.007.
- [147] Freeborn, A. B., King, P. I., and Gruber, M. R., "Swept-Leading-Edge Pylon Effects on a Scramjet Pylon-Cavity Flameholder Flowfield," *Journal of Propulsion and Power*, Vol. 25, No. 3, 2009, pp. 571–582. doi:10.2514/1.39546.
- [148] Pitz, R. W., Lahr, M. D., Douglas, Z. W., Wehrmeyer, J. A., Hu, S., Carter, C. D., Hsu, K.-Y., Lum, C., and Koochesfahani, M. M., "Hydroxyl tagging velocimetry in a supersonic flow over a cavity," *Applied Optics*, Vol. 44, No. 31, 2005, pp. 6692–6700. doi:10.1364/AO.44.006692.
- [149] Beresh, S. J., Wagner, J. L., Henfling, J. F., Spillers, R. W., and Pruett, B. O. M., "Width Effects in Transonic Flow over a Rectangular Cavity," *AIAA Journal*, Vol. 53, No. 12, 2015, pp. 3831–3834. doi:10.2514/1.J054362.
- [150] Demauro, E. P., Beresh, S. J., Wagner, J. L., Henfling, J. F., and Spillers, R. W., "Volumetric Measurement of Transonic Cavity Flow Using Stereoscopic Particle Image Velcimetry," AIAA Paper 2016-2076, Jan. 2016. doi:10.2514/6.2016-2076.
- [151] Beresh, S. J., Wagner, J. L., and Smith, B. L., "Self-calibration performance in stereoscopic PIV acquired in a transonic wind tunnel," *Experiments in Fluids*, Vol. 57, No. 48, 2016. doi:10.1007/s00348-016-2131-y.
- [152] Lusk, T., Cattafesta, L., and Ukeiley, L., "Leading edge slot blowing on an open cavity in supersonic flow," *Experiments in Fluids*, Vol. 53, No. 1, 2012, pp. 187–199. doi:10.1007/s00348-012-1282-8.
- [153] Laufer, G., *Introduction to Optics and Lasers in Engineering*, Cambridge University Press, New York, 1996. doi:https://doi.org/10.1017/CBO9781139174190.
- [154] Wieneke, B., "Stereo-PIV using self-calibration on particle images," *Experiments in Fluids*, Vol. 39, No. 2, 2005, pp. 267–280. doi:10.1007/s00348-005-0962-z.
- [155] Scarano, F., David, L., Bsibsi, M., and Calluaud, D., "S-PIV comparative assessment: image dewarping+misalignment correction and pinhole+geometric back projection," *Experiments in Fluids*, Vol. 39, No. 2, 2005, pp. 257–266. doi:10.1007/s00348-005-1000-x.
- [156] Sciacchitano, A., Wieneke, B., and Scarano, F., "PIV uncertainty quantification by image matching," *Measurement Science and Technology*, Vol. 24, No. 045302, 2013. doi:10.1088/0957-0233/24/4/045302.

- [157] Zhang, T., Wang, J., Qi, L., Fan, X., and Zhang, P., “Blowout Limits of Cavity-Stabilized Flame of Supercritical Kerosene in Supersonic Combustors,” *Journal of Propulsion and Power*, Vol. 30, No. 5, 2014, pp. 1161–1166. doi:10.2514/1.B35120.
- [158] Brown, M. S. and Barhorst, T. F., “Post-Flight Analysis of the Diode-Laser-Based Mass Capture Experiment Onboard HIFiRE Flight 1,” AIAA Paper 2011-2359, April 2011. doi:10.2514/6.2011-2359.
- [159] Williams, S., Barone, D., Barhorst, T., Jackson, K., Lin, K.-C., Masterson, P., Zhao, Q., and Sappey, A. D., “Diode Laser Diagnostics of High Speed Flows,” AIAA Paper 2006-7999, Nov. 2006. doi:10.2514/6.2006-7999.
- [160] Brown, M. S., Barone, D. L., Barhorst, T. F., Eklund, D., Gruber, M., Mathur, T., and Milligan, R., “TDLAS-Based Measurements of Temperature, Pressure, and Velocity in the Isolator of an Axisymmetric Scramjet,” AIAA Paper 2010-6989, July 2010. doi:10.2514/6.2010-6989.